The Dissertation Committee for Oded Doron Certifies that this is the approved version of the following dissertation:

Simulation of an INS Soil Analysis System

Committee:

Steven R. Biegalski, Supervisor

Sheldon Landsberger

D.K. Ezekoye

Lynn Katz

Simulation of an INS Soil Analysis System

by

Oded Doron, B.S., M.S

Dissertation

Presented to the Faculty of the Graduate School of

The University of Texas at Austin

in Partial Fulfillment

of the Requirements

for the Degree of

Doctor of Philosophy

The University of Texas at Austin

December 2007

Dedication

For Cori, my wonderful wife, who stood with me all these years in school

And to my parents for their insistent drive for education

Acknowledgements

I would like to thank my advisor, Dr. Steven Biegalski, and Dr. Sheldon Landsberger for all their guidance and support in my studies and my life. Without their help I am certain I would not be where I am now. I would like to thank Dr. Lucian Wielopolski for giving me the chance to work on the INS project. Thanks are due to all other members of my committee: Dr. Ofodike Ezekoye and Dr. Lynn Katz. I would also like to thank Dr. Sudeep Mitra, and Dr. Rex Omonode for their help and guidance with my work.

I would like to thank my whole family for their motivation and support, and my beautiful wife Cori, our daughter Noa and son Ezra, if it wasn't for them, all of this would be for not.

This manuscript has been co-authored by employees of Brookhaven Science Associates, LLC under Contract No. DE-AC02-98CH10886 with the U.S. Department of Energy. The publisher by accepting the manuscript for publication acknowledges that the United States Government retains a non-exclusive, paid-up, irrevocable, world-wide license to publish or reproduce the published form of this manuscript, or allow others to do so, for United States Government purposes.

Simulation of an INS Soil Analysis System

Publication No._____

Oded Doron, Ph.D.

The University of Texas at Austin, 2007

Supervisor: Steven R. Biegalski

Global climate change in either the form of global warming or global cooling is occurring relatively rapidly today. Studies have shown that increased levels of greenhouse gases, especially atmospheric carbon dioxide (CO_2) are the dominate component contributing to the change. A reduction in CO_2 may be influenced by making larger efforts to sequester carbon in soil and therefore to not only keep soil organic carbon (SOC) levels steady but by possibly increasing them through human assistance. Soil sequestration of carbon has been estimated to have one of the largest potentials to sequester carbon in the world. By some estimation up to 2 billion tons of carbon can be sequestered terrestrially. Therefore the efficient and repetitive monitoring of SOC on a local and global scale is a critical issue. The current soil measurement technique utilized around the world is chemical analysis of one form or another. Chemical analysis of soil is a well studied technique that returns relatively accurate results of density, moisture content, and elemental breakdown of a soil. However, chemical analysis is costly, time consuming, and destructive. As a result of the destructive nature of soil chemical analysis, repeated measurements of the same soil site is impossible. Also, due to time

constraints, it would be difficult to analyze a large area utilizing chemical analysis. To surmount the inherent issues with chemical analysis a system based on inelastic neutron scattering (INS) is under development for non-destructive monitoring of carbon in soil. It is based on spectroscopy of gamma rays induced by fast (14 MeV) neutrons emanating isotropically from a D-T neutron generator (NG). The calibration of the INS system is a remains a challenge. Calibration of the system is necessary for relating the carbon gamma ray counts from the detectors to a carbon concentration in the soil volume measured. Utilizing a benchmarked Monte Carlo model of the INS system it is possible to create many calibration curves. The advantages of the model are that the calculations require a relatively short amount of time, and that all the soil variables are defined by the user.

Table of Contents

List of Tables

List of Figures

Chapter 1: Introduction

Soil carbon sequestration is a rapidly developing field that will assist in the slowing and possible reduction in the rise in atmospheric carbon dioxide levels around the globe. New technologies are emerging that allow for rapid soil carbon measurements, one such device currently being developed at Brookhaven National Laboratory (BNL) is an *in-situ* inelastic neutron scattering (INS) soil analysis system. The calibration of the INS system is the single largest challenge facing the new technology. The research presented here addresses the issues involved with the calibration of the INS system and proposes a calibration method for field measurements utilizing a Monte Carlo model. The goals of the research undertaken are:

1. Develop a model of the system utilizing a Monte Carlo code.
2. Benchmark the model with field experiments and data.
3. Investigate system and soil perturbations.
4. Determine the effective sampling volume and depth of the system.
5. Develop a method for system calibration.

1.1. BACKGROUND

Global change resulting from anthropogenic emissions has become a wide-ranging field of study. Regardless of whether human activities result in global warming or global cooling, studies show that levels of greenhouse gases, especially the increased concentration of atmospheric carbon dioxide (CO_2), are on the rise. The increasing trend of CO_2 has been well documented since 1957 by Dr. Keeling at the Maunu Loa Observatory in Hawaii and has been plotted in what is commonly referred to as the "Keeling Curve" (Fig. 1.1). The yearly fluctuations in Figure 1.1 are seasonal

fluctuations of CO_2 [Keeling, 2005]. Since the majority of the land in the world is in the northern hemisphere. Spring plant blooms and farming cause the CO_2 levels to drop. In the fall when leafs fall and plants wilt the CO_2 levels rise again. This can be described as the "breathing" of the world. It has been theorized that with the increased CO_2 other climate changes are to be expected including a rise in annual mean temperature, changes in rainfall patterns, and a continuing in the increase of CO_2 [Parton, 1993]. Soil organic carbon (SOC) may be influenced by climate change in two ways: altering plant growth that results in limiting the annual return of plant residues to the soil, and by changing the organic input decay rate in or on soil [Jenkinson, 1991]. Emanuel *et al.* (1985) predicted a 17% increase in the world's desert area with the climate changes expected due to a doubling of CO_2. The concentration of greenhouse gases is also further increased by tropical deforestation [Qi, 2004]. The result of desertification and deforestation is the reduction of CO_2 sinks in the world. Qi *et al.* (2004) demonstrated a connection between raising temperatures, decreased precipitation, and increased human activities and the decrease in SOC and as a result in the increase of CO_2.

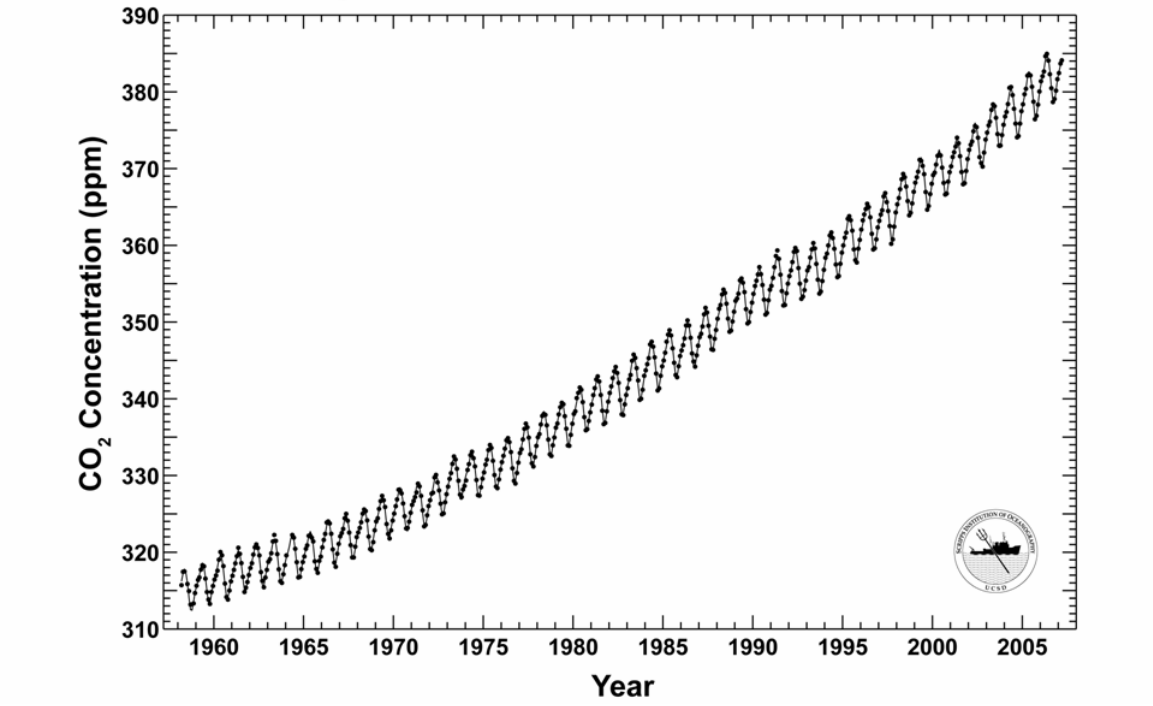

Figure 1.1. Atmospheric CO2 readings from Mauna Loa observatory in Hawaii [Keeling, 2005].

A reduction in CO_2 may be influenced by making larger efforts to not only keep SOC levels steady but by possibly increasing them through human assisted carbon sequestration in soil. The Kyoto Protocol calls for carbon sequestration technologies to be researched and developed.

> "Research on, and promotion, development and increased use of, new and renewable forms of energy, of **carbon dioxide sequestration technologies** and of advanced and innovative environmentally sound technologies" [Article 2.4 of the Kyoto Protocol]

Soil sequestration of carbon has been estimated to have one of the largest potentials to sequester carbon in the world [Garcia-Olivia, 2004]. By some estimation up to 2 billion tons of carbon can be sequestered terrestrially (Fig. 1.2). Carbon sequestration is a natural process. However, certain agricultural practices can aid in maintaining the sequestered carbon in the soil. One such practice that is employed today is Conservation Tillage agriculture as opposed to Conventional Tillage agriculture. Table 1.1 gives an example of a field where half the field was Conservation Till and half Conventional Till. The Field is located at the Pee Dee Research and Education Center of Clemson University in Florence, South Carolina. It is clear from Table 1.1 that the carbon content is not only maintained in the Conversation Tillage plot but actually increases as opposed to the Conventional Tillage plot where the carbon content is reduced. One of the main challenges is how to credit soil carbon sequestration from activities. The main challenges in the measurement of soil carbon include, a need to monitor small changes in SOC relative to large carbon pools, long-time periods to acquire the full carbon benefits, high local variability of SOC, and relatively costly soil carbon measurement procedures [Garcia-Olivia, 2004]. The depth to which soil carbon should be measured is also a challenge. In general, the highest SOC is in the upper most layer of soil and decreases exponentially with depth. Measurements of at least 30 cm in depth should be conducted, because the changes in soil carbon at these depths will be rapid enough to allow for detection during a short period [Masera, 2003]. This research provides a solution to this measurement of C in soil problem.

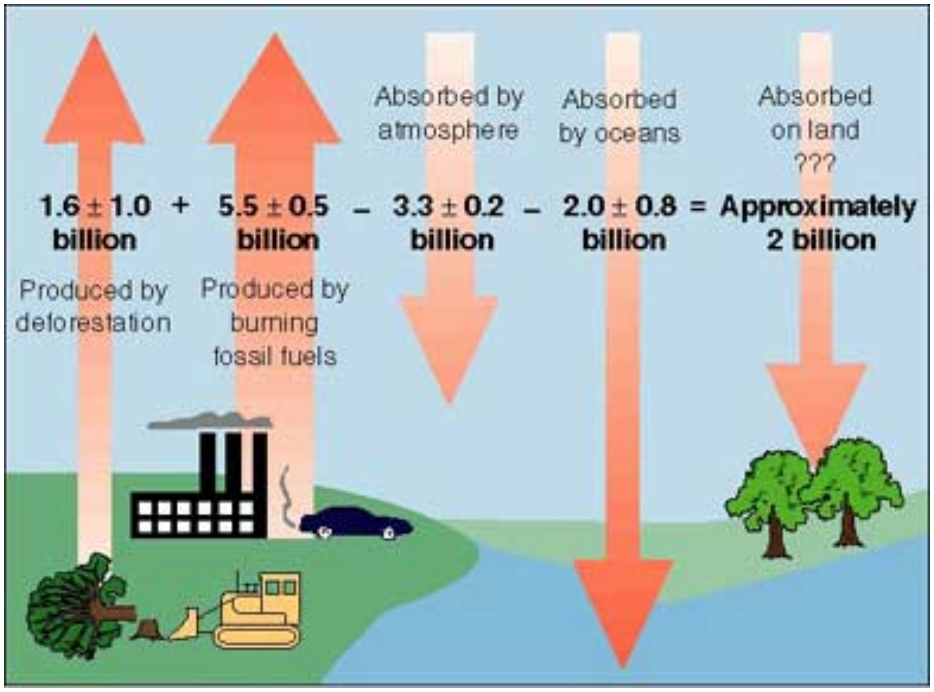

Figure 1.2. CO_2 released yearly and carbon sequestration potential [www.usgs.gov].

Table 1.1 Soil Organic Carbon contents in 1998 and 2005, change in SOC content, summation of OC added as plant residue, and percentage of plant residue entering the SOC pool (SD in parentheses).[Novak, 2007]

		SOC contents (Mg ha^{-1})		
Side	**Depth (cm)**	**1998**	**2005**	**Change**
Conservation	**0 to 3** **3 to 15**	**2.4 (1.1)** **12 (5.1)**	**3.3 (0.9)** **9.1 (4.1)**	**+0.9** **-2.9**
Conventional	**0 to 3** **3 to 15**	**3.1 (1.7)** **13.3 (7.8)**	**2.7 (1.6)** **12.4 (7)**	**-0.4** **-0.9**

Currently the dominate soil measurement technique utilized around the world is chemical analysis by dry combustion. Namely, the instrument used for dry combustion soil carbon analysis is: Leco CHN 2000 Analyzer (Leco Corp. St. Joseph, MI). Chemical analysis of soil is a well studied technique that returns relatively accurate results of density, moisture content, and elemental breakdown of a soil [Cambardella, 1993; Ellert, 1995; Nelson, 1996; Nelson, 1982]. The chemical analysis involves taking soil cores at the field, removing all organic and inorganic debris from the cores, drying the cores, homogenizing the cores, and then analyzing the cores by dry combustion. As a result, chemical analysis is costly, time consuming, and destructive. Due to the destructive nature of soil chemical analysis, repeated measurements of the same soil site is impossible [Pansu, 2001]. Also, due to time constraints, it would be difficult to analyze a large area utilizing chemical analysis. An alternative to chemical analysis is neutron activation analysis (NAA) of the soil.

Neutron activation analysis is a widely utilized measurement technique [Alfassi, 1990]. NAA is capable of detecting 30 to 40 elements. Elemental concentrations are measured based on the measurement of the resulting radioactivity of elements post-irradiation. Every activated or excited isotope emits a characteristic gamma-ray upon deexcitation. As a result of the "signature" energies, individual isotopes may be identified and their concentrations found. NAA has many advantages of which the most important ones for soil are that, NAA is non-destructive, many elements may be analyzed simultaneously and NAA detects trace elements. The most useful neutron reactions for NAA, are INS (Fig. 1.3a) and radiative capture (Fig 1.3b). Radiative capture can be divided into two categories: prompt gamma neutron activation analysis (PGNAA) and delayed reactions, which generally is what is referred to as NAA. INS involves the excitation of an element without the absorption of a neutron rather than activation due to

the absorption of a neutron. The difference is that with activation an atom is transformed to a different isotope. The excitation of an atom involves elevating the nucleus to a higher energy state, but the isotope does not change. The excited nucleus decays and releases a "signature" gamma-ray as a result.

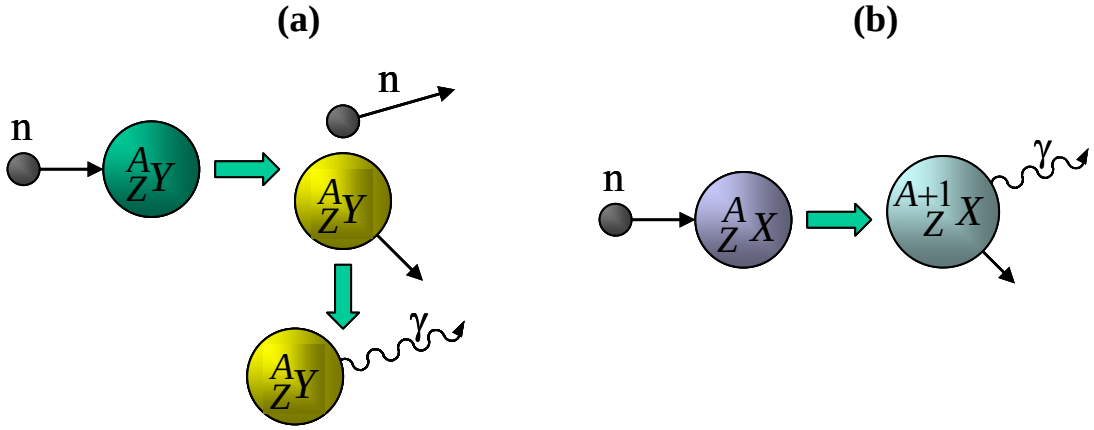

Figure 1.3. Diagrams showing the INS (a) and radiative capture (b) reactions utilized for NAA.

Naqvi *et al.* (2002) experimented via NAA with detecting water content or more specifically hydrogen in soil samples. Their experimental setup involved producing 3 MeV neutrons with a D(d,n)He reaction. The neutrons were directed through a sample and detected by an NE213 scintillation detector. The team ran Monte Carlo simulations to produce calibration curves. The team found that they were able to detect differences in the moisture content of the soil samples.

Nir-El *et al.* (2001) calibrated and found an algorithm for a minimum detectable activity of a germanium p-type detector for environmental analysis. The team performed experiments in-situ at two locations. The team was able to calibrate the detectors in the laboratory using a multinuclide and three single nuclide gamma-ray standard point

sources. The team found it to be a simple procedure to modify the standard software algorithm to be correct for in-situ gamma spectroscopy.

Khatamov *et al.* (2000) experimented with finding the reproducibility of NAA conducted on soil. The team found that the reproducibility of the NAA helps define the degree of uniformity of the distribution of an element in the sample being analyzed.

Macdonald *et al.* (1996) developed an in-situ gamma spectrometry system in North Wales. The team utilized a high-purity n-type germanium detector. The quantitative in-situ spectrometry was compared with the analysis of three core samples. It was found that the concentrations of ^{137}Cs agreed within 25%, and to within 50% for ^{134}Cs. There was complete agreement for ^{40}K within experimental errors. Also, the dose-rates of ^{137}Cs were compared with those from a compensated Geiger-Mueller tube and they found that the numbers were in total agreement with the experimental errors.

Ertek *et al.* (1984) measured the density and water content of soil using photon multiple scattering. The team irradiated the soil samples with a 0.7 mCi ^{137}Cs source. The counting was completed by a stabilized single channel scintillation detector and counter system in the differential mode. The team found that they could accurately determine the density and water content of their soil samples as compared to lab analysis. The team concluded that their method of analysis could be utilized to scan large fields for moisture content and density.

A more advanced form of NAA is Fast prompt gamma neutron activation analysis (FPGNAA) coupled with inelastic neutron scattering (INS) analysis. The decay times involved with FPGNAA are orders of magnitude shorter than with common NAA. FPGNAA occurs on the order of microseconds where as NAA is on the order of seconds or minutes. The temporal advantage of these techniques has made them useful for *in-situ* measurements in the field. FPGNAA and INS analysis have been widely utilized in both

landmine detection and well-bore logging. Calculations performed with the Monte Carlo N-Particle transport code (MCNP) are frequently used for proof of concept and to assist in calibration of the well-bore logging and landmine detection systems [Odom, 1997; Borsaru, 2001].

Hussein *et al.* (2005) examined three radiation scattering techniques for detecting buried landmines. They demonstrated by Monte Carlo simulations with the Monte Carlo N-Particle transport code (MCNP) and experiments the suitability of utilizing thermalization of fast neutrons for measuring concentrations of hydrogen. The elastic scattering of fast neutrons by three prominent elements found in landmines, namely, nitrogen, oxygen, and carbon. Lastly, the Compton scattering of gamma-rays due their dependence on material density makes this an effective technique indicator of landmines.

Maucec *et al.* (2004) developed an MCNP model of a FPGNAA system with a 14 MeV D-T neutron generator, bismuth-germanate (BGO) detection system and a landmine embedded in a rock formation. The potential system would be utilized for the detection of landmines. The team was able to successfully simulate the inelastic and fast gamma spectra from a landmine, including isotopes of C, N, O, Si, Fe, and Al.

1.2. OTHER EMERGING MODALITIES

There are three other emerging modalities for carbon analysis aside from the INS system, laser induced breakdown spectroscopy (LIBS), mid- and near- infrared spectroscopy (MIR and NIR), and pyrolysis molecular beam mass spectroscopy (Py-MBMS) [Gehl, 2006]. A summary of the emerging modalities is presented in Table 1.2, highlighting the differences in the technologies.

Table 1.2. Summary and comparison of the emerging modalities for measuring soil carbon [Wielopolski, 2006].

Instrument	Process	Methodology	Radiation Type Detected	Penetration Depth (cm)	Sampled Volume (cm^3)	Measurement Type
LIBS	**Atomic**	**Plasma Induced Emission**	**Visible**	**~ 0.1**	**10^{-2}**	**Point, Depth Profile, Destructive**
NIR	**Molecular**	**Diffuse Reflectance**	**Near-Infrared**	**~ 0.2**	**10^{0}**	**Surface, Scanning, Destructive**
MIR	**Molecular**	**Diffuse Reflectance**	**Infrared**	**~ 1**	**10^{1}**	**Surface, Destructive**
Py-MBMS	**Molecular**	**Pyrolysis Molecular Beam**	**m/z**	**---**	**10^{1}**	**Samples Destructive**
INS	**Nuclear**	**Neutron Induced Nuclear Reactions**	**Gamma Rays**	**~ 30**	**10^{5}**	**Volume, Scanning, Non-Destructive**

LIBS utilizes a laser that ionizes a solid soil sample and forms a microplasma. A light is emitted from the microplasma that is characteristic of the elements in the sample. The system can quantify carbon and many other elements present in soil in seconds. It is estimated that 100 laser shots target the sample in order to complete one measurement. The LIBS system measures areas of 1 to 5 mm^3 per pulse and the measurement is completed in approximately 10 s. The LIBS instrument is field deployable and requires very little preparation of soil samples aside from coring [Cremers, 2001; Ebinger, 2003].

NIR operates at a wavelength of approximately 1500 nm. NIR measures the diffusely scattered light from an illuminated soil sample. The light penetrates the sample and induces molecular vibrations. These vibrations then partial absorb the light, making it possible to mathematically compare the incident and reflected spectra and differentiate

what quantities of certain molecules were present in the soil sample. The samples NIR measures are 0.5 to 3 cm^3 they do not require any sample preparation and no soil coring is necessary [Christy, 2003].

MIR characterizes a soil sample in a similar way to NIR. However, MIR operates at a wavelength of approximately 6000nm and the current MIR system does require the same soil preparation as for conventional analysis methods, such as combustion. Current MIR system claims to be able to analyze 360 samples per day with an autosampler as compared with 100 samples for combustion methods. The MIR system can determine soil C fractions including organic, inorganic, and total C [Reeves, 2001].

Py-MBMS utilizes pyrolysis along with molecular beam mass spectrometry and multivariate statistical analysis to measure SOC in soils that have been well characterized. Samples are 100-500 mg, and analysis times are typically 3-5 minutes. It has been shown that carbon in the particulate organic matter, mineral, and microbial biomass fractions may be quantified [Wielopolski, 2006].

1.3. RESEARCH PATH

The development of any model for a real world system requires a profound knowledge of both the real world system and the code utilized for the modeling. The steps taken to model and develop a calibration method for the INS system are as follows:

- Review and study the physics and geometry of the system (chapter 2).
- Study the MCNP code to utilize the correct modeling tools provided by the code (chapter 3 and 5).
- Model the detectors of the system (chapter 4).
- Model the system in MCNP (chapter 3,4 and 5)

- Utilize the model to estimate the sampling volume and depth of the system (chapter 6).
- Benchmark the model of the system (chapter 7).
- Utilize the model to calculate soil perturbations effects (chapter 8).
- Produce calibration curves (chapter 9).

Chapter 2: The INS System

In situ elemental analysis of bulk soil is required both for emerging precision agriculture and for monitoring and verifying the soil's carbon stocks resulting from carbon sequestration programs. In one promising approach, this is done by NAA, in which carbon in soil is analyzed utilizing a 14 MeV neutron generator (NG) operated in a pulsed mode [Wielopoloski, 2000], whereby fast neutrons impinging on soil undergo INS with C nuclei. The C cross-section for INS (Fig. F.1) makes it an ideal candidate for utilizing fast neutrons (>5 MeV) for analysis. In addition neutrons thermalized via elastic scattering with the soil's matrix elements undergo capture reactions (TNC). Both the INS and TNC processes induce characteristic gamma-ray emissions from the soil elements that are separated in time by the duration of the thermalization processes. Thus, while the first occurs during the neutron pulse the second occurs mainly between the neutron pulses. Such time-dependent gamma-ray spectra using pulsed NGs have been effectively used for elemental characterization of explosives, contraband and in the oil well logging, coal and cement industries [Vourvopoulos, 2001; Gozani, 2003; Schweitzer. 1991; Dep, 1998].

The alpha prototype of the system became operational in 2003 that was able to perform static scanning. Both field and lab experiments measuring various levels of carbon in soil demonstrated a strong correlation with standard chemical analysis. A beta prototype became operational in 2005 that was able to operate in both static and dynamic modes. A new soil analysis facility was constructed at BNL for the operation and testing of the beta prototype. The beta prototype has been utilized extensively on many field trips. Strong correlations of large field scans with chemical analysis have been shown.

Currently, construction has begun on a new 16 detector system that should allow for scanning yet larger areas.

2.1. NEUTRON SOURCE

The fast 14 MeV neutrons used in these studies were produced by a compact sealed-tube neutron generator (NG) in which an accelerated deuteron beam impinges on a zirconium target impregnated with tritium, producing a neutron and an alpha particle via a D-T fusion reaction. The NG is operated in a pulsed mode at a repetition rate of 10 kHz and a 25% duty cycle emitting nominally 10^8 neutrons s^{-1} into a 4π solid angle. The neutron output can be adjusted by changing the high voltage and/or the beam current of the accelerator. The NG's ion-source voltage controller also generates a logic level HIGH when the neutron beam is "ON" which is used for gating the DMCA. Between the pulses, the GATE signal level is LOW corresponding to the neutron beam "OFF" state.

The fast neutron output is routinely monitored with a plastic scintillator (Bicron, BC-400) and calibrated with copper-foil activation that utilizes the reaction ^{63}Cu (n,2n) ^{62}Cu. This reaction has a threshold at neutron energy of 11.3 MeV [Mitra, 2004].

2.2. DATA ACQUISITION SYSTEM

Gamma-rays were detected using three large, 12.7x12.7x15.2 cm^3, NaI(Tl) detectors connected to a summing current-to-voltage (I-to-V) converter interfaced directly to a Polaris Digital Multi Channel Analyzer (DMCA) system (Polaris spectrometer from XIA LLC). Before each run, the three detectors were gain-matched using standard ^{137}Cs and ^{60}Co calibration radiation sources. Figure 2.1 shows the block diagram of the data-acquisition system.

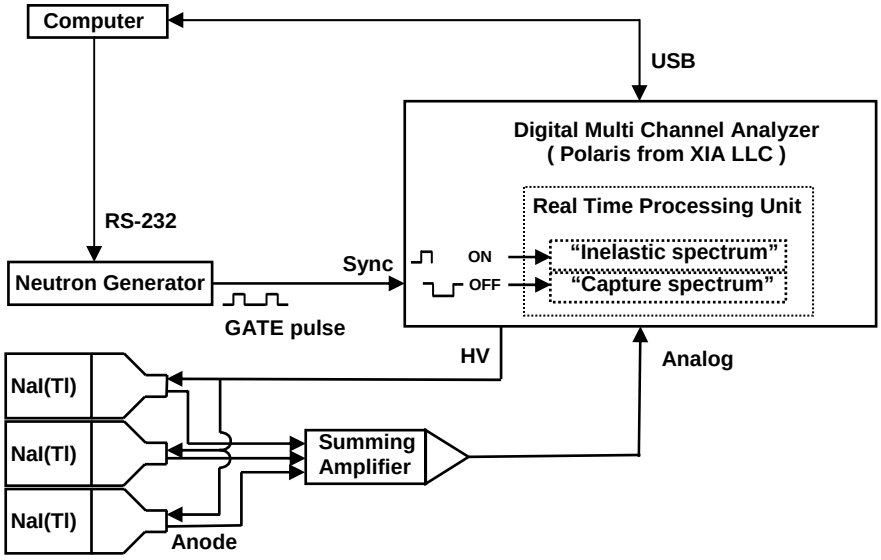

Figure 2.1. Schematic of the experimental apparatus. [Mitra, 2007]

The off-the-shelf Polaris DMCA system was re-programmed to store the incoming gamma-ray pulses in two memory groups depending on the GATE level at the DMCA's SYNC input. The "ON" group held the INS events collected during the neutron pulse while the "OFF" group held the TNC events occurring in between the neutron pulses. The pertinent dead time corrections, pile-up rejections, incoming count rate (ICR), and the observed count rate (OCR) for both channels were monitored independently of each other. The system terminated the data acquisition when the OFF channel reached a prescribed real-time (RT) or live-time (LT). Naturally; RT and LT were different in the ON and OFF channels, depending on the count rate and the duty cycle. Two typical INS and TNC gamma-ray spectra acquired concurrently with the current system from a grass land are shown in Figure 2.2.

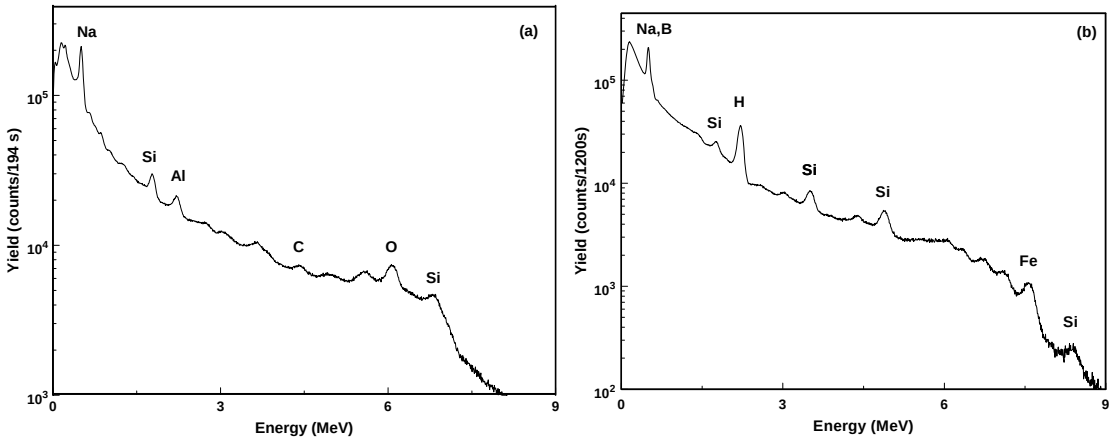

Figure 2.2. Gamma-ray spectra acquired concurrently; (a) an INS spectrum during the neutron pulse and (b) a TNC spectrum between neutron pulses from a grass land.[Mitra, 2007]

2.3. THE CARBON SIGNAL

The carbon signal yield (from neutron source to pulse height distribution) from a given soil that the INS system is used to analyze can be expressed as in Equation 2.1. Equation 2.1 is based on the Boltzmann neutron transport equation. Equation 2.1 can not be solved analytically and because of the multiplicity of integrals any numeric solution will be very cumbersome and highly inefficient. Instead the value of the integration is estimated using a probabilistic Monte Carlo method by which the entire system is simulated following the paths of particles from their creation to death thus enabling accurate modeling of complex systems and economically replacing complicated experiments. One of the possible codes to perform these numerical experiments is the Monte Carlo N-Particle transport code Version 5 (MCNP5) developed at Los Alamos National Laboratory [Girard, 2003]. The MCNP5 code was utilized in this project and is discussed below.

$$R \propto \int_0^T dt \int_{-\infty}^{\infty}\int_{-\infty}^{\infty}\int_{h}^{\infty}\int_{E_{thr}}^{E_{\max}} \phi_n(x,y,z,E)\,\sigma_{ins}(E)\,C_f(x,y,z)\,\rho_b(x,y,z)\,\Omega(x,y,z)\,A(x,y,z)\,dEdxdydz \quad (2.1)$$

Where $\phi_n(x,y,z,E)$ is the neutron flux distribution in the soil given in units of (n cm^{-2} s^{-1}), $\sigma_{ins}(E)$ is the neutron cross section, or the probability of an INS interaction given in units of (cm^{-1}), $C_f(x,y,z)$ is the carbon weight fraction in units of (gC g^{-1} soil), $\rho_b(x,y,z)$ is the soil bulk density in units of (g soil cm^{-3}), $\Omega(x,y,z)$ is the solid angle subtend by the detectors, $A(x,y,z)$ is the gamma ray attenuation in the soil.

2.4. SYSTEM SHIELDING AND GEOMETRY

The three NaI(Tl) detectors require heavy shielding from the 14 MeV neutrons produced by the NG. The shielding of 14 MeV neutrons is a relatively trivial issue in the field of nuclear engineering; however, most neutron shielding materials utilized today contain carbon. The INS system is measuring carbon from the soil therefore any added carbon in the shielding would interfere in the carbon signal. A detailed review of shielding materials, experiments, and final shielding setup is given in Chapter 4. Based on a height optimization experiment, discussed below, the INS system is mounted about 30 cm above the ground (Fig. 2.3). The system appears on a stationary stand in Figure 2.3, in reality it is mounted on a cart of the same height. Figure 2.4 is a picture of the system in a U.S. Department of Agriculture field in Beltsville, Maryland. Shown in Figure 2.4 are the cart, the electronics, and the two side borated water tanks that have the same dimensions as the borated water tank in between the NG and the detectors.

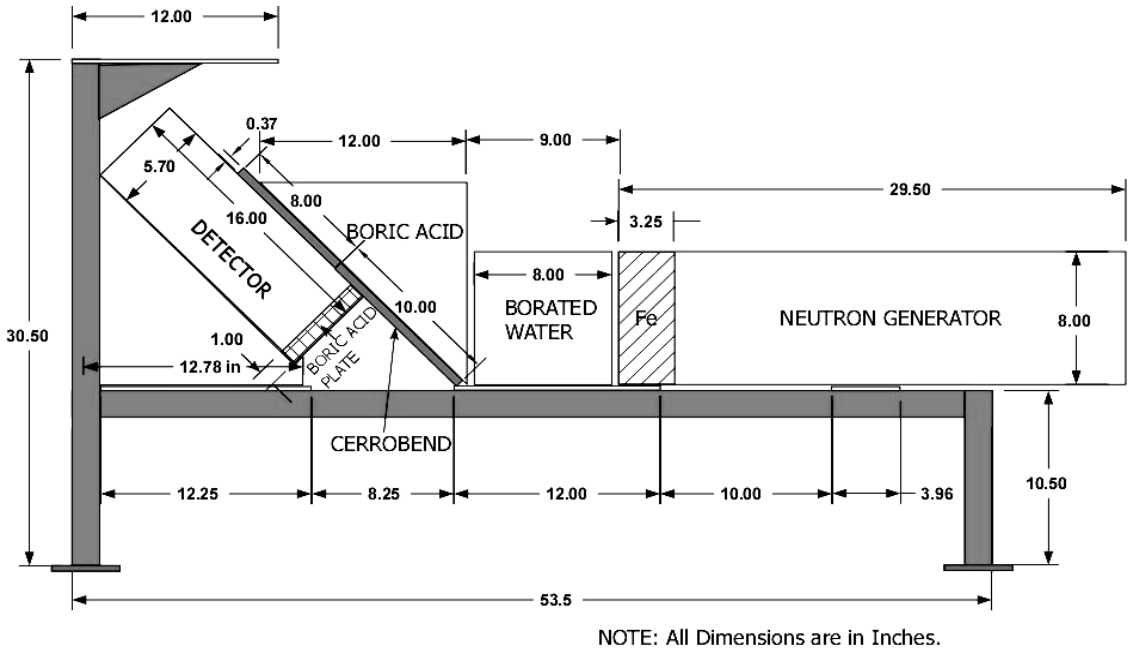

Figure 2.3. Schematic diagram of the INS system Shielding configuration.

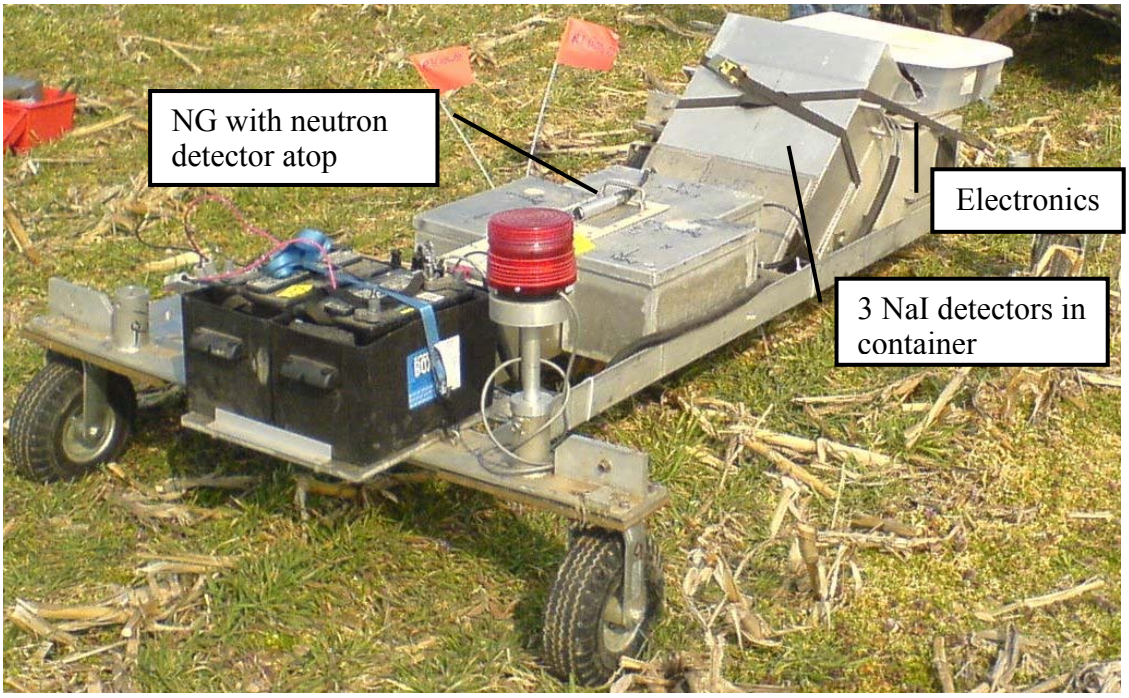

Figure 2.4. Picture of the current INS system in the field.

A height optimization experiment was performed in the field to maximize the net peak areas of the three main regions of interest (ROI), silicon, oxygen, and carbon. Due to the shadow shielding configuration between the NG and the detectors there is an optimal system height where soil activation and the view point of the detectors on the soil provide maximum net peak areas in the ROI's. The energy windows of the three ROI's are given in Table 2.1. The system was raised from the ground level up to a source height of 57 cm with a spectra acquired for 30 minutes at each position. The results from the experiment are presented in Figure 2.5.

Table 2.1. The energy windows for the ROI's of silicon, carbon, and oxygen.

Element	Energy Windows (MeV)	
Silicon	1.673	1.889
Carbon	4.356	4.698
Oxygen	5.935	6.351

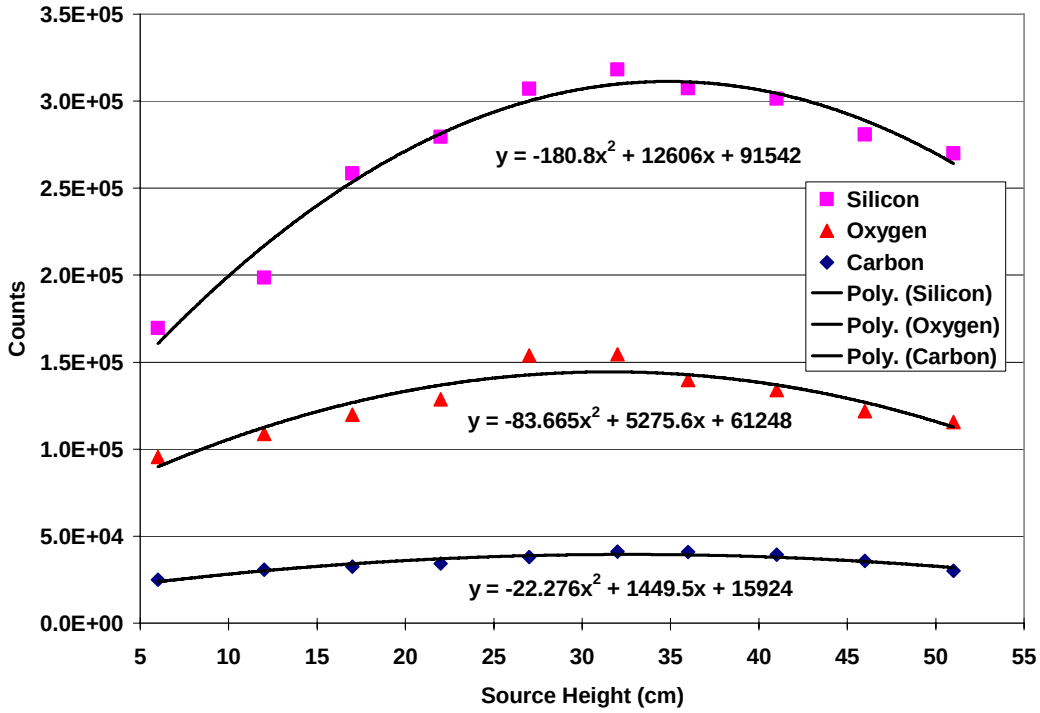

Figure 2.5. The height optimization results from the field experiment.

2.5. MODEL DEVELOPMENT

The model of the INS system was developed in stages. Components of the system were added individually in order to enhance the understanding of the effect of each component on measurements, calculations, and computer processing times. The final result is two main versions, alpha and beta, of the model that may be utilized for different calculations. Versions α and β of the model are given as Figures 2.6 and 2.7, respectively. The system can be broken down into four major components for modeling: the shielding, the detectors, the cart, and the soil volume. The soil volume in both versions was chosen to be 250 cm by 200 cm by 60 cm deep to encompass the experimental soil volumes utilized in lab experiments. The soil in both versions, unless otherwise stated, is composed of the top thirteen elements in median world soils (App. A). The soil bulk density of 1.4 g cm^{-3} was chosen to represent the average bulk density of world soils [Frank, 1993]. Version α includes the soil volume, most of the shielding with the exception of the two borated water tanks (Fig. 2.4) on either side of the neutron generator. The detectors are modeled as a single large volume of NaI(Tl) without individual housings and insulation of each detector. The cart is not included in version α. Version α is useful for calculations where relative changes as opposed to exact numbers are sufficient, and that do not require pulse height distributions. Version α is utilized for all reaction rate calculations (chapters 5 and 6) and some soil perturbation calculations (chapter 8). Version β includes all the geometry in version α and also the shielding housing, the side borated water shielding, most of the cart and the three detectors are modeled individually and materials around the detectors including their housing and insulation are included as well. The major items excluded in the modeling of the cart are: axles, wheels, power generator, the NG housing, and the electrics box. Version β is

utilized for pulse height distributions. The decision to exclude items from the geometry of version β was based on calculations that compared the increased computer processing time of additional geometry with increased model accuracy. One such calculation is demonstrated in Figure 2.8. Two calibration sources, ^{137}Cs and ^{60}Co, were utilized to acquire spectra in MCNP with three different models and with the INS system. The three models are version α with three separate detectors, version α with the detectors in a stainless steel housing, and version β. The spectrum from each MCNP model is compared with the spectrum from the INS system. The spectrum from version β shows the good correlation with the INS spectrum. The experiment is described in more detail in Chapter 7. An example of the input for MCNP for version β is given in Appendix B.

A more detailed discussion of version β of the model is given here. The MCNP5 model utilizes the default source, an isotropic mono-energetic 14 MeV point source located at the origin.

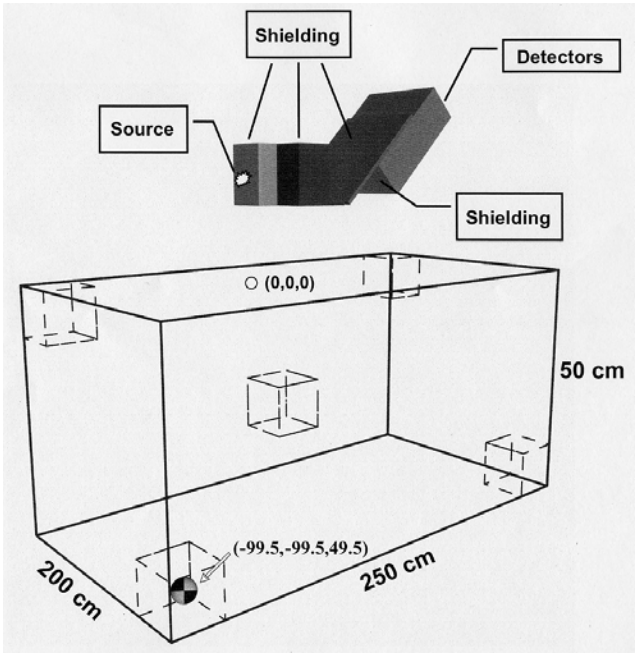

Figure 2.6. Version α of system geometry as modeled and the tally locations used for comparison of the tally options discussed in chapter 5.

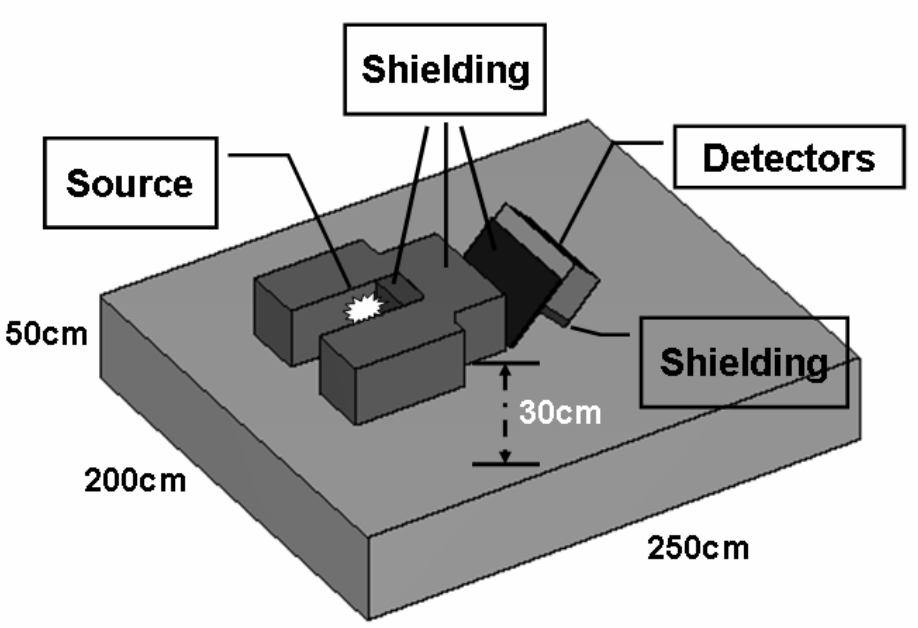

Figure 2.7. Version β of system geometry as modeled. The model of the cart is excluded to improve visual clarity.

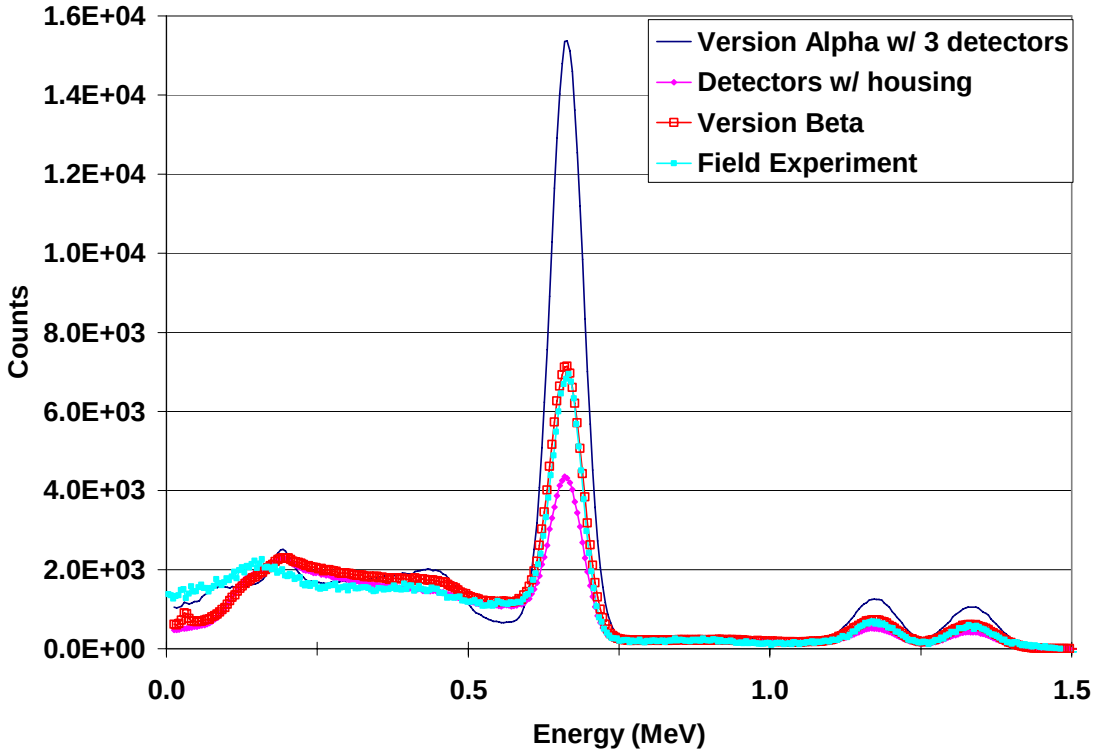

Figure 2.8. The spectra of 137Cs and 60Co from three MCNP models and a field experiment.

2.5.1. Modeled Shielding and Cart

The complete shielding of the system is included in the model. Starting with the shielding in closest proximity to the detectors and moving toward the NG, the shielding components are:

1. Compressed BA discs at the bottom surface of each detector
2. Two cerrobend plates on the detector face closest to the NG
3. Aluminum box with borated water at the front of the NG
4. 3.5” thick aluminum block inside the NG housing
5. 2 Aluminum boxes with borated water, one either side of the NG

The system's cart is manufactured from aluminum and is modeled with the correct dimensions. However, in the interest of reducing the modeling of extraneous materials, the "axles" of the cart are excluded from the model.

2.5.2. Detectors

The importance of modeling the correct geometry of the detectors to achieve an accurate pulse height distribution cannot be over emphasized. The system's three NaI(Tl) radiation detectors are modeled to the highest level of accuracy possible from the engineering information available. The geometry of the three detectors is identical with the exception of their relative positions in the system. The detectors were manufactured by Scionix. The engineering drawings of the detectors from Scionix were utilized to model the detector geometry and materials surrounding the detectors accurately (App. C). A further email communication with Scionix was necessary to clarify all the materials surrounding the NaI crystal (App. D). Each detector is composed of a 127 mm by 127 mm by 152 mm high Tl doped NaI crystal. Adjacent to the sides of the crystal is a 4 mm sheet of TEFLON, followed by a 2 mm sheet of pack aluminum oxide, and on the bottom of the crystal there is a are 2.5 mm sheet of silicon rubber followed by a 0.2 mm thick Nylon reflector (negligible, not modeled) and finally there is a 2 mm Stainless Steel casing around all sides of the crystal. The photomultiplier tube is modeled as scatterer as a steel cylinder.

The F8 pulse height tally discussed in Chapter 3 was utilized to calculate pulse height distributions in the detector volumes. A detailed explanation on the use of the F8 tally for the model and the calculation for the broadening of the pulse height distribution tally is given in Chapter 7.

Chapter 3: MCNP Code

Monte Carlo codes are widely utilized today for assessing gamma- and neutron-transport in soil. The Monte Carlo method is a probabilistic one that follows the path of a particle from its creation to death, simulating all its interactions in between. The result is an ability to accurately model complex real-world systems and economically undertake time- saving calculations. One of the codes often used is the Monte Carlo N-Particle transport code (MCNP) developed at Los Alamos National Laboratory [Girard, 2003]. MCNP codes previously were employed to simulate radiation transport in soil. HOWELL *et al.* utilized MCNP to model the measurement of chlorine with prompt gamma-ray neutron activation analysis [Howell, 2000]. MAUREC also used it to assess the sensitivity of neutron- and gamma-flux in soils saturated with fresh water, salty water, and oil [Maurec, 2005].

3.1. MCNP

The Monte Carlo N-Particle code is a general purpose, continuous-energy, generalized-geometry, time-dependent Monte Carlo transport code. MCNP can be utilized for neutron, photon, and electron transport individually or combined. MCNP is a three-dimensional code that treats an arbitrary three-dimensional configuration of materials in geometric cells bounded by first and second degree surfaces and fourth degree elliptical tori. The MCNP calculations for this work were completed mainly on Version 5 of MCNP (MCNP5) and some calculations were also performed on the extended version, MCNPX, of MCNP [Girard, 2003; Pelowitz, 2005].

All of the MCNP codes utilize the Monte Carlo method to solve the transport equation. The Monte Carlo method is extremely effective for solving complicated three-dimensional, time-dependent problems. Monte Carlo is utilized to simulate statistical

processes, such as nuclear interactions, and is therefore utilized throughout the nuclear industry. In particle transport, the Monte Carlo technique is pre-eminently realistic (a numerical experiment) [Metropolis, 1949; Mosegaard, 1995]. The specifics of how the Monte Carlo technique is utilized in MCNP can be found in the MCNP5 manual [Girard, 2003].

MCNP5 utilizes point-wise, continuous-energy nuclear and atomic data libraries. The nuclear data are from the Evaluated Nuclear Data File (ENDF) system, Advanced Computational Technology Initiative (ACTI), the Evaluated Nuclear Data Library (ENDL), Evaluated Photon Data Library (EPDL), the Activation Library (ACTL) compilations from Livermore, and evaluations from the Nuclear Physics (T-16) Group at Los Alamos. The evaluated data are processed with codes such as NJOY into an ACE format utilized for MCNP. All of the data tables available to MCNP are given in a cross-section directory file called XSDIR.

3.2. TALLIES

Monte Carlo obtains answers by simulating individual particles. Results are recorded and tallied as a function of user-defined specific aspects of their average behavior. MCNP has seven standard tallies that can be modified and utilized in a combination of ways to help understand and solve a problem. Four of the tallies were used for the all of the calculations completed to model the INS system; the surface current (F1), the surface flux (F2), the track length estimate of the flux (F4), and the pulse height tally (F8). A brief discussion of each tally will be given here and an extend discussion of the variations of the F4 tally, including the Mesh and Lattice Tallies will be given in Chapter 4. Also, the F8 tally will be discussed in more detail in Chapter 6.

The F1, surface current tally is a count of the number of particles crossing a surface. The user has the option of tallying the current in both directions, i.e. the particles

crossing a surface in the positive x direction and those crossing in the negative x direction, and the sum of both directions giving a net current for the surface. When a particle enters a cell a track length for every component of the life the particle in that cell is recorded. The F4 tally calculates volumetric flux by summing all of the track lengths (Eq. 3.2).

$$F4 = \frac{1}{V}\int_E \int_t \int_V \phi(\vec{r}, E, t)\, dE\, dt\, dV \tag{3.1}$$

Where the scalar flux $\phi(\vec{r}, E, t)$ is defined as the particle flux as a function of position, energy, and time. The particle flux may also be defined as the multiple of the particle velocity (v) and the particle, or track length density (N). Substituting this and ds=v dt into Equation 3.1, we arrive at Equation 3.2.

$$F4 = \frac{1}{V}\int_E \int_s \int_V N(\vec{r}, E, t)\, dE\, ds\, dV \tag{3.2}$$

The results from an F4 tally are in units of particles cm^{-2} (source particle)$^{-1}$:

$$F4 = \frac{\frac{neutron\,track\,length(cm)}{Volume(cm^3)}}{Source\,Particles} = \frac{\frac{particle}{cm^2}}{Source\,Particle}$$

The results can be multiplied by the number of source particles, whether neutron, photons, or electrons to calculate an absolute flux number.

The F2, surface flux tally is estimated using a surface crossing estimator that may be thought of as the limiting case of the cell flux or track length estimator when the cell becomes infinitely thin. The results for the tally are the same units as the F4 tally. MCNP provides the option to tally along the track length as well to calculate values such

as reaction rate with the tally multiplier (FM) option. The general calculation for the FM tally is given in Equation 3.3.

$$FM \Rightarrow C\int \phi(E) f(E) dE \tag{3.3}$$

Where C is any constant multiplier that the user wishes to enter, *i.e.* if calculating reaction rates C would be the number density of the material in question. ϕ(E) is the energy dependent fluence and *f*(E) is any product or summation of the quantities in the cross-section libraries or a response function provided by the user. The syntax for the FM card is given below:

FMn C m R

Where n is the F4 tally number for which the FM card is to be utilized to calculate reaction rate. C is the constant multiplier; in this work C is always the number density of the material in question in order to calculate reaction rates in reactions cm^{-3} (source particle)$^{-1}$. M is the material number as defined in the material cards of the material for which the reaction rates will be calculated for. Also, m does not have to be part of the geometry; it can be solely utilized for the FM card. R is the reaction number desired. The reaction numbers utilized in this work are given in Table 3.1.

Table 3.1. List of reactions utilized in this work.

MCNP Reaction Number	Reaction Cross Section
51	(n,n',γ) to 1st excited state
102	(n,γ)
103	(n,p)

The F8, pulse height tally provides the energy distribution of pulses created in a cell that models a physical detector. Although the entries on the F8 card are cells, this is not a track length cell tally. F8 tallies are made at source points and at surface crossings. The pulse height tally is analogous to a physical detector. The F8 energy bins correspond to the total energy deposited in a detector in the specified channels by each physical particle. All the other MCNP tallies record the energy of a scoring track in the energy bin.

3.3 VARIANCE REDUCTION

The two forms of variance reduction utilized in the MCNP work presented here are source variance reduction and weight splitting of particles. Source variance reduction involves decreasing the solid angle in to which the 4-π NG source is emitted, thereby concentrating the neutrons in to a smaller volume and conserving computer processing time. The weight splitting of particles increases the number of particles during a run and as a result increases the statistics of the code without increasing the processing time of the run.

3.3.1. Source Variance Reduction

A 4-π neutron point source in MCNP was biased in such a way that only a fraction of the source is sampled code execution. The geometric representation of the biasing `of the source is given as Figure 3.1.

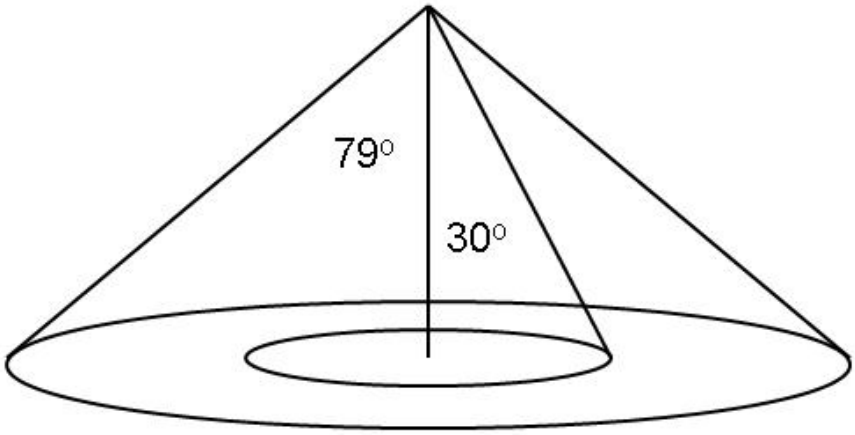

Figure 3.1. Solid angles utilized for the biasing in the source variance reduction in MCNP.

Three sample cases were run in order to ensure that the source is sampled isotropically within the biased solid angle (Ω). The sample cases that were run varied the biasing of the neutron source by varying the sampling angle (θ), measured from the vertical z-axis. Cases 1, 2, and 3 have the source biasing angles of, 4-π, between cos(79°) and cos(0°), and between cos(79°) and cos(30°), respectively. Case 3 will be used for a more specific explanation. The biasing of the source between cos(79°) and cos(30°) forces what would be a 4-π source to be sampled strictly within the biased angles. There should be two major consequences to this restricted source sampling: there should be no neutrons detected anywhere but within the sampled angles, and the neutron density of the biased source should be greater than the unbiased (discussed further below). Four tallies were utilized to ensure that no neutrons were present outside of the biased angles. In each biasing sample case the same neutron tallies were utilized. The angles representing the location of the tallies are also all measured from the z-axis. The locations of the tallies are at 15°, 35° and 76°, and given represented by θ_1, θ_2, and θ_3, respectively (Fig.

3.2). The results of the calculations are given in Table 3.2. From the results, it is clear that the source biasing forces the neutrons to be sampled only within their biased angles.

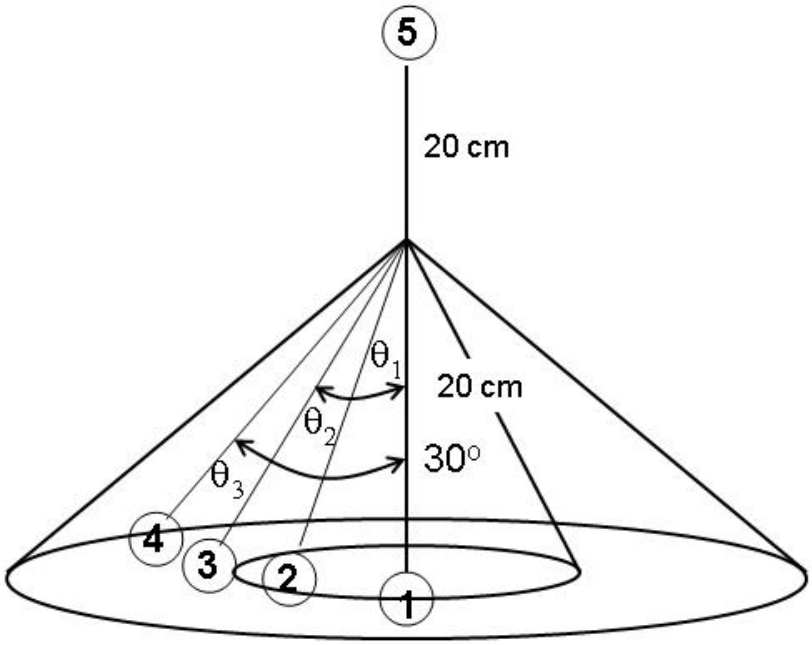

Figure 3.2. Locations of neutron tallies used to analyze the source variance reduction technique.

Table 3.2. The neutron fluxes at the different tally points from the three variance reduction cases. * Errors less than 1%.

	Neutron Flux (n cm^{-2} (source particle)$^{-1}$)		
Tally #	**Case 1 ***	**Case 2 ***	**Case 3 ***
1	1.98E-04	5.00E-04	0.00E+00
2	1.95E-04	4.97E-04	0.00E+00
3	1.95E-04	4.89E-04	5.86E-04
4	2.00E-04	4.90E-04	5.86E-04
5	1.96E-04	0.00E+00	0.00E+00
Mean	1.97E-04	4.94E-04	5.86E-04
σ	1.82E-06	5.03E-06	1.70E-07

Source biasing is an extremely powerful variance reduction technique and it is important that its affect on the final tally answer be understood. Source biasing forces

MCNP to sample only in a given region, therefore increasing statistics [Maucec, 2005]. The final answer is biased by the ratio of the volume of the biased sampled region to the original sampling volume. The neutron density should therefore be greater by this ratio. The derivation of the biasing ratio is given below.

$$d\Omega = \int_0^{2\pi}\int_{\theta_1}^{\theta_2} \sin\theta d\theta d\alpha \tag{3.4}$$

$$= \left[\alpha\Big|_0^{2\pi}\right]\int_{\theta_1}^{\theta_2} \sin\theta d\theta \tag{3.5}$$

$$\Omega = 2\pi\left[-\cos\theta\Big|_{\theta_1}^{\theta_2}\right] \tag{3.6}$$

$$\Omega = 2\pi\left[-\cos(\theta_2) + (\cos(\theta_1))\right] \tag{3.7}$$

Therefore the ratio of the solid angles subtended by the sources to that of the *4–π* source is Ω/4π. The ratio of the solid angles is called the weighting factor (W). The comparison of the calculated ratio to the one obtained from MCNP is given in Table 3.3. The results demonstrate that the biased neutron density is greater by the ratio of Ω/4π.

Table 3.3. The fluxes from case 2 and 3 are equal (within σ) to that of case 1 when they are multiplied by their respective weighting factors. $W_2=\Omega_2/\Omega_1$ & $W_3=\Omega_3/\Omega_1$, where $\Omega 1=4\pi$, $\Omega_2=2.084$ rads, and $\Omega_3=4.243$ rads. * Errors less than 1%.

	Neutron Flux (n cm^{-2} (source particle)$^{-1}$)		
Tally #	**Case 1 ***	**Case 2 *W_2 ***	**Case 3 *W_3 ***
1	1.98E-04	2.02E-04	0.00E+00
2	1.95E-04	2.01E-04	0.00E+00
3	1.95E-04	1.98E-04	1.98E-04
4	2.00E-04	1.98E-04	1.98E-04
5	1.96E-04	0.00E+00	0.00E+00
Mean	1.97E-04	2.00E-04	1.98E-04

The variance reduction technique of source biasing is an effective way to reduce computer processing time while increasing statistics. The calculated weighting factor is multiplied by the final answer to allow for direct comparison to unbiased experimental data.

3.3.2. Particle Weight Splitting

The weight splitting of particles is a less cumbersome method than source biasing to improve statistics while maintaining or decreasing processor times. The basic idea is that as a particle travels into important regions of the geometry it is split into two particles each with half the weight of the original particle. Also, as the two particles travel back into a region of lower importance only one particle is allowed to enter return to its original weight while the other particle is killed. This allows for higher statistics in regions of higher importance and lower statistics in regions of lower importance. This technique was utilized in the reaction rate calculations in the soil volume presented in chapter 6.

3.4. SOLID ANGLE VERIFICATION WITH MCNP

Solid angle test cases were run in MCNP and compared to equations and literature to analyze the solid angle calculation processes in MCNP. The solid angle from a point and cubic source to a parallelepiped detector is also simulated. The errors of all results are less than 1%.

3.4.1. Point Source and Disc Detector

The first set of simulations has an isotropic point source emitting into 4-π at a lateral distance of 50 cm from the center of a disc detector with a radius of 5 cm (Fig. 3.3). An F2 source tally and an F1 surface current tally were taken on the front surface of the disc (facing the source). The results from the point source and disc detector

calculations are given below in Table 3.4. Equation 3.5 is utilized for solid angle estimation and is compared to the F2 tally from MCNP. The F2 tally has units of cm^{-2} and thus must be multiplied by the surface area of the disc to be comparable to Equation 3.8. The product of Equation 3.8 with the cosine of the angle of inclination of the disc is compared to the F1 tally from MCNP.

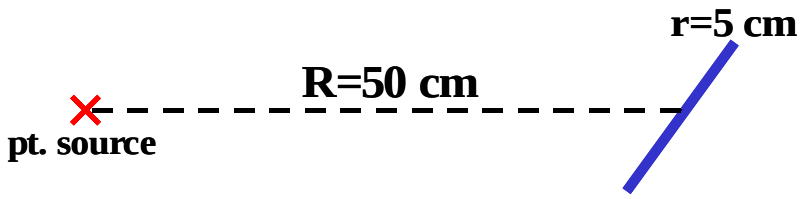

Figure 3.3. First set of simulations run in MCNP. The disc was varied in angle from vertical at 0 degrees to the horizontal at 90 degrees. The 45 degree angle is shown in the diagram.

Table 3.4. Solid angle from the point source and disc detector simulations.

Angle θ (degree)	F2 (particles cm^{-2} (source particle)$^{-1}$)	Area (cm^2)	F2*Area	$r^2 4R^{-2}$	$(r^2 4R^{-2})$*cos θ	F1 (particles)
0	3.17E-05	78.54	2.49E-03	2.50E-03	2.50E-03	2.48E-03
45	3.16E-05	78.54	2.48E-03	2.50E-03	1.77E-03	1.74E-03
60	3.17E-05	78.54	2.49E-03	2.50E-03	1.25E-03	1.23E-03
75	3.14E-05	78.54	2.46E-03	2.50E-03	6.47E-04	6.17E-04
90	0.00E+00	78.54	0.00E+00	2.50E-03	0.00E+00	0.00E+00

$$\Omega = \frac{\pi r^2}{4\pi R^2} = \frac{r^2}{4R^2} \tag{3.8}$$

3.4.2. Point, Disc and Cylindrical Sources and Upright Circular Cylinders and Disc Detectors

The second sets of simulations involve varying combinations of an isotropic point, disc and cylindrical source each positioned at different locations in reference to either an upright cylindrical or disc detector (Fig. 3.4). The results from the point source and disc source and the upright cylindrical detector are given in Table 3.5. The F1 results from MCNP are comparable to those from the literature [Wielopolski, 1977]. The F1 tally from MCNP is multiplied by 4-π because the F1 result is the fraction of the full solid angle (4-π) and the results in the literature were presented in steradians

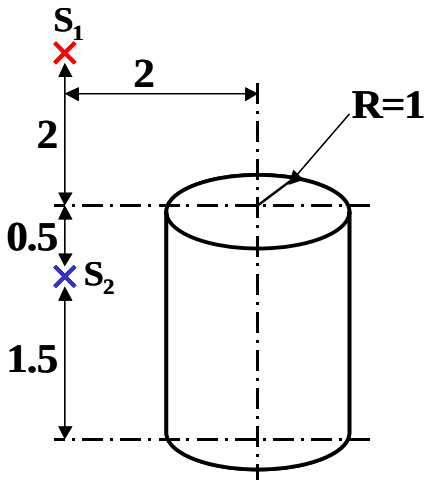

Figure 3.4. Second set of simulations run in MCNP. The solid angle is calculated with the source at position at S_1, above and to the left of the cylinder, and at position S_2, above midpoint and to the left of the cylinder. Dimensions are arbitrary.

Table 3.5. Solid angle from a point source and upright cylindrical detector, a disc source and disc detector, and a cylindrical source and disc detector as compared to the literature.

case[a]	F1 (particles)	F1*4π	solid angle literature
1	0.0303	0.3807	0.3775
2	0.1005	1.2623	1.2602
3	0.0004	0.0050	0.0047
4	0.0041	0.0521	0.0568
5	0.0028	0.0346	0.0333

[a] **Case Geometries**

1) Point source at S_1 above cylindrical detector
2) Point source at S_2 on side cylindrical detector
3) Disc source parallel to a disc detector
4) Disc source perpendicular to a disc detector
5) Cylinderical source parallel to disc detector

3.4.3. Point Source and Parallelepiped Detector

The third set of simulations involved an isotropic point source and a parallelepiped detector (Fig. 3.5). A point is positioned at various locations around the parallelepiped and the fractions of the solid angle is calculated in MCNP utilizing F1 and compared to values found in literature. The results from the point source and the parallelepiped detector are given below in Table 3.6. The F1 results from MCNP were directly comparable to the literature because the literature presented the results as fractions of solid angles as well [Wielopolski, 1984].

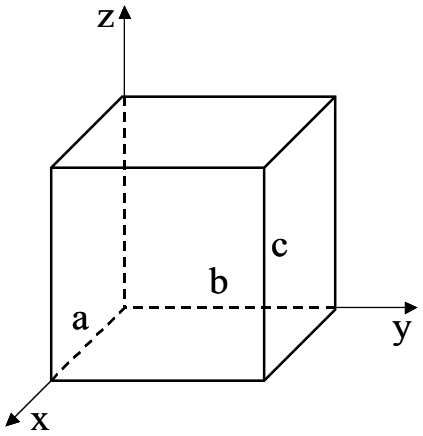

Figure 3.5. Third set of simulations run in MCNP. The solid angle is calculated with the source at position at the locations indicated in Table 3.5.

Table 3.6. Fraction of the solid angle from the point source and parallelepiped detector simulations as compared to the literature.

case[a]	Source location (x,y,z)	F1 (particles)	Solid Angle Literature
1	1,1,10	1.12E-01	1.12E-01
2	19,9,10	1.12E-01	1.12E-01
3	5,15,10	8.26E-02	8.24E-02
4	25,15,10	3.80E-02	3.79E-02

[a] **Case Geometries**

parallelpiped detector a=20, b=10, c=5

1) pt above back left corner of detector
2) pt above front right corner of detector
3) pt above and right of detector
4) pt above, in front, and right of detector

3.4.4. Square Source and Square Detector

The fourth set of simulations was of a square distributed source and a square detector. The results from the square source and the square detector are given below in Table 3.7. The F1 results from MCNP were directly comparable to the literature because the literature presented the results as fractions of solid angles as well [Wielopolski,

1984]. The exception is that the result from MCNP from case 1 had to be divided by four to fit the analytical solution. This exception is discussed in Wielopolski [1984]. Wielopolski suggested that there is ambiguity in the given dimensions of the analytical solution in the reference from which the solution was compared.

Table 3.7. Fraction of the solid angle from the square source and square detector simulations as compared to the literature. The distributed square sources are 1 cm by 1 cm and are parallel and concentric to a square detector.

case[a]	Separation Distance	F1 (particles)	Solid Angle Literature
1	1.5	2.36E-02	2.36E-02
2	10	7.97E-04	7.94E-04

a) case 1 detector is a 2cm by 2cm square
case 2 detector is a 1cm by 1cm square

3.4.5. Cubic and Point Source and Parallelepiped Detector

The above calculations demonstrate the effectiveness of utilizing the F1 surface tally in MCNP to calculate fractions of solid angles from point and distributed sources to various geometries of detectors. Solid angle from point sources and of 1 cm^3 cube sources concentric with the point sources to a parallelepiped detector were calculated utilizing MCNP (Fig. 3.6). The results from the solid angle calculations for the point and cubic sources are given below in Tables 3.8 and 3.9, respectively. The F1 tally to each surface of the detector is calculated and the individual surface contributions are summed. The correct cosine bin had to be utilized to calculate the correct solid angle. The F1 tally calculates net surface current, *i.e.* the addition of the current passing a surface in both directions. For correctly calculating the solid angle only current entering the detector was volume was desired. The solid angle from the point and cubic sources are very close. Therefore the point source to the detector is a correct estimation of the solid angle from

the cube sources to the detector. This estimation greatly simplifies the solid angle calculations of this sort.

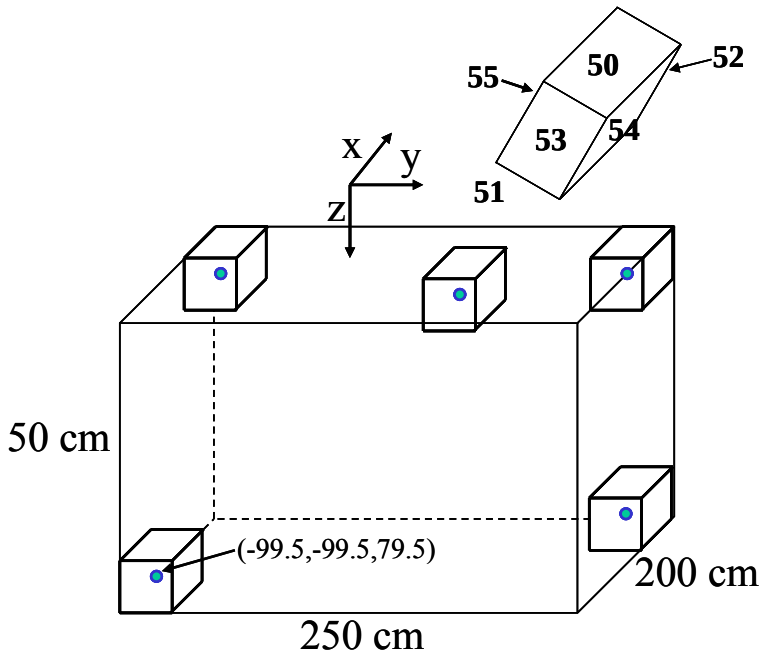

Figure 3.6. The geometric representation of the solid angle comparison from point and cubic sources to a parallelepiped detector is shown. The surface numbers of the detector as defined in MCNP and given in tables 3.8 and 3.9, are indicated. The origin of the system is 30 cm above the large volume shown. The location of the point and corresponding concentric cubes is shown, and the index of one of the sources is given as an example of index labeling.

Table 3.8. The fraction of solid angle calculated with the F1 tally in MCNP from a point located at the indicated locations to the detector. The solid angle is given to each plane of the detector separately and the detector as a whole.

	F1 - Surface Tally						MCNP
Point Position	**54**	**51**	**50**	**55**	**53**	**52**	**Total - Fraction Ω**
70.5, 0, 30.5	2.73E-02	1.57E-02	0	0	0	0	4.30E-02
149.5, 99.5, 30.5	1.65E-03	0	4.39E-04	0	0	6.86E-04	2.78E-03
149.5, 99.5, 79.5	1.58E-03	0	0	0	0	4.41E-04	2.02E-03
-99.5, 99.5, 30.5	0	7.30E-04	0	5.41E-04	0	1.87E-04	1.46E-03
-99.5, -99.5, 79.5	0	8.03E-04	0	2.13E-04	1.59E-04	0	1.18E-03

Table 3.9. The fraction of solid angle calculated with the F1 tally in MCNP from a 1 cm^3 cube source concentric with the indicated location to the detector. The solid angle is given to each plane of the detector separately and the detector as a whole.

	F1 - Surface Tally						MCNP
Cube Position	**54**	**51**	**50**	**55**	**53**	**52**	**Total - Fraction Ω**
70.5, 0, 30.5	2.72E-02	1.58E-02	0	0	0	0	4.30E-02
149.5, 99.5, 30.5	1.66E-03	0	3.94E-04	0	0	7.11E-04	2.77E-03
149.5, 99.5, 79.5	1.52E-03	0	0	0	0	4.18E-04	1.94E-03
-99.5, 99.5, 30.5	0	7.44E-04	0	5.38E-04	0	1.88E-04	1.47E-03
-99.5, -99.5, 79.5	0	7.90E-04	0	2.52E-04	1.40E-04	0	1.18E-03

Chapter 4: Detector Shielding

The INS system utilizes neutron shielding located between the NG and the detectors in an attempt to reduce the neutron flux intercepting the detector volume and therefore lowering the detector activation from neutrons. The detectors were modeled in MCNP5 and field experiments and calculations were performed to optimize the neutron shielding.

4.2. DETECTOR SHIELDING

The use of a radiation source, 14 MeV, (D,T) neutron generator (NG), in a close proximity to the detection system without any precautions will flood and saturate the detectors with direct radiation from the source. A shadow shielding placed between the source and the detection system was partially optimized and experimental results with basic MCNP calculations are discussed.

Radiation shielding issues can be looked upon in two broad categories, first, as being a massive radiological or biological shielding for a facility and, second, a system or an instrument shielding which, by its nature, is very compact. These two types of shielding fundamentally differ in their sizes, materials, and objectives. Facility shielding for reactors, accelerators, and intense neutron generators have been extensively described in the literature [Schaeffer, 1973]. These facilities, by and large, contain thick walls made of concrete or high density concrete arranged in a labyrinth to reduce radiation streaming and most of them take advantage of the $1/r^2$ rule to reduce the dose outside the walls. On the other hand, shielding for a system or an instrument is compact, light, and might be very specialized. Hence, there is no single approach for system shielding design, although many individual shielding arrangements, and very often one of a kind, have been described in the literature [Ellis, 1987; Harling, 1990]. Furthermore, systems can be

subdivided into passive and active where each one necessitates a different type of shielding. For passive systems the main shielding consideration is to reduce the background gamma ray radiation thus increasing the signal-to-noise ratio and reducing the error. However, for active systems a distinction has to be made whether it uses gammas or a neutrons as a primary source of radiation and what kind of radiation is being detected, again gamma rays or neutrons. Thus the source and the detection systems either can be shielded independently or jointly using a shadow shielding configuration in which the shielding is placed between the source and the detectors.

4.2.1. The INS System and Shielding Experiments

The INS system consists of a 14 MeV NG embedded in shadow shielding and placed beside an array of NaI detectors (Fig. 2.3). There is also a neutron detector for NG output normalization. The shadow shielding consists of the following items; 1) an iron block is the closest to the fast neutron source is to reduce the neutron energy via inelastic scattering, 2) borated water which is next further thermalizes and absorbs the neutrons, 3) wedge filled with loose powder of boric acid (BA) to absorb neutrons, 4) cerrobend plates on the side of the detector for gamma ray shielding consisting of an alloy of Bi, Cd, Pb, and Sn, which is a high density alloy with a low melting point, and 5) a compressed (~7,000 kg/cm^2) boric acid plates at the bottom of the detectors to absorb thermal neutrons reaching the detector, it is marked as a dashed areas under the detectors in Figure 2.3. Additional features are labeled in Figure 2.3. The approximate weight of the total shielding is about 200 kg and the exercise became to reduce the shielding weight without compromising too much on increased gamma ray background count rate, or losses in the peak areas due to pulse pile-up in the detector.

Real and numerical experiments were carried out in which different components of the shielding were replaced by other materials or removed altogether. Specifically; Fe

was replaced by Al with somewhat lower cross sections but lighter and by borated polyethylene (BPE). In addition the efficacy of the borated water as a moderator and absorber was checked against regular water and heavy water. Next the relevance of the boric acid wedge and the top two plates, of the four plates, of cerrabend was also evaluated. Some of the tests were performed with the system in its standard configuration at 30 cm above the ground, whereas, to assess the gamma ray albedo from soil, measurements were also taken at 140 cm above the ground. Some of the experiments were backed up by Monte Carlo calculations. The results of these alterations are summarized in the next section.

4.2.2. Results

Experiments and simulations were completed 30 cm above the soil, replacing Fe with Al. The field and MCNP results are summarized in Table 4.1. Version α of the model was utilized as the base model. The input count rates increase 24% when replacing Fe with Al in the field experiments. The Al ROI peak intensity in MCNP increases 20% when replacing Fe with Al. The peak increases 35% when Fe is replaced with Al and the BA wedge and top two plates of cerrabend are removed. The Al ROI increase is not observed in the field data. One possible explanation is that the cart that supports the system is Al along with the shielding boxes and the detector casing itself and these were not modeled in MCNP, therefore the addition of the Al shielding is a relatively small addition. In the field and MCNP results the ROIs for C, O, and Si have no statistical difference when replacing Fe with Al, nor when the BA wedge and top two plates of cerrabend are removed.

Table 4.1. The summary of INS ROI's for field experiments and MCNP simulations replacing Fe shielding with Al shielding, and removing the boric acid wedge and the top two plates of cerrabend.

Shield	Si (1.78 MeV)		Al (2.21 MeV)		C ROI (4.43 MeV)		O (6.13 MeV)	
	Field (counts)	MCNP (γ cm^{-2} (source n)$^{-1}$)	Field (counts)	MCNP (γ cm^{-2} (source n)$^{-1}$)	Field (counts)	MCNP (γ cm^{-2} (source n)$^{-1}$)	Field (counts)	MCNP (γ cm^{-2} (source n)$^{-1}$)
Fe	1236762 ±3892	7.02E-08 2.23E-09	165577 3535	2.50E-08 1.29E-09	59201 2694	4.73E-08 1.79E-09	324945 2548	2.81E-07 4.32E-09
Al	1259673 ±5072	7.07E-08 2.23E-09	163814 4678	3.10E-08 1.43E-09	59916 3269	5.21E-08 1.86E-09	317752 3338	3.09E-07 4.51E-09
Al, no wedge' lower cerrabend	1235984 ±4480	7.22E-08 2.25E-09	159967 4453	3.86E-08 1.58E-09	62672 3076	4.76E-08 1.79E-09	348666 3133	3.04E-07 4.47E-09

Experiments and simulations were completed at 140 cm above the soil to analyze the effect of replacing the borated water with heavy water. Replacing the borated water shielding with heavy water reduced the 2.2 MeV hydrogen counts. The field data shows hydrogen ROI has about 3 times fewer counts when heavy water is used in place of borated water while not affecting the carbon counts (Table 4.2). MCNP data shows H ROIs peak intensity to be 14 times lower and also not affecting the carbon peak intensity (Table 4.3). The discrepancy between the reduction observed in the field and MCNP results could arise from the natural presence of hydrogen in the field, *i.e*. moisture in the soil, whereas there is no hydrogen present in the MCNP problem. However, both field and MCNP show a significant decrease in the H ROI with borated H_2O replaced with D_2O.

Table 4.2. The carbon and hydrogen ROIs from field experiments of replacing borated water with heavy water. Indicated in the table are the shielding inside the neutron generator and the water shielding.

Shielding inside NG	Water shielding	INS			TNC		
		C ROI 4.43			H 2.22		
		Total	Background	Net	Total	Background	Net
3.25" Fe	Borated	814600	802410	12189 ± 1272	341970	278418	63552 ± 787
3.25"Fe	D_2O	785890	774416	11474 ± 1249	299410	279385	20024 ± 760

Table 4.3. The carbon and hydrogen ROIs from MCNP calculations of replacing borated water with heavy water. Indicated in the table are the shielding inside the neutron generator and the water shielding.

Shielding inside NG	Water shielding	INS	TNC
		C ROI 4.43	H 2.22
		γ cm^{-2} (source n)$^{-1}$	γ cm^{-2} (source n)$^{-1}$
3.25" Fe	Borated	1.25E-08	2.58E-08
	±	1.48E-09	2.09E-09
3.25"Fe	D_2O	1.14E-08	1.83E-09
	±	1.42E-09	5.83E-10

The Fe shielding was replaced with BPE into two different system configurations. The results from the two configurations are given in Table 4.4. The first configuration was the same as the heavy water experiment, at 140 cm above the soil. Field data shows that the input count rate increased about 24%, the same as replacing Fe with Al, however, the carbon ROI has about 3.3 times more counts with BPE than with Fe (Fig. 4.2). MCNP results shows carbon ROI peak intensity is 3.7 times that of Fe when BPE is used. The

second configuration was the same as the Al experiment, at 30 cm above the soil. Field data shows carbon ROI has 1.44 times more counts with BPE than with Fe. MCNP shows carbon ROI peak intensity is 1.32 times that of Fe when BPE is used. Both field and MCNP data shows that there is a detectable difference in carbon when Fe is replaced with BPE. As we approach the soil the BPE carbon effect is lower but is still significant.

Table 4.4. Ratios of the areas in the region of the carbon peak using BPE shielding instead of iron at two different heights of the system above the ground.

System Height Above the Soil (cm)	Field	MCNP
140	3.3	3.7
30	1.4	1.3

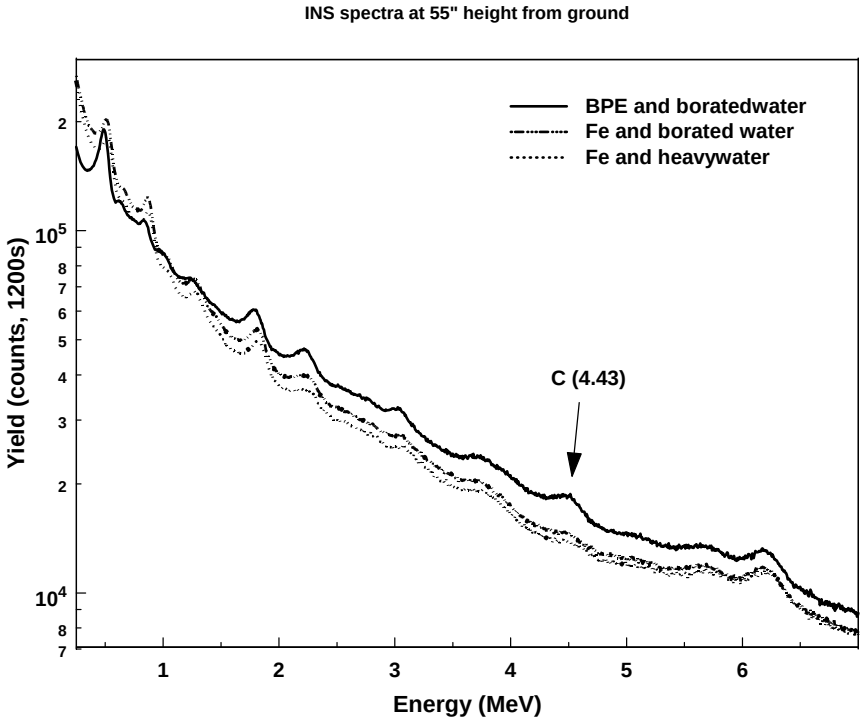

Figure 4.2. The effect of BPE shielding shows the increase in the carbon content [Wielopolski, 2008].

The Fe shielding can be replace with Al, and the BA wedge and the two top plates of cerrabend can be removed with no or little affect on the C, Si, Al, or O ROI's. The result is reducing the weight of the system by approximately 43 kg or 21% of the total weight of the system. Borated water can be replaced with heavy water without affecting the carbon ROI while reducing the hydrogen counts greatly. This will be useful if moisture content measurements are desired. Though BPE does not affect the ROIs discussed, it increases the carbon peak which is counter productive for the system.

Chapter 5: Mesh and Lattice Tallies

5.1. INTRODUCTION

The induced carbon inelastic reaction rates (RR) in the soil will be an important tool to help understand neutron transport and its interactions. Furthermore, the RR will help in predicting the sampling depth, footprint, and volume of soil that the INS system measures. The research discussed herein is the calculations and comparisons we made of the induced inelastic scattering reaction rates for carbon in the soil utilizing different tallying options in MCNP5 [Girard, 2003] and MCNPX [Pelowitz, 2005]. Our ultimate goal is to be able to calculate large RR matrices for a given soil volume. Reaction rates were calculated in 0.125 cm^3 and 1 cm^3 volumes to observe differences. It was found that the general shape of the reaction rate curves from the two different volumes was the same. The 1 cm^3 volumes are used for the purposes of minimizing computer processor times and amount of data to process.

To calculate the RR in every cubic centimeter, or voxel, of the soil volume, 2.5 million tallies are taken in MCNP. MCNP offers two options for calculating large numbers of tallies in a volume; the mesh tally, and the lattice tally. The former is a virtual grid structure superimposed on a geometry, rather than being defined as part of the geometry. Furthermore, the estimate of the track length of the particle flux is calculated, and the flux distributed to the defined mesh cells utilizing an efficient algorithm. Consequently, the mesh tally allows for calculation of large matrices with greatly reduced computational times. By contrast, the lattice flux tally is a part of the geometry, and flux is calculated separately for every tallying cell, which, for a large matrix, can become computationally cumbersome. Recently, a fast lattice tally (FLT) was developed for MCNPX. Although the FLT offers competitive computational times, it is not applicable

for all lattice cases. Carbon-inelastic RRs were calculated with the lattice and mesh tally in MCNP5, and with the FLT in MCNPX. All the codes were executed starting with 100 million source neutrons on the same 3.2 GHz personal computer with sole use of the computer processor. A detailed description of these three tallies, their results and respective computational times are compared, and the advantages of these methodologies discussed.

5.2. Lattice Creation and Tally

A lattice of 1 cm^3 voxels was created in a soil volume of dimensions 250x200x60 cm^3. The lattice (LAT) feature of MCNP is a powerful and time saving one, as will be explained in this summary. The idea behind the lattice is that the user can create many identical cells with actually only creating one and then replicating it. MCNP allows two options for lattice cell geometries, LAT =1 and 2, hexahedra (solid with six faces) and hexagonal prism, respectively. The lattice cell must be assigned to a certain universe (U). This universe is then used to fill (FILL) another universe. The idea will be made clearer with an example of the lattice that was created in the soil volume in question.

The cell cards that define the cells necessary to make up the lattice are given below:

```
c Cell cards
c Cell #1
1     0    -1 2 -3 4 -6 5   FILL=1  imp:n,p 1 $150x100x 60 cm lattice volume
c Cell #2
2  1 -1  -10 11 -12 13 -15 14  imp:n,p 1 LAT=1  U=1 $lattice definition 1 cm^3
volumes
```

Cell 1 is the definition of the soil volume. Cell 2 is the definition of the 1 cm^3 voxel that replicated to create the lattice. The voxel is defined as a hexahedra, LAT=1,

and that it makes up universe 1, U=1. In the cell 1 definition, the FILL=1 dictates that the soil volume is completely filled with U=1, or the 1 cm^3 voxels. The end result is that the complete volume, U=0, is filled with 2.5 million voxels, U=1, creating the lattice and the user only had to enter two cell lines to define it.

The time saving ability of the lattice feature is obvious, and one of the powerful tools that the lattice allows is tallying locations. It is possible with the lattice to tally in only one lattice cell, a row of lattice cells, or in every single tally cell. The tallying format for this example is given below:

(2<2[0 0 0]) Single Tally

(2<2[-150:100 0 0]) Single Row Tally

(2<2[-150:100 –100:100 0:50]) Every Cell Tally

These tallies are all instructing MCNP to tally cell 2 that is within cell 2. This format seems redundant, but that is only because of the simplicity of this example. When, there are several universes, and cells within cells, this tally format is extremely useful. Every lattice cell has its own indices that are what is given in the brackets of the tallies. The logic of the indices definition is best explained in the volume two of the MCNP5 manual, so its discussion will be left out here. The single tally is self-explanatory. The single row tally is asking for the tally from –150 to 100 of the X index only, so it will yield the tally of just one row. The tally for every single cell, asks for the full range of lattice cells defined by the indices. The lattice that was setup for this problem has not yet been extensively utilized but will most likely be in the near future.

5.3. Mesh Tally

An MCNP mesh tally is created for the same soil volume as for the lattice tally. The mesh tally's individual volumes are all the same 1 cm^3 voxels. The tally fills the same volume as the lattice. The mesh tally card entries are described below. The general format of the mesh tally is:

FMESHn:pl fmesh variable = specification

Where: n = tally number (only tally type 4 [volumetric] are permitted)
pl = N or P or E [Girard, 2003]

The discussion of all of the possible entries is not necessary here. The specific entries that are used in this example are given in Table 5.1 below.

Table 5.1. Entries used on mesh card.

Card Entries	Meaning
ORIGIN	Specifies beginning of mesh
IMESH	Location of coarse meshes in X direction
IINTS	Number of fine meshes within corresponding coarse meshes
JMESH	Location of coarse meshes in Y direction
JINTS	Number of fine meshes within corresponding coarse meshes
KMESH	Location of coarse meshes in Y direction
KINTS	Number of fine meshes within corresponding coarse meshes
EMESH	Value of coarse mesh in energy, in MeV
EINTS	Number of fine meshes within corresponding coarse energy meshes

The specific mesh card that is used is:

FMESH4:n ORIGIN=-150 -100 30
IMESH = 100 IINTS = 250
JMESH = 100 JINTS = 200
KMESH = 90 KINTS = 60
EMESH =Variable EINTS = Variable

The origin of the soil volume is at the center of the volume on the x and y-axis, and is 30 cm above the soil for the z-axis (Fig. 2.6). The origin of the mesh is at the back, left, and top corner of the mesh, with it origin at (-150, -100, 30). There is only one coarse mesh location for x,y,z, because all the tally volumes desired were the same. For the x and y-axis, there are 250 and 200 fine mesh points in the coarse meshes, dictating that at every 1 cm there was a fine mesh line. For the z-axis, there are 60 fine mesh points, dictating again, that there were fine mesh lines every 1 cm. The energy mesh is variable because it is changed depending on the energy spectrum desired.

The output matrix of the mesh tally is given as a six column matrix with the columns listed in order as, energy, x, y, z, tally output, and relative error. The x, y, z coordinates are of the center of the specific tally volume. A snip of the mesh output is given as Appendix E.

5.4. Reaction Rate Matrix

The INS system was modeled utilizing MCNP5 and MCNPX. Version α of the model was utilized for the calculations. Neutron shielding between the neutron generator and the NaI detectors minimizes the detector's activation and consequentially, reduces the background in the gamma-ray spectrum. The volume of the soil modeled was 250 cm

by 200 cm by 60 cm deep. The neutron generator, shielding, and detectors are 30 cm above the soil's surface. The composition of the soil used in these simulations consisted of the top thirteen elements from the median value of world soils (App. A), with a bulk density of 1.4 g cm^{-3} and 2% by weight carbon.

The carbon inelastic scattering reaction rates, Equation 5.1, were calculated separately for every cubic centimeter, or voxel, of the soil's volume. The FM, tally multiplier, card was used to calculate the RR in the voxels. The calculated reaction rates are given as reactions cm^{-3} source $particle^{-1}$ by the codes.

$$R_t = N \int_o^\infty \sigma_i(E)\phi(E)dE \tag{5.1}$$

where R_i = the rate of neutron interactions of type *i* (reactions cm^{-3} $second^{-1}$)

$\sigma_i(E)$ = the interaction cross-section (barns)

$\phi(E)$ = the neutron flux (neutrons cm^{-2} $second^{-1}$)

N = number density (atoms $barn^{-1}$ cm^{-1})

The FM card requires the entry of the number density (N_i) of the element that in a mixture, such as soil, depends on the density of the mixture and the weight percent of the material in it (Eq. 5.2). The number density of carbon in a soil with a bulk density of 1.4 g cm^{-3} and 2% carbon by weight is 1.405×10^{-3} in units of atoms b^{-1} cm^{-1}.

$$N_i = \frac{w_i \rho_{mix} N_A}{100 M_i} \tag{5.2}$$

where N_i = number density of element (atoms b^{-1} cm^{-1})

w_i = weight percent of element in mixture (%)

ρ_{mix} = density of mixture (g cm^{-3})

N_A = Avogadro's Number (0.6022 atoms cm^2 $mole^{-1}$ b^{-1})

M_i = molecular mass of element (atomic mass unit)

5.5. RESULTS AND DISCUSSION

Five tally locations were chosen in the soil volume for comparing the RR values obtained from the different tallying options, as illustrated in Figure 2.6. Individual voxel RRs were calculated at these locations to validate the values from the large tally calculations. The results of the tallies are given in Table 5.2 The lattice tally's computation time was too long to completely execute 100 million particles. The elapsed time versus the number of particles at the start was plotted for several points and a linear regression line was fit to the plot (Fig. 5.2). The computation time for a complete execution was estimated by solving the equation of the fit linear regression line. The computation times from all the tallies are given in Table 5.3.

Table 5.2. The carbon inelastic reaction rates at various locations in the soil volume, calculated utilizing the different tallying options in MCNP5 and MCNPX. There are no values for the lattice tally as the computation time was excessively long and, therefore, a full run was not completed.

Tally	Carbon RR (reactions cm^{-2} (source n)$^{-1}$)	σ
-99.5, -99.5, 49.5		
Regular	9.93×10^{-12}	3.35×10^{-12}
Lattice	---	---
FLT	1.82×10^{-11}	5.65×10^{-12}
Mesh	9.93×10^{-12}	3.35×10^{-12}
-99.5, 149.5, 49.5		
Regular	3.33×10^{-12}	2.40×10^{-12}
Lattice	---	---
FLT	3.24×10^{-12}	2.51×10^{-12}
Mesh	3.02×10^{-12}	2.13×10^{-12}
99.5, 149.5, 0.5		
Regular	4.27×10^{-10}	0.34×10^{-10}
Lattice	---	---
FLT	4.23×10^{-10}	0.33×10^{-10}
Mesh	4.24×10^{-10}	0.34×10^{-10}
99.5, -99.5, 0.5		
Regular	1.12×10^{-9}	0.05×10^{-9}
Lattice	---	---
FLT	1.15×10^{-9}	0.05×10^{-9}
Mesh	1.12×10^{-9}	0.05×10^{-9}
0, 0, 25.5		
Regular	4.60×10^{-9}	0.11×10^{-9}
Lattice	---	---
FLT	4.52×10^{-9}	0.11×10^{-9}
Mesh	4.59×10^{-9}	0.11×10^{-9}

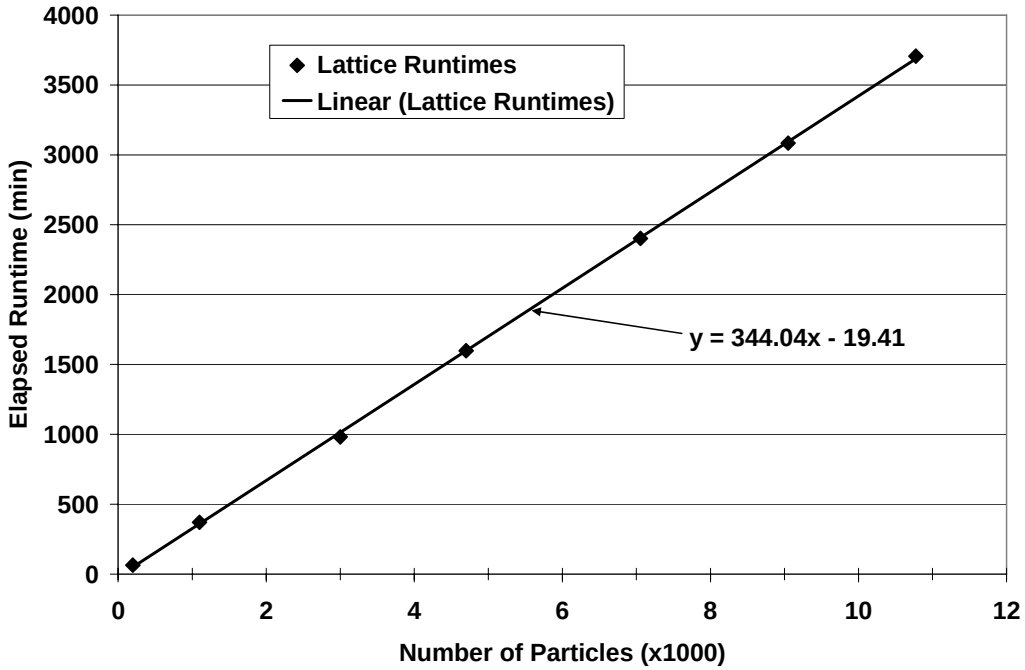

Figure 5.2. The plot of the elapsed time versus the number of particles started for the regular lattice tally, and the linear regression line fit to the plot, along with its equation. The equation was used to estimate the computation time of a complete lattice-tally run [Doron, 2008].

Table 5.3. The computation times for the different tally options utilized in MCNP5 and MCNPX on a 3.2 GHz PC.

Tally	Time (min)	Number of Tallies
Regular	384	5
Lattice*	3.34×10^7 (63 years)	2.5×10^6
FLT	624	2.5×10^6
Mesh	387	2.5×10^6

* Tally time estimated from equation fit to linear regression line

The RR values from the FLT and the mesh tally agree with the individual tally results, within the error (σ) calculated by MCNP (Table 5.2). The results from the

regular lattice tally are unavailable because the execution time for a complete run is excessively long, as discussed below. Though the FLT results are within σ of the individual tally results, they diverge more than the results of the mesh tally. Both of the large tally options produce reliable RR numbers versus the individual tallies.

The computation times for the tallies are 387, 624, and 3.34 x 10^7 minutes for the mesh-, FLT-, and lattice-tallies, respectively, on a 3.2 GHz PC (Table 5.3). The individual tallies' computation time was 384 minutes for five tallies. Even though the mesh tally is a factor of two faster than the FLT, it is important to note the same MCNP5 deck run with the regular lattice tally would take approximately 63 years to complete on a 3.2 GHz PC. The output format of the mesh and lattice tally differ: the output of the former is given in a five column table with the X, Y, and Z location of the center of the tally cube, the tally result (RR in our case), and the relative error of the value. This output format is suitable for copying and pasting into a database program or for reading into a math program, such as Matlab®, for further matrix manipulations. The output size of the mesh tally for this problem is a 135MB ASCII file. The lattice output is three lines of text for each voxel. The first line of the output is the lattice index in question, which is independent of the actual coordinate value of the problem geometry, the second line is FM card details, and on the third line are the output and its relative error. An external routine must be written to tabulate the results into a matrix format. The output size of the FLT is 773MB.

The mesh tally is the most accurate one compared to individual tallies; it is the fastest, and has the smallest, most user-friendly output format for importation into other database or math programs. Although the mesh tally is the fastest because it is superimposed on, and not part of a geometry, this can be a disadvantage when introducing morphology into the soil, namely, adding stones, pebbles, or roots to mimic

the real situation. The disadvantage is that the user can incorrectly define the superimposed tallying mesh and mistakenly tally a part of the soil volume that does not contain any stones, for instance. The advantage of the lattice tally is that the specific cells in which stones exist can be called out, reducing the chance of user error.

The FLT tally has the same geometric advantage as the regular lattice tally and can be executed in a reasonable time. However, as of now, it requires the tallying input to be quite specific, and therefore, does not support all the tallying options of the regular lattice. The FLT would be effective for introducing a homogeneous distribution of stones or pebbles.

5.6. CONCLUSIONS

The large tallying options in MCNP5 and MCNPX can be utilized for calculating carbon RR in soil. The mesh tally and FLT also will be valuable for calculating the energy-dependent neutron and gamma fluxes in soil. The combination of these results will help establish the sampled depth, volume, and footprint of the INS system, along with clarifying how these parameters are affected by the soil's bulk density, moisture content, and morphology. The mesh tally presently is the fastest, most user-friendly, and effective option for calculating large tally matrices in a soil volume. However, the FLT is an efficient option for use in introducing certain morphological features into the soil, and may become a more versatile tallying option in future.

Chapter 6: Reaction Rates and Soil Volumes

6.1. NEUTRON TRANSPORT IN SOIL

The goal of this work was to examine the transport of neutrons in soil as a function of time and energy utilizing the MCNPX code. The energy spectrum of the neutrons changes as a function of time and depth in the system. This in turn affects the reaction rates in the soil. Reaction rates are calculated as a function of both time and depth within the system.

6.1.1. System Modeling

The INS system has been modeled utilizing the MCNPX code. Version α of the model was utilized for the calculations. Variance reduction techniques were utilized to improve the performance of the model. The first variance reduction method utilized was to point the source towards the soil so that all particle simulations had the chance to enter the soil volume. The second variance reduction technique was splitting to give neutrons increased weights as they progressed deeper into the soil. Neutron reaction rates were calculated for 1 cm^3 volumes in the soil with F4 tallies. One billion particles were modeled from the source for each of the MCNPX runs.

6.1.2. Results and Discussion

Results showing the effect of time vs. depth in the soil are shown in Figure 6.1. Note that the MCNPX code produces results in time units of shakes (1 shake = 10^{-8} s). The average time for neutrons to escape the system after being released from the source was 2.47 x 10^{-5} s. The average time to capture for neutrons in the soil was 2.22 x10^{-5} s after release. As expected, the data show that the average age (time from release) of neutrons increases with depth in the soil. At a depth of 50 cm in the soil all the neutrons

have an age of 10^{-7} s or greater. By 0.01 s all the neutrons have either escaped the system or have been absorbed.

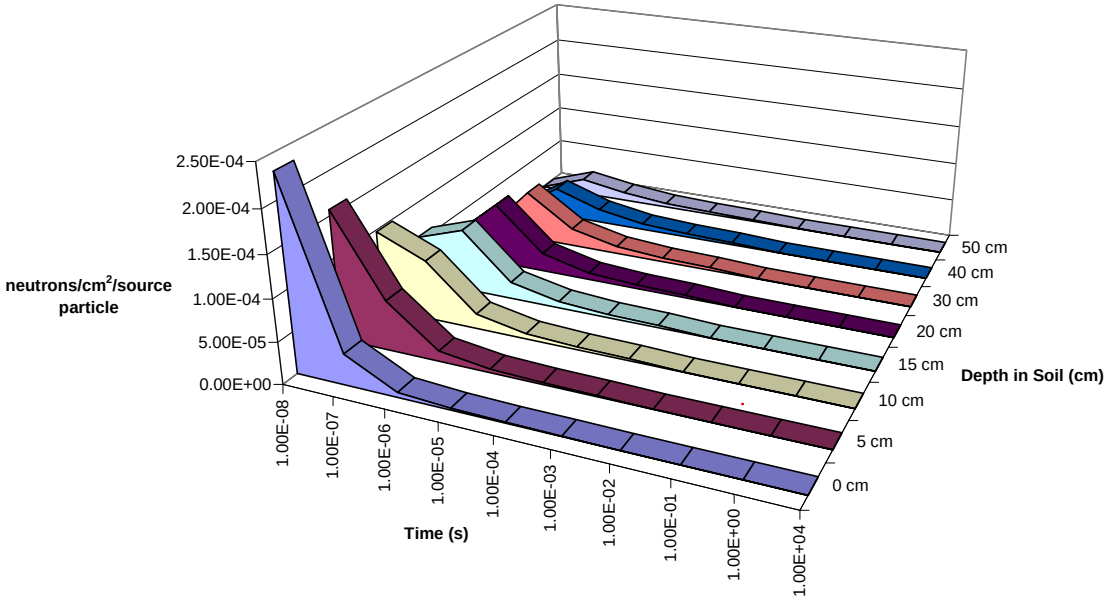

Figure 6.1. Time versus depth of neutrons in soil. The neutrons start with an energy of 14 MeV, but change energy as a result of interactions in the soil [Biegalski, 2008].

Figure 6.2 shows how the energy of neutrons changes as a function of depth in the soil. While the neutron energy spectrum has peaks at both 14 MeV (birth energy) and thermal energies, the ratio of 14 MeV neutrons to thermal energy neutrons significantly changes with respect to soil depth. Figure 6.3 illustrates this thermalization of the neutron population as a function of depth in the soil. The ratio of 14 MeV neutrons to thermal neutrons changes by more than a factor of 100 from the soil surface to a depth of 50 cm.

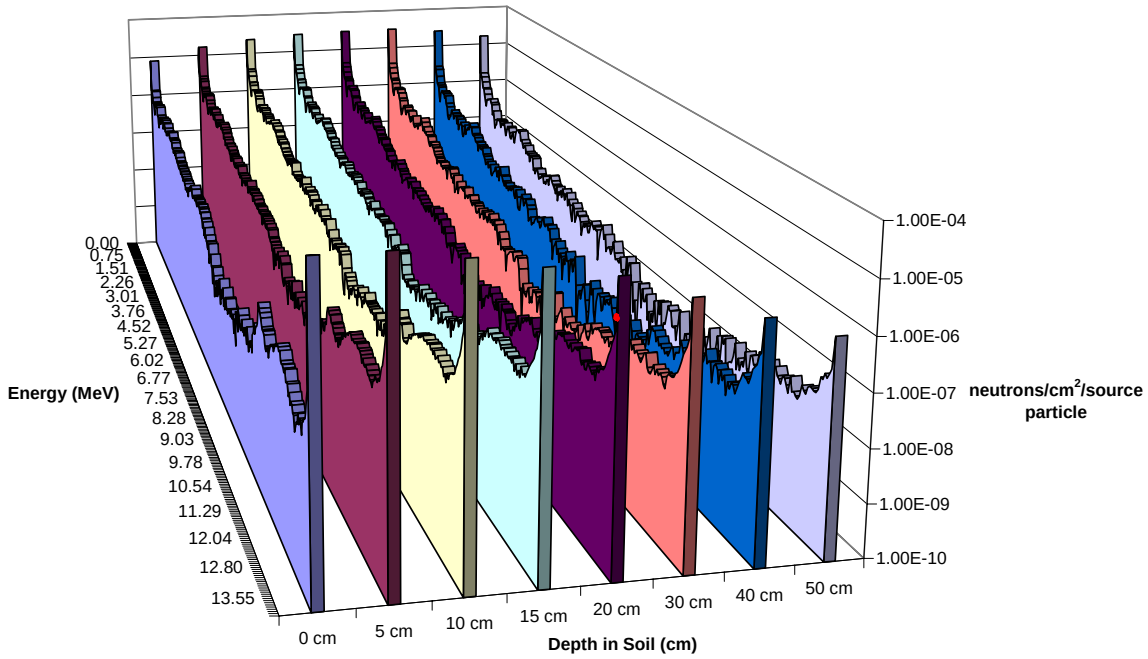

Figure 6.2. Energy versus depth of 14 MeV incident neutrons in soil.

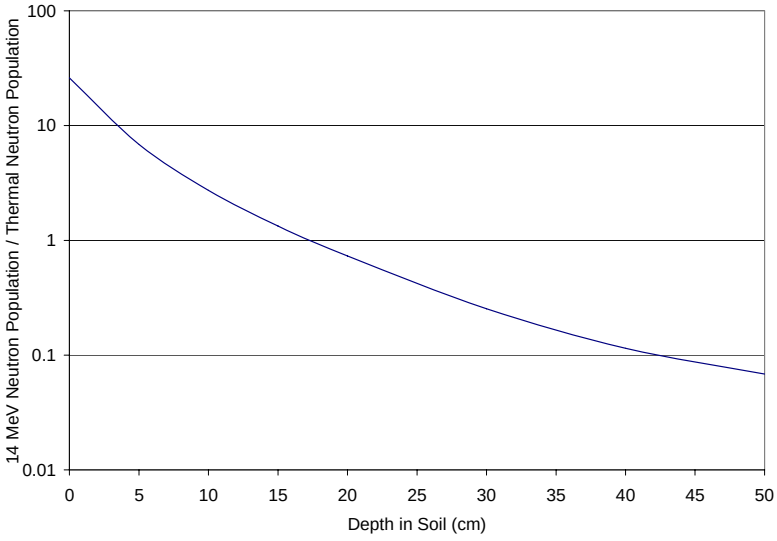

Figure 6.3. Ratio of neutron population with energy of 14 MeV to neutron population with thermal energies as a function of depth in the soil.

Figures 6.4 and 6.5 show how the neutron population thermalizes as a function of both time and depth in the system. Figure 6.4 shows the neutron population at the soil surface and Figure 6.5 shows the neutron population at a depth of 50 cm. After the first neutron time interval of 10^{-7} s no 14 MeV neutrons exist in the system. The 14 MeV neutrons escape, are absorbed, or lose energy through a scattering interaction. By a neutron age of 10^{-6} s, no fast neutrons still exist in the system. By 10^{-5} s, the entire neutron population consists of thermal neutrons. Figures 6.4 and 6.5 also show how the neutron population decreases as a function of depth in the soil.

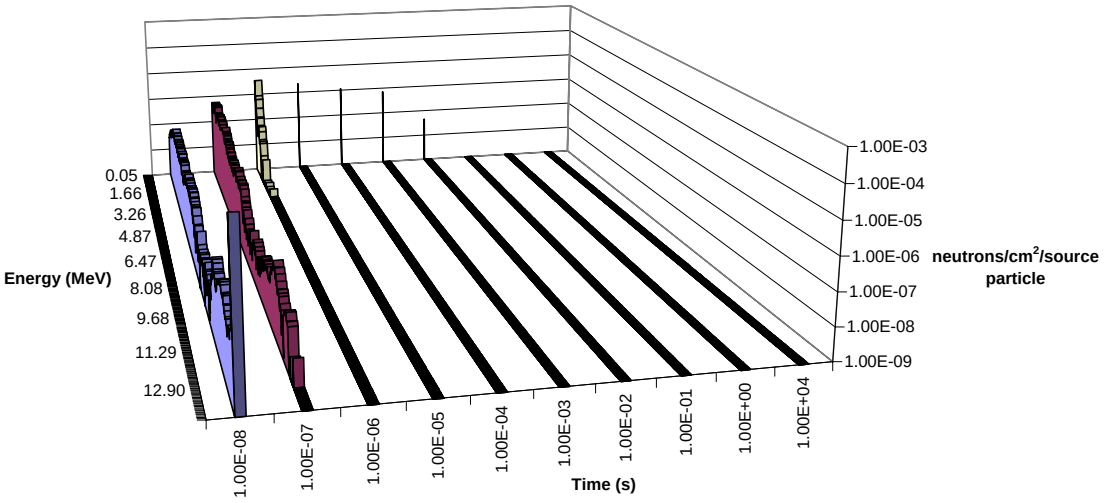

Figure 6.4. Energy versus time at 0 cm depth in soil.

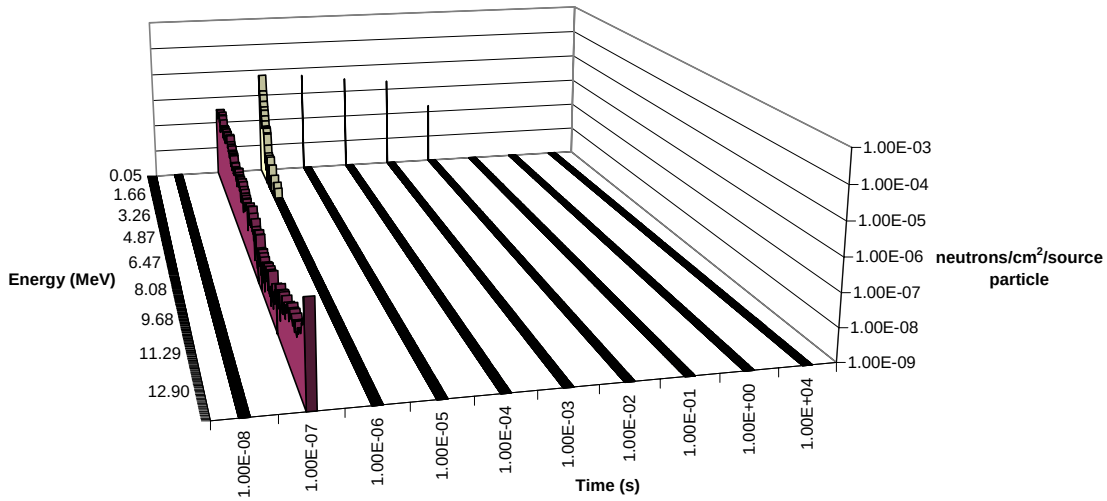

Figure 6.5. Energy versus time at 50 cm depth in soil.

Figures 6.6 and 6.7 show the carbon (n, n' γ) inelastic scattering reaction rates as a function of time within the system. This reaction is of primary interest for the INS system. The carbon (n, n' γ) inelastic scattering reaction is a threshold reaction with a neutron energy cutoff at 4.4 MeV (Fig. F.1). As a result, all the carbon (n, n' γ) inelastic scattering reactions occur with energy between 4.4 MeV and 14 MeV (source energy) within 10^{-6} s after release from the source. At the soil surface the majority of the carbon (n, n' γ) inelastic scattering reactions occur with 14 MeV neutrons within the first 10^{-8} s after leaving the source. At a depth of 50 cm in the system, most of the carbon (n, n' γ) inelastic scattering reactions occur within a time window between 10^{-8} and 10^{-7} s. Since the reactions at different depths are time dependent, one could theoretically determine the depth of a reaction by measuring the time between the neutron release and the photon measurement. However, the time difference appears to be too short to practically

differentiate within the INS system due to the limitations of the electronics and the 25 μs pulse duration.

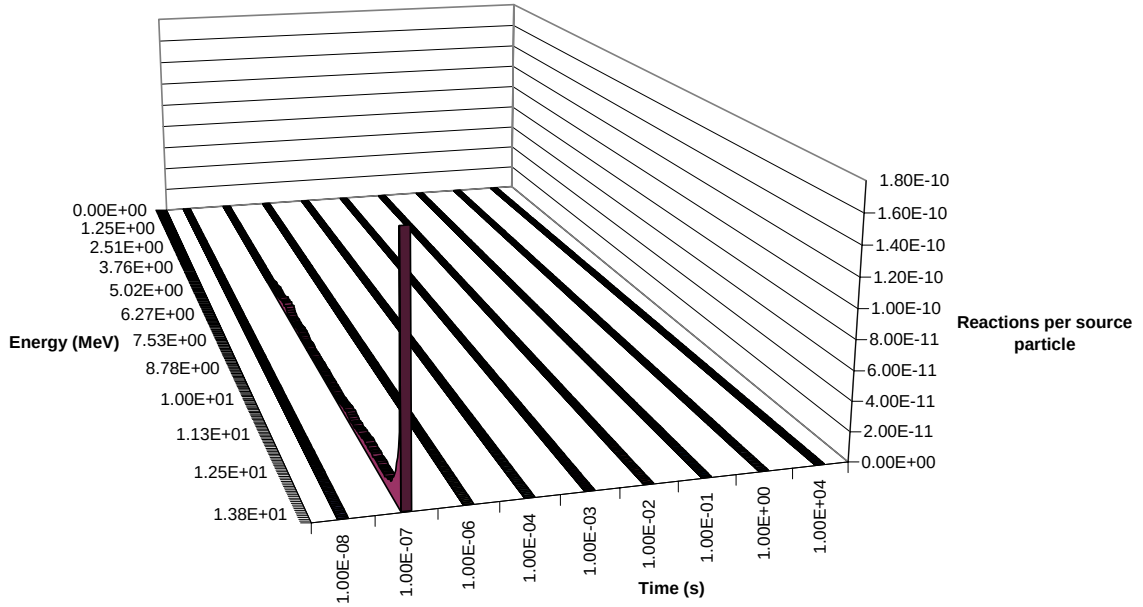

Figure 6.6. Carbon inelastic scattering reaction rate probability at a depth of 0 cm below the neutron source.

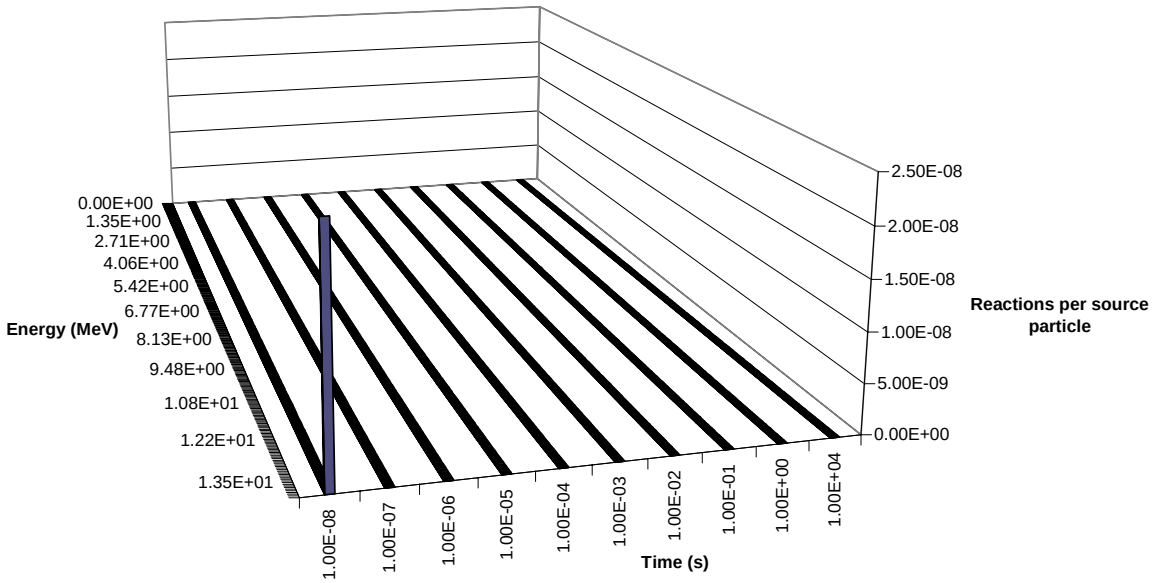

Figure 6.7. Carbon inelastic scattering reaction rate probability at a depth of 50 cm below the neutron source.

This information will be utilized for calculating the reaction rates and optimization of the gating of gamma-ray spectral acquisition times. This information is also required to determine the sampled volume in the soil and should assist in deconvolving the time-dependent gamma-ray signature measured by the NaI detectors. Our results show that after 10^{-6} s, there are no fast neutrons left within the system. After 0.01 s, all the neutrons have either escaped the system, defined as a soil volume of 250 cm by 200 cm by 50 cm deep, or have been absorbed.

6.2. SOIL VOLUME, FOOTPRINT, AND DEPTH

In the pursuit of the soil depth and volume analyzed by the in-situ soil analysis method, a question arose as how to define the effective sampling volume and depth. It was concluded that the volumes and depths of interest would be related to the 90%, 95%, and 99% of the total sampled response volume. MCNP5 and Matlab were utilized in series to complete the desired calculations and plots. Version α of the MCNP model is utilized for these calculations. Carbon inelastic reaction rates were calculated with MCNP5 to a depth of 50 cm. Inelastic gamma-ray attenuation and solid angle from the soil to the detectors was calculated with Matlab. The soil sampling volumes, max depths, footprints, and weights representing the 90, 95, and 99% of the total carbon inelastic gamma-ray activity in the soil was calculated utilizing Matlab, as well. The details of the calculations, along with term definitions and results are presented below.

6.2.1. Reaction Rate

The carbon inelastic scattering reaction rates (Eq. 6.1) are calculated separately for every cubic centimeter, or voxel, of the soil volume. These calculations are performed by MCNP5. The MESHTAL (section 5.3) card is used for volumetric tallying in every voxel and the FM card is used to calculate the carbon inelastic scattering reaction rates in the voxels. The calculated reaction rates in MCNP5 are given as reactions cm^{-2} $(source\ particles)^{-1}$. The result is a five column two dimensional matrix ([RR]) that gives the reaction rates with their relative error for every voxel (App. E).

6.2.2. Matlab

Matlab is utilized for calculating the 5 MeV gamma attenuation ([A]) and solid angle ([Ω]) from every voxel in the soil volume to the detector face. The attenuation and solid angle matrices are then point multiplied by the reaction rate matrix. This calculation gives the final calculated probability of a carbon inelastic scattering gamma ray arriving at the detector face. The steps to performing these calculations are explained below.

The first step taken is to read the MCNP5 two dimensional output matrix into Matlab and convert the matrix into three dimensional space within Matlab. Next the attenuation from every voxel in the soil volume is calculated.

6.2.3. Geometric Calculations

To calculate attenuation from every voxel a set of geometric equations were derived. An equation to calculate the material attenuation distance, r, and an equation to calculate the 1 R^{-2} attenuation distance, R. The geometry calculated is shown in Figure 6.8. The derivation of the equations is given below.

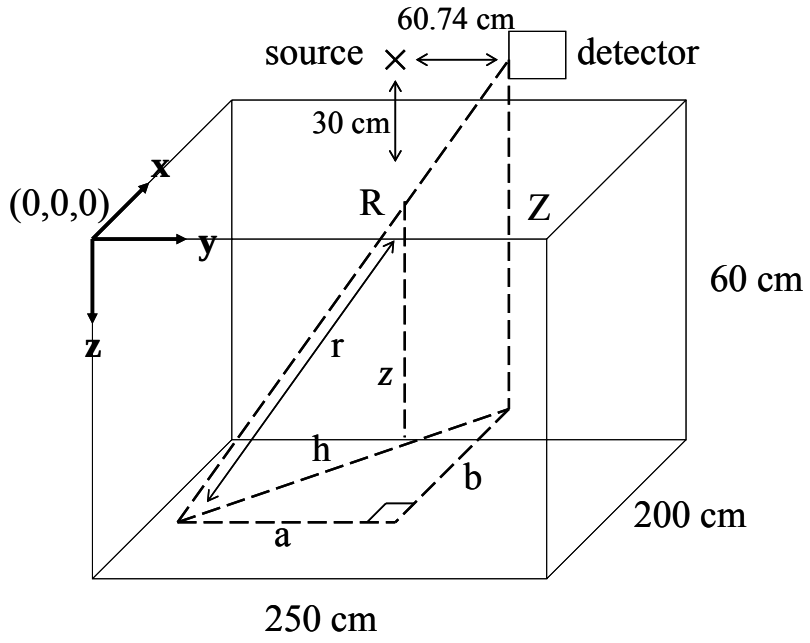

Figure 6.8. Soil geometry used for attenuation calculations in Matlab.

1/R^2 attenuation distance:

$$R = \sqrt{h^2 + Z^2} \tag{6.1}$$

$$h = \sqrt{a^2 + b^2} \tag{6.2}$$

substituting equation 6.2 into equation 6.1:

$$R = \sqrt{\left(\sqrt{a^2 + b^2}\right)^2 + Z^2}$$

$$R = \sqrt{a^2 + b^2 + Z^2} \tag{6.3}$$

Material attenuation distance:

using the rule of like triangles:

$$\frac{R}{Z} = \frac{r}{z} \tag{6.4}$$

$$r = \frac{R * z}{Z} \tag{6.5}$$

$$R = \sqrt{(150 - x + 61.74)^2 + (150 - y)^2 + (z + 30)^2} \tag{6.6}$$

$$r = \frac{R * z}{(z + 30)} \tag{6.7}$$

with: $Z = z + 30$

$a = |150 - x + 61.74|$

$b = 150 - y$

These general geometric equations are entered into Matlab. The carbon inelastic gamma ray attenuation from every voxel to the detector face can now be calculated utilizing Equation 6.8, given below.

$$Attenuation = \frac{\exp(\left(-\frac{\mu}{\rho} * \rho\right) * r)}{4\pi R^2} \tag{6.8}$$

with μ/ρ = 0.28 cm^2 g^{-1} for 5 MeV gamma rays and ρ = 1.4 g cm^{-3}.

The Attenuation coefficient, μ/ρ, for the soil was calculated for the soil for 5 MeV gammas utilizing Equation 6.9. The carbon inelastic scattering gammas are 4.4 MeV. Only the six most abundant soil elements were considered in the calculation. The calculations are summarized in table 6.1.

$$\frac{\mu}{\rho} = \frac{\mu_1}{\rho_1} * w_1 + \frac{\mu_2}{\rho_2} * w_2 + ... + \frac{\mu_i}{\rho_i} * w_i \qquad (6.9)$$

Where μ_i/ρ_i = Soil attenuation Coefficient ($cm^2\ g^{-1}$) of element *i*

ρ_i = Density ($g\ cm^{-3}$) of element *i*

w_i = Weight concentration of element *i*

Table 6.1. Summary of attenuation coefficient calculations. [Shultis, 2000]

Element	wt ratio	μ/ρ @ 1 MeV ($cm^2\ g^{-1}$)	μ/ρ @ 5 MeV ($cm^2\ g^{-1}$)	μ/ρ @ 10 MeV ($cm^2\ g^{-1}$)
^{8}O	53.02	0.0637	0.0278	0.0207
^{14}Si	43.76	0.0634	0.0296	0.0244
^{13}Al	1.096	0.0613	0.0283	0.0230
^{26}Fe	0.724	0.0595	0.0315	0.0298
^{11}Na	0.245	0.0609	0.0275	0.0217
^{19}K	0.225	0.0619	0.0306	0.0270
Total		**0.0629**	**0.0284**	**0.0222**

The attenuation matrix and the reaction rate matrix are point multiplied. Point multiplying (*.) instructs Matlab to multiply each corresponding geometric point in the two matrices by each other. The result is another matrix in three dimensional space giving the combined probability of both generating a carbon inelastic scattering gamma and that this gamma will make it to the detector face ([R]). The calculation is given below as Equation 6.10 in matrix notation.

$$[RR] *. [A] *. [\Omega] = [R] \qquad (6.10)$$

6.2.4. Soil Volume Calculations

The calculation of the soil volumes is based on the fact that every data point in the reaction rate and response matrices represents a 1 cm^3 voxel. For the description of the

calculation, the 90% response volume calculation will be used as an example. Matrix [R] is manipulated in Matlab. The matrix is summed and normalized with its sum. The matrix is reshaped to a vector of dimensions (2.5e6, 1). The vector is then sorted in ascending order. The sorted vector is cumulatively summed, so that the first number in the summed matrix is the same as the first number in the original single column matrix, and that the last number is one. The index of the cumulative sum approximately equal to 0.1 or 10% is found. This index represents the number of cells that make up the 10% response from the lowest valued numbers. This number is then subtracted from 2.5e6 (the total number indices in the vector). The result is the number of cells that make up the 90% of the total response, and since each cell represents 1 cm^3, this number is also the volume, *e.g.* the index for 10% may equal 2e6 this then correlates to the 90% volume being 5e5 cm^2.

Next, the plots of the volumes were created as follows. The value in the sorted (not summed) vector at the index corresponding to the 10% volume is found. All the indices in the normalized matrix with the 10% value or lower are set to zero. The Matlab plotting feature of isosurface can now be used on the normalized matrix that includes the zeroed points. The isosurface plotting feature creates a contour plot that connects the data points that share a specific isovalue (zero being the isovalue in this case). This enables the creation of plots representing the soil volume contributing to 90, 95, and 99% of the total carbon gamma ray signal at the detector volume (Fig 6.9).

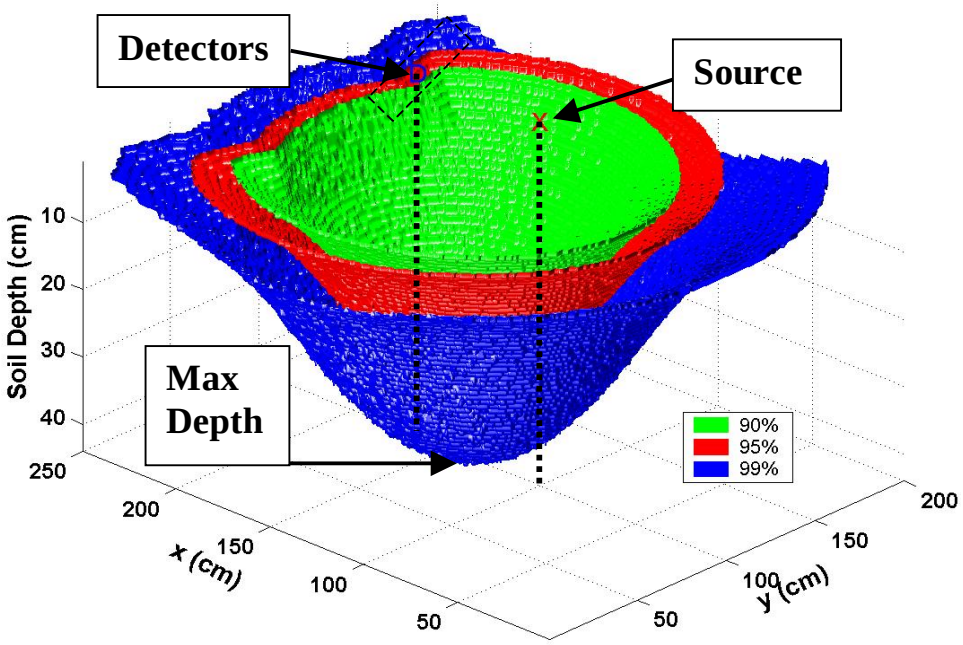

Figure 6.9. Volumes contributing to the 90, 95, & 99% of the total carbon inelastic gamma ray flux intercepting the detectors. The approximate locations of the detectors, neutron source, and maximum depth area also shown on the plot.

6.2.5. Results and discussion

The soil volumes of the 90, 95, and 99% of the total carbon inelastic gamma ray flux intercepting the detector are calculated. The 90, 95, and 99% of the total carbon inelastic gamma ray flux intercepting the detector, represents the soil volume contributing the specified percent to this total flux. The maximum depth and footprint can be found from the isosurface volume plots. The maximum depth is defined as the greatest depths that the volume plots extend to in the soil (Fig. 6.9). The footprint is defined as the area of the projection of the soil volume on the soil surface and is measured in units of meters squared. The weight of the sampled volume is calculated by multiplying the sampled volume times the soil bulk density. The tabulated results of the calculations for the 90,

95 and 99% sampled volumes with a soil bulk density of 1.4 g cm^{-3} are given below in Table 6.2.

Table 6.2. Parameters of the 90, 95, and 99% of the total carbon inelastic gamma ray flux intercepting the detectors assuming soil bulk density of 1.4 g cm^{-3}.

% of Sampled Volume	Depth (cm)	Footprint (m^2)	Volume (m^3)	Mass (kg)
90	24	2.100	0.223	311.54
95	30	2.970	0.359	502.73
99	43	4.870	0.777	1087.16

In Table 6.2 it can be observed that the volume of the 99% of the total gamma ray flux intercepting the detector is more than a factor of three greater than that of the 90% of the total, and the 99% depths is almost twice as deep as the 90% depths. The plotting of the volumes representing 90, 95, and 99% in Figure 6.9, gives insight to the geometry of the volume that the system is sampling. The geometry of volumes is oval in shape and relatively symmetrical about approximately the midpoint between the source and the detectors.

Chapter 7: Model Benchmarking

Any model of a real world system must be tested and benchmarked experimentally in a controlled setting. MCNP must not be operated as a black box, since the results of the model will only be as good as the input. Model benchmarking provides the evidence for whether a model may be relied on to predict real world solutions. In this chapter several benchmark experiments are presented that were performed for the MCNP5 model of the INS system. The benchmarks each concentrate on a specific part of the model. The accepted standard in literature pertaining to MCNP benchmarking is to achieve an accuracy of less than 10% between real and modeled experiments [Choi, 2004; Roh, 2000].

7.1. FLUX FOIL EXPERIMENT

A neutron flux foil experiment was performed to benchmark the MCNP5 modeling of the neutron transport of the system. MF Physics Corporation, the manufacturer of the specific NG that is utilized for the system, published a technical bulletin relating a technique to experimentally measure the output of the neutron generator [MF Physics Corp]. The method that MF Physics utilizes is The Texas Convention technique for measuring neutron generator output [Heath, 1965]. The reaction utilized is the ^{63}Cu (n,2n)^{62}Cu reaction with an 11.3 MeV threshold, a cross-section of ~500 millibarns at 14 MeV (Fig. F.2), and a half-life of 9.9 minutes. The measurement method is standard and was completed through an irradiation and counting method. The copper flux monitor is irradiated at a given location with respect to the NG, and once active, it is counted on a gamma detector. The detector outputs a gamma spectrum with peaks at specific energies and magnitudes given in counts. The counts can be calculated per second, and correspond to disintegrations per second, or the activity of

the isotope. The flux can be calculated with this activity, the properties of the copper flux monitor, and the constants of the experiment. A simplified explanation of the method used to calculate flux will be given with equations below. We start with the equation calculating neutron flux (Eq. 7.1):

$$\phi = \frac{\lambda C\left(\frac{C_R}{C_L}\right)}{(\gamma\varepsilon\sigma N)\left(1-e^{(-\lambda t_{irr})}\right)\left(e^{(-\lambda t_d)}\right)\left(1-e^{(-\lambda C_R)}\right)} \quad (7.1)$$

where: ϕ is the calculated flux in neutrons cm^{-2} s^{-1}

λ is the decay constant of the isotope in s^{-1}

C is the total number of counts

C_R is the real counting time in seconds

C_L is the live counting time in seconds

γ is the gamma yield

ε is the detector efficiency

σ is the microscopic cross section of the isotope in cm^2

N is the number of atoms in the sample

t_{irr} is the irradiation time of the flux monitor in seconds

t_d is the decay time from the end of irradiation to the beginning of counting in seconds

In equation 7.2, the decay constant is equal to:

$$\lambda = \frac{\ln 2}{t_{1/2}} \quad (7.2)$$

where: $t_{1/2}$ is the half life of the isotope in seconds

Also the number of atoms in the equation is given in equation 7.3 as follows:

$$N = \frac{mN_a}{M} \tag{7.3}$$

where: m is the mass of the flux monitor (grams)

N_a is Avogadro's number

M is the elemental mass of the isotope (amu)

Finally to extrapolate back the neutron output at the NG target line, the flux calculated with equation 7.1 is multiplied by $4\pi R^2$:

$$Output_{NG} = \phi * 4\pi R^2 \tag{7.4}$$

Where: NG output is neutron per second

ϕ is the calculated flux at the copper foil in neutrons cm^{-2} s^{-1}

R is the distance from the foil to the center of NG target line in cm

The disintegration mode of ^{62}Cu is positron emission 97.43% of the time. The energy that is counted is the positron annihilation energy of 511 keV. The detector efficiency (ε) is calculated by counting a ^{22}Na source of known activity on the detector that was used. ^{22}Na is also a strong positron emitter, decay by positron emission nearly 90% of the time. A combined geometric and peak efficiency number was calculated as 0.11 (App. H). The flux Equation 7.1 accounts for the flux monitor's decay during irradiation, from the end of irradiation to the beginning of counting, and during the counting. Plugging all the above information into the flux equation gives us the

calculated flux of the NG at the target line. The experimentally calculated is compared to an F4 neutron tally result from MCNP5.

7.1.1. Experimental

The copper foils were 99.9% pure copper, 0.1 cm thick by 2 cm diameter. All the foils weighted the same at 3.29g. Four experiments were performed, with the copper foil at different locations each time; (a) the foil was placed on the soil directly below the target line of the NG, (b), on the soil surface 7.5 cm away from the target line (c) 13 cm depth and 7.5 cm away from the target line, and (d) 18 cm depth in the soil and 13 cm away from the target line (Fig. 7.1). The counting system included a well-type NaI(Tl) scintillation detector, a multi channel analyzer (MCA), a pre-amp, an amp, and a high-voltage power supply (Fig. 7.2). Version β is utilized for the calculations along with a copper foil at the experimental positions and the neutron flux above the reaction threshold is tallied. The NG output calculated from the experimental flux at position 'a' was taken as the "true" output of the generator (Eq. 7.4). All of the MCNP5 results are multiplied by the NG output to convert the flux in n cm^{-2} (source particle)$^{-1}$ to n cm^{-2} s^{-1}. The MCNP5 and experimental fluxes at the copper foils can then be compared.

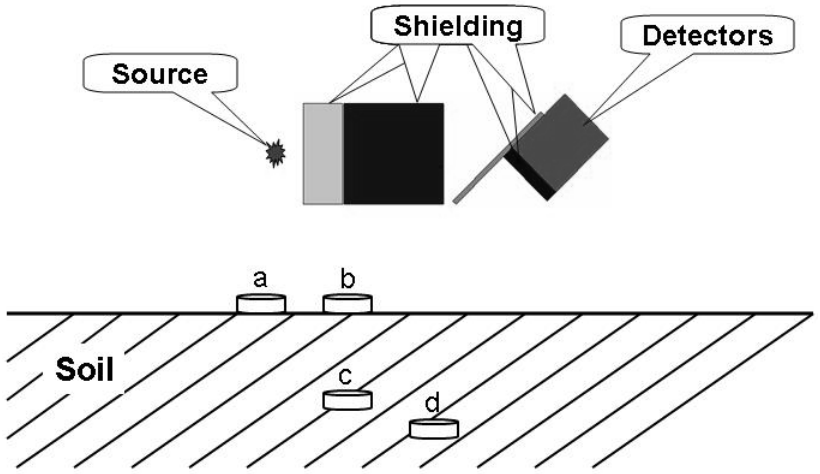

Figure 7.1. The approximate placement of the four copper flux foils, not to scale.

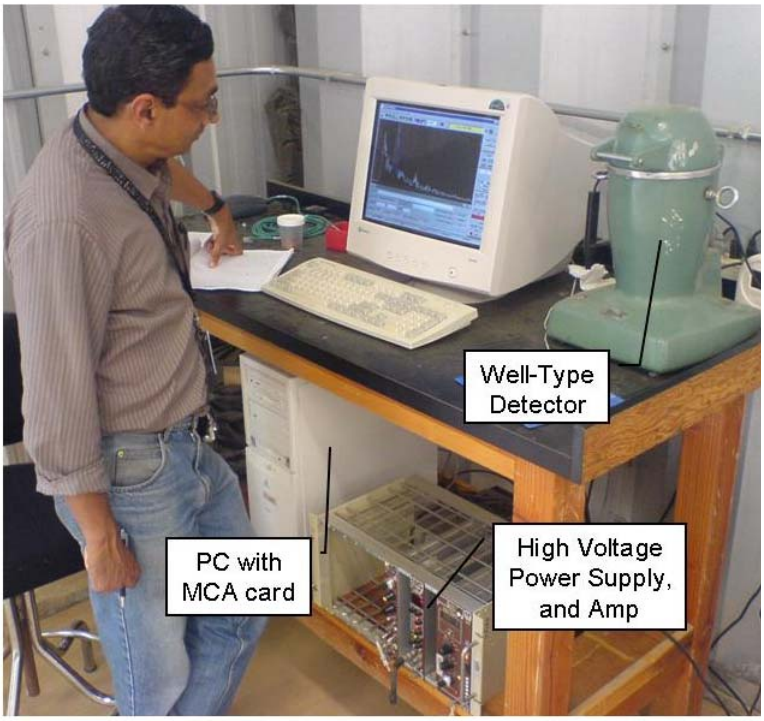

Figure 7.2. The counting system setup for the copper flux foils experiments.

7.1.2. Results and Discussion

Table 7.1 is an Excel spreadsheet of all the data necessary for calculating the flux that each sample experienced. Table 7.1 specifically, is the calculation for the copper foil at position 'a'. The NG output at position 'a' calculated with Equation 7.4 is 1.35×10^{7} n s^{-1}. There is an identical spreadsheet for each sample. The experimental and MCNP5 results are given in Table 7.2. The results all have a delta less than 10%. The small differences in the results can be attributed to two major sources of error, human error and low counting statistics. The placement of the copper foils and the subsequent measurement of their location in the experiment were not precise and would inevitable lead to incorrect geometric modeling of the foils location in MCNP5. The neutron flux that the foils at positions 'c' and 'd' experienced is nearly a factor of three lower than the foils on the surface at positions 'a' and 'b'. The lower neutron flux lead to lower activation and as a result lower counting statistics. Overall, the results are in good agreement.

Table 7.1. Excel spreadsheet of copper foil at position 'a' shown with all the necessary data to calculate the fast flux at the copper foils and the NG output.

$^{63}Cu(n,2n)^{62}Cu$	511 keV Line	
Half-life	9.9	min
	594	s
Decay Constant	0.001166914	1/s
Irradiation Time	3600	s
Decay	30	s
Collect (real time)	600	s
Collect (live)	600	s
Energy	511	keV
Efficiency	0.11	
Counts	712	counts
Counts (+/-)	103	counts
Gamma yield	0.972	
mass	3.29	grams
Cu-63 cross-section	0.480	barns
(n,2n)	4.8E-25	cm^2
Number of Atoms	3.1181E+22	atoms
Source Distance	33.9725	cm
Flux at Foil	**1084.17**	$n\ cm^{-2}\ s^{-1}$
NG Output	**1.57E+07**	$n\ s^{-1}$

Table 7.2. The calculated neutron flux (above 11.3 MeV threshold) the copper foils were exposed to. * Errors less than 1%.

	Flux @ Foil ($n\ cm^{-2}\ s^{-1}$)			
Position	**Field**	**σ**	**MCNP***	**Δ (%)**
a	1084	152	1151	5.82
b	1020	122	1078	5.39
c	376	130	387	2.81
d	294	87	269	9.26

7.2. SAND WITH CARBON CALIBRATION

The number of carbon gamma rays in the ROI represents the carbon concentration in soil that entails the solution of the transport equation. Therefore, the calibration of the system for various soil types and soil conditions must be performed in order to determine

the relation of carbon concentration to the number of gammas in the ROI. For that purpose a calibration curve for dry sand (silica) with increasing carbon concentrations from 0 gC cm^{-3} to 0.14 gC cm^{-3} was derived experimentally and simulated by the MCNP5 code. Version α of the model was utilized for the calcuations. The results from the simulations are the gamma fluxes that are intercepting the detector volume, and the results from the experiment are the gamma spectrum from the detector and electronics system (Table 7.3). In column 2 of Table 7.3 the carbon region of interest (ROI) gamma flux intercepting the detector volume is given. In column 3, the net is given, in which the background in the carbon ROI (0 gC cm^{-3}) is subtracted from column 2. In column 4, the net from column 3 is normalized to the experimental value of the carbon ROI at a concentration of 0.14 gC cm^{-3}. The normalization in column 4 is given by equation 7.5. The field net carbon ROI is given in column 5.

$$C_i = M_i * \frac{F_4}{M_4} \tag{7.5}$$

Where: C_i = Normalized MCNP net carbon ROI (counts) at a given carbon concentration

M_i = MCNP net carbon ROI gamma flux intercepting detector (γ cm^{-2} source $particle^{-1}$) at a given carbon concentration

M_4 = MCNP net carbon ROI gamma flux intercepting detector with highest measured carbon concentration (0.14 gC cm^{-3})

F_4 = Field net carbon ROI counts with highest carbon concentration (0.14 gC cm^{-3})

Table7.3. Results from the calibration experiment performed.

Carbon concentration ($gC\ cm^{-3}$)	MCNP			Experiment
	4.43 MeV $\gamma\ cm^{-2}$ (source n)$^{-1}$	Net	Normalized C ROI (Counts)	C ROI (Counts)
0.0000	5.60E-08	0.00E+00	0	0
0.0375	8.03E-08	2.43E-08	2466	1976
0.0500	9.08E-08	3.48E-08	3530	---
0.0700	1.03E-07	4.75E-08	4813	4252
0.1400	1.49E-07	9.28E-08	9408	9408

The graph of the results of the experimental and MCNP5 simulation results are plotted in Figure 7.3.

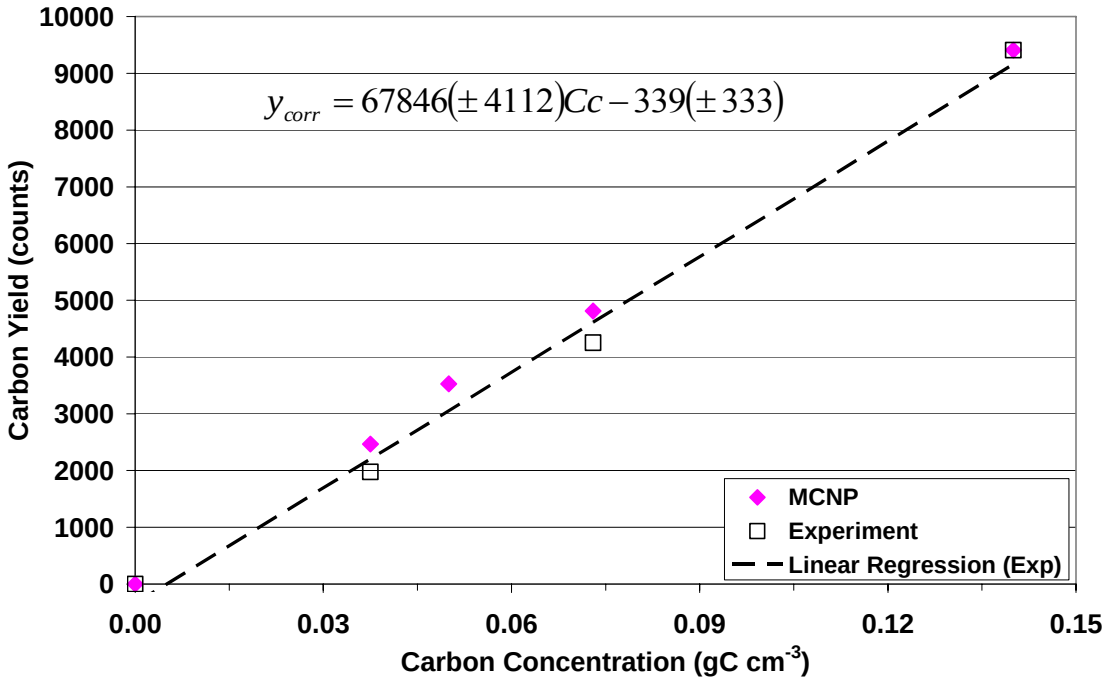

Figure7.3. The normalized results from the MCNP5 calibration calculations plotted with the results from the experimental calibration.

The normalized results from the MCNP5 calibration calculations are in close agreement with the experimental calibration results. The finding suggests an important benchmark of the relative changes in the carbon signal due to changes in soil carbon content.

7.3. Cs and Co Pulse Height

The benchmarking of the detector pulse height (PH) distribution with MCNP5 is a more complicated manner than the benchmarking of the gamma and neutron transport. The PH of a detector is affected by many factors, including but not limited to, crystal size, efficiency, and electronics, which all have to be taken into account in the model. In this section I discuss the benchmarking of the PH distribution of the INS system's three NaI(Tl) scintillation detectors.

7.3.1. Experimental

Two calibration sources of known activity were utilized, namely, a ^{137}Cs (661 keV) and ^{60}Co (1173, 1332 keV) source. The date of creation and activity at creation of the sources was used with Equation 7.6 to calculate the activity of the sources at the time of the experiments [Lieser, 2001]. The Excel spreadsheet with all the data for and the results of the calculations is given in Table 7.4.

$$A = A_o e^{-\lambda t} \tag{7.6}$$

Where A = Activity in Bequerels (Bq), disintegrations per second

A_o = Activity at time zero (Bq)

λ = the decay constant as defined in Eq. 7.2

Table 7.4. Calculation of the ^{60}Co and ^{137}Cs activity at the time of the experiment.

Co-60		
Creation	2-Mar-90	
Present	1-Jun-07	
Time elapsed	31-Mar-17	days
	5.44E+08	seconds
Activitiy (Ao)	0.84	μCi
	3.11E+04	Bq
Half Life	1925.1	days
	1.66E+08	seconds
λ	4.17E-09	sec^{-1}
Activitiy (A)	**3.22E+03**	**Bq**

Cs-137		
Creation	3-Dec-88	
Present	1-Jun-07	
Time elapsed	28-Jun-18	days
	5.84E+08	seconds
Activitiy (Ao)	1.09	μCi
	4.03E+04	Bq
Half Life	30.07	years
	9.48E+08	seconds
λ	7.31E-10	sec^{-1}
Activitiy (A)	**2.63E+04**	**Bq**

Source particles for MCNP, simulating counting for **10** minutes
1.93E+06 particles

Source particles for MCNP, simulating counting for **10** minutes
1.58E+07 particles

Ratio of Co/Cs intensity
0.144

Branching Ration for 0.667 MeV
8.50E-01
number of 0.667 MeV
1.34E+07

A $^{137}Cs^{60}Co$ and a background spectrum were collected for each individual detector separately and the three detectors summed. The energy broadening of the peaks was measured by calculating the full width half maximum (FWHM) of the peaks. FWHM is a measure of the energy resolution of any radiation detector; it is the value of the full energy width of a peak at half the maximum value of that peak [Knolls, 2000]. The FWHM of the detectors is modeled in MCNP5 utilizing a built in Gaussian energy broadening function and version β of the model. The built in function along with the parameters that are entered by the user to MCNP5 are given in Equation 7.7. There are two general ways to solve for the parameters in Equation 7.7; one may setup a system of three equations with three unknowns and solve for the parameters, or create a plot of FWHM versus root E and fit a linear regression to the points. The former method allows for solving of all three parameters including c and the latter method solves for only

parameters a and b. However, both methods of solving were used here and it was found, that for our case, the linear regression fit was adequate, and less time consuming. When solving for the parameters with the latter method the equation becomes Equation 7.8. An example of the linear regression of the sum of detectors 1, 2, and 3 and the fit parameters a and b is given in Figure 7.4. The $^{137}Cs^{60}Co$ sources and the detectors' FWHM were modeled in MCNP5 and PH tallies (F8) were taken for each individual detector and the three detectors summed. Finally, the spectra from the field instrument and model are compared.

$$FWHM = a + b\sqrt{E + cE^2} \tag{7.7}$$

$$= b\sqrt{E} + a \tag{7.8}$$

$$w/c = 0$$

Where a, b, and c are user defined parameters and all units are in terms of MeV [Girard, 2003]

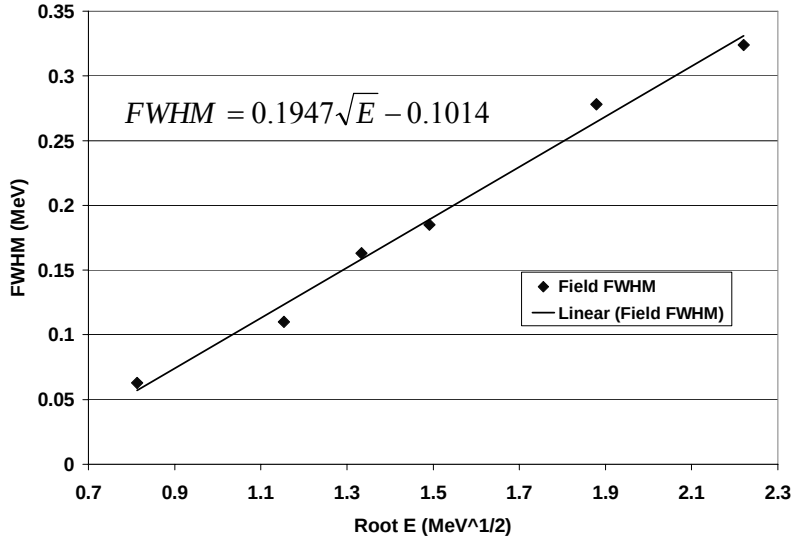

Figure 7.4. The linear regression and equation fit to the FWHM versus root E from the field data. The parameters of the MCNP5 equation are, a=-0.1014, b=0.1947, and c=0.

The $^{137}Cs^{60}Co$ spectra were each collected for 10 minutes and a 12 hour background was collected. The collection of the background was necessary due to natural background radiation that is difficult to model in MCNP5 (Fig. 7.5), therefore being able to subtract the background from the total $^{137}Cs^{60}Co$ spectra will allow for a true comparison of the MCNP5 detector model. The background was taken for 12 hours to allow for good counting statistics. However, it is necessary to normalize the background spectrum prior to subtraction from the total $^{137}Cs^{60}Co$ spectrum, because it was counted for a different length of time than the $^{137}Cs^{60}Co$ spectra. The ratio of the integral counts of the peak-free regions of the two spectra was used for the normalization factor for the background (Channels 800-1024). The integral counts of the peak-free regions of the spectra were chosen to reduce the probability of a photo peak in the normalization ratio calculation. A peak would lead to an incorrect normalization. The normalized background is now subtracted from the $^{137}Cs^{60}Co$ to compare with the modeled spectra. The $^{137}Cs^{60}Co$ source was modeled in MCNP5 and normalized to the disintegrations per second (dps) of the ^{137}Cs and ^{60}Co sources. Finally, the net peak areas of the ^{137}Cs and ^{60}Co peaks from the field and MCNP5 spectra are compared. The net peak areas are equal to the integral counts of the ROI minus the background in the ROI. In this case, the trapezoidal method was utilized to calculate the net peak areas in the ROI (Eq. 7.8).

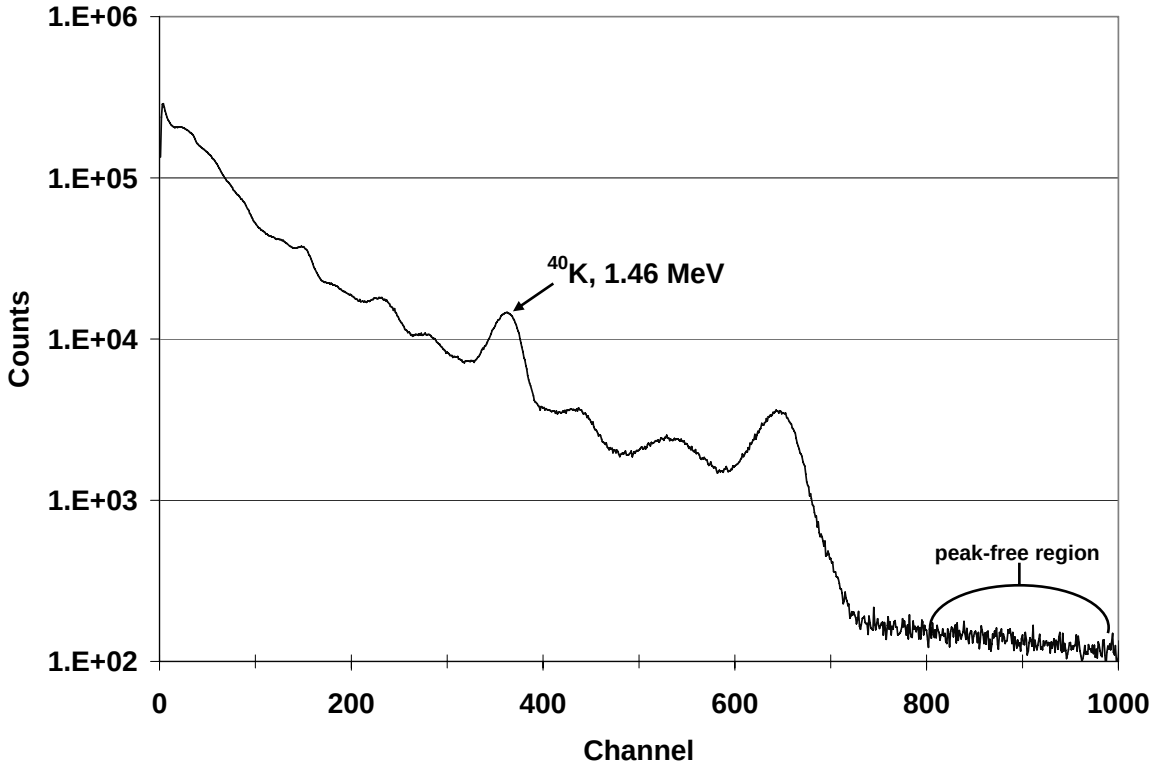

Figure 7.5. Background spectrum counted for 12 hours with detector 3. Labeled on the plot are the strong 1.46 MeV potassium-40 peak, and the peak-free region used for normalization.

$$Net\ Peak\ Area = \sum_{i=Ch_R}^{Ch_L} C_i - (Ch_R - Ch_L)\frac{C_L + C_R}{2} \tag{7.8}$$

where: C_i are the counts from channel i

Ch_L is the left channel of the ROI

Ch_R is the right channel of the ROI

C_L is the counts in the left channel of the ROI

C_R is the counts in the right channel of the ROI

7.3.2. Results and Discussion

The field and modeled $^{137}Cs^{60}Co$ spectra from each individual detector and from the three detectors summed are given below, in Figures 7.6, 7.7, 7.8, and 7.9. The spectra all show good correlation, indicating that both the geometric modeling of the detectors and the calculations of the parameters for the FWHM (Eq.7.8) are correct. The net peak areas of the peaks are compared in Table 7.5. The $^{137}Cs^{60}Co$ sources were placed directly below detector 2 therefore the nets of detectors 1 and 3 are lower than detector 2. The MCNP5 results of detectors 1 and 3 are in better agreement with the field than detector 2. One possible source of error is the measurement of the source location. A relatively small error in measurement, and therefore in modeling, would be less detectable in detectors 1 and 3 than in detector 2 due to its closer proximity to the sources. The modeled spectra are all lower than the experimental spectra at the low energies (<200 keV) of the Compton continuum. The discrepency arises from additional photon scatterings in the experimental data due to extra shielding material that was not modeled in the model, *i.e.* surrounding soil, building materials, etc. Another source of error is the uncertainty of the Monte Carlo simulations of low-energy electrons [Hu-Xia, 2002].

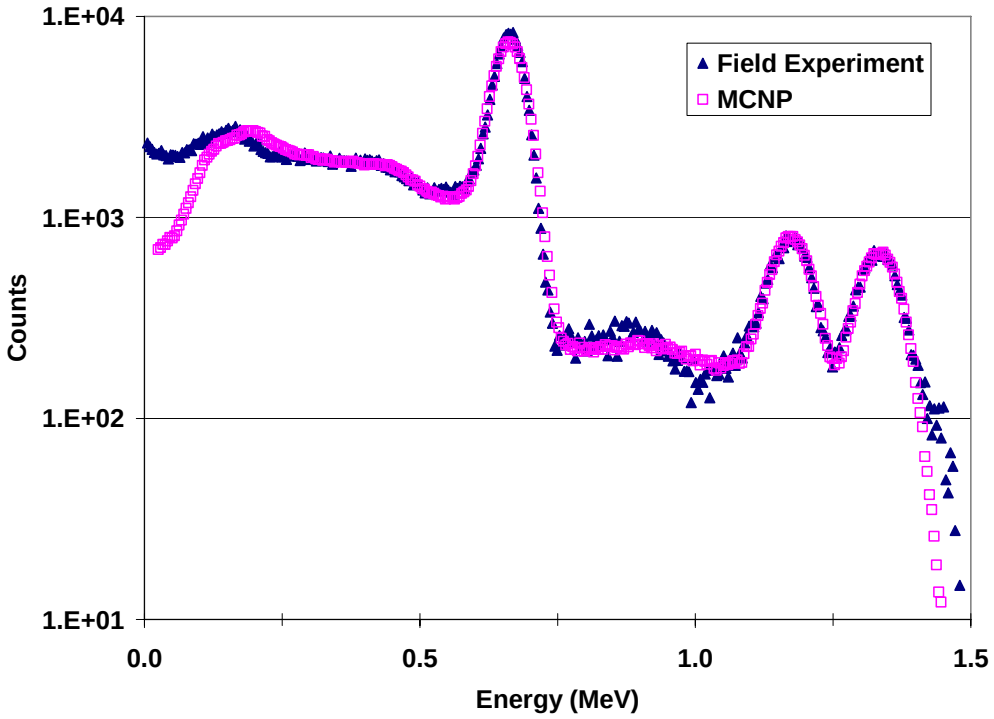

Figure 7.6. Detector 1 $^{137}Cs^{60}Co$ spectra from the field and MCNP5 model.

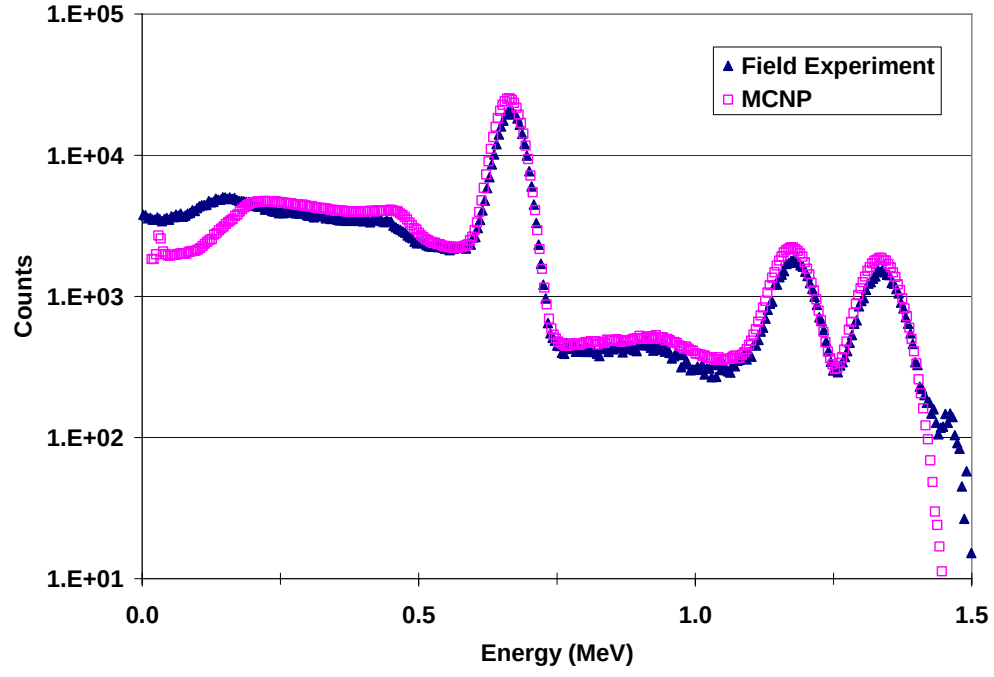

Figure 7.7. Detector 2 $^{137}Cs^{60}Co$ spectra from the field and MCNP5 model.

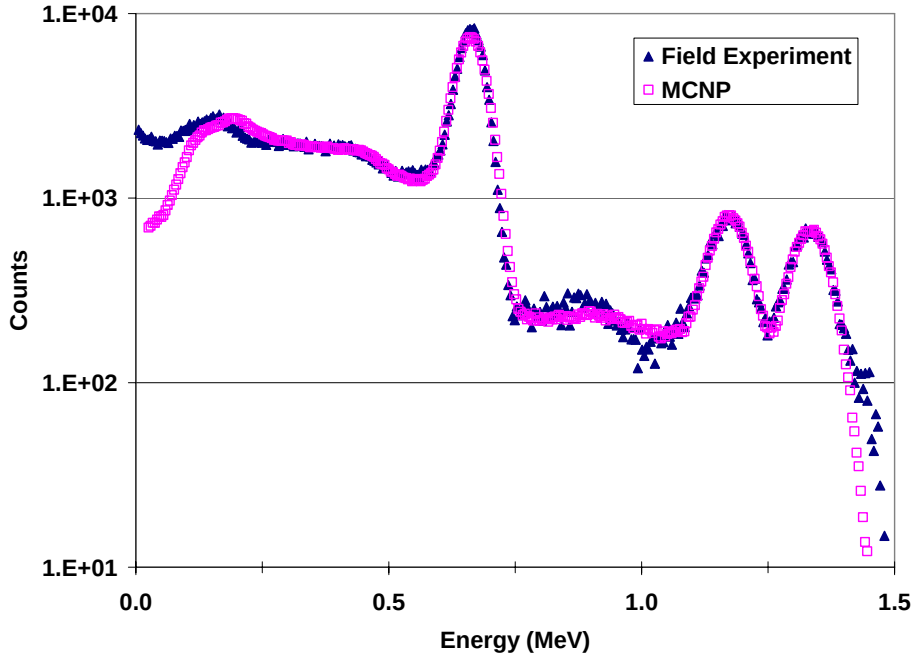

Figure 7.8. Detector 3 $^{137}Cs^{60}Co$ spectra from the field and MCNP5 model.

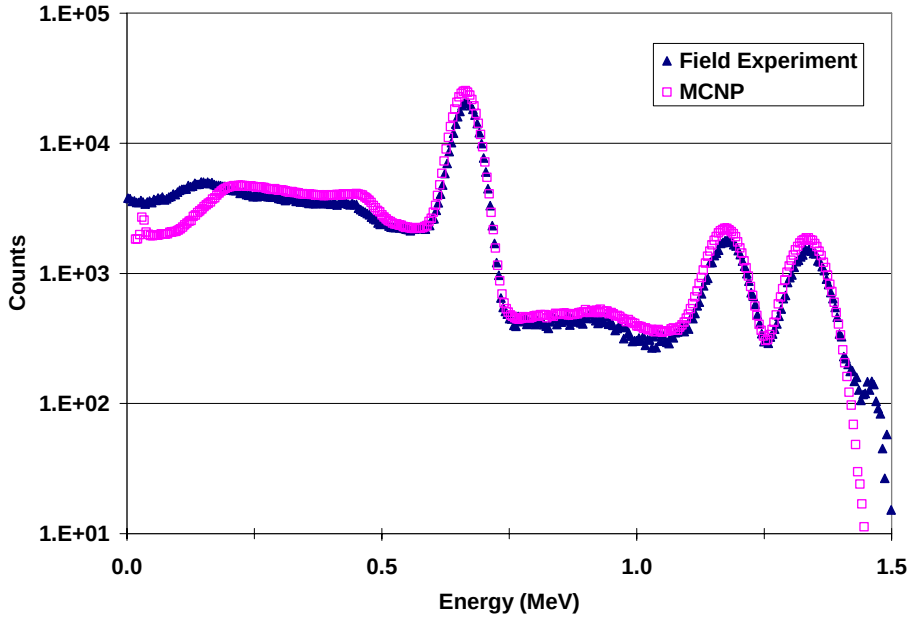

Figure 7.9. The sum of detectors 1,2, and 3 $^{137}Cs^{60}Co$ spectra from the field and MCNP5 model.

Table 7.5. The net peak area of the ^{137}Cs and ^{60}Co peaks from the field and MCNP spectra.

	Detector 1 (Counts)		Detector 2 (Counts)		Detector 3 (Counts)		Detector 123 (Counts)	
Peak	**Field**	**MCNP**	**Field**	**MCNP**	**Field**	**MCNP**	**Field**	**MCNP**
^{137}Cs	92,043	100,141	266,668	338,028	111,667	110,662	497,654	577,480
±	389	402	615	673	427	423	882	930
^{60}Co(1.173)	9,387	10,417	25,738	33,344	10,955	11,578	46,164	52,157
±	154	162	234	254	173	169	332	364
^{60}Co(1.332)	9,288	9,526	24,656	30,512	11,207	10,568	48,283	43,664
±	134	139	209	219	153	145	311	320

7.4. HEIGHT OPTIMIZATION

The height optimization field experiments (Fig. 2.5) were simulated with MCNP5 and the net peak areas for the three ROI's (C, Si, and O) were calculated using the same energy windows as defined for the field measurements. Version β of the model as shown in Figure 2.7 was utilized, however the soil volume was increased considerably to accommodate the for experiment being completed in an open field as opposed to over the soil pits in the soil analysis facility. The soil volume was increased to 800 cm by 800 cm by 60 cm depth. The soil composition, moisture, and density of the field soil are not known; therefore the soil from Appendix A was used. As a result, the absolute quantities should not be taken into account in the results, *i.e.* the silicon net peak areas from the field have the highest values and the oxygen has the highest values for the MCNP5 calculations. The results from the field experiment and MCNP are given in Figure 2.5, and 7.10, respectively.

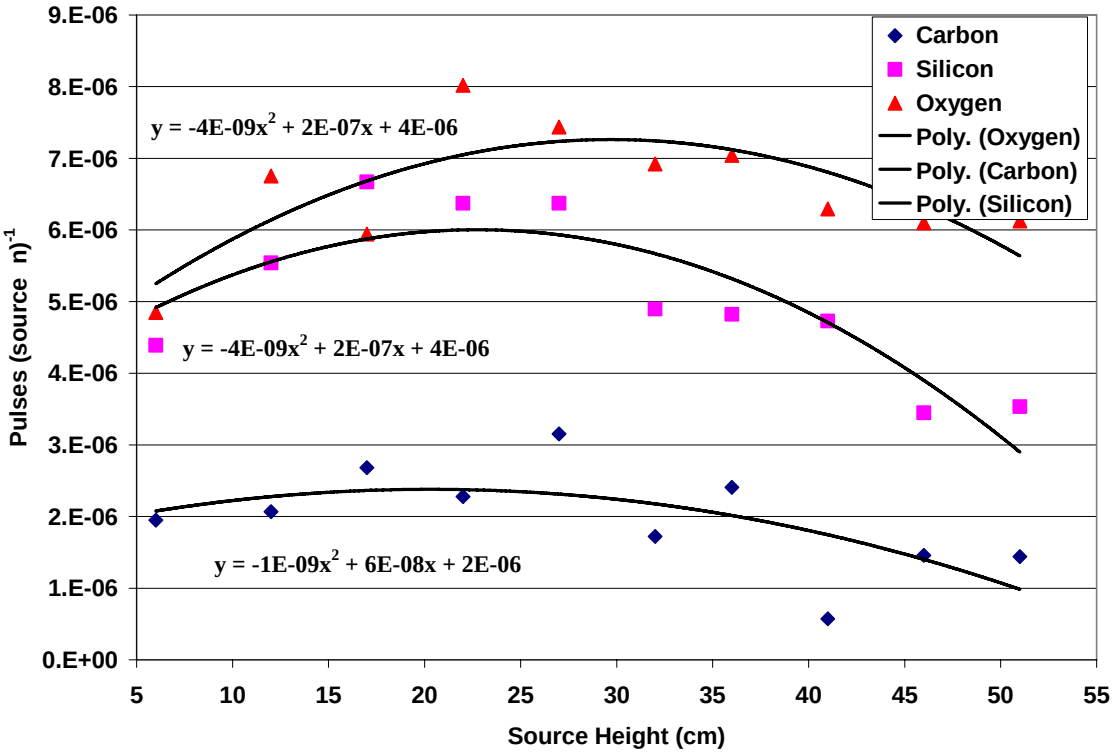

Figure 7.10. The net peak area results form the MCNP simulation of the height optimization.

A second degree polynomial was fit to the net peak areas from silicon, oxygen, and carbon. The maximum source height of each element was calculated by setting the derivative of each polynomial equal to zero and solving for x. The maximum net peak area values for each element from the field experiment are from 30 cm. The silicon and oxygen maximum net peak areas from MCNP5 are at 25 cm and at 30 cm for carbon. The discrepancy is most likely due to human error in measuring the height of the source above the ground in the field experiment. It is important to note that the absolute values of the net peak areas should not be compared between the field and the model.

7.5. CONCLUSION

All the benchmarks presented above demonstrate the models ability to accurately represent the real world system. The desired accuracy of the model is 10% within any of the experimental values. The flux foil experiment shows that the neutron transport of the system is accurately modeled by calculating the neutron fluxes at four different points correctly. The model achieved approximately 6-9% accuracy between the model and experimental values of the flux for the four copper foils. The sand pit calibration emphasizes that the model calculates the same slope for a specific calibration line. The slopes of the regression lines for the modeled and experimental calibration points are within 1%. The $^{137}Cs^{60}Co$ pulse height distributions show that the model accurately produces pulse height distributions for each detector separately and summed. The modeled net peak area values achieved accuracies of less than 8%, 20%, 6%, and 13%, for detector 1, 2, 3, and the three summed, respectively. As discussed above the relatively large error for detector 2 is due to the proximity of the sources to the detector and therefore the model is more sensitive to any human error in the geometric modeling of the source. The error of the three detectors summed was affected as a result of the detector 2 error. Finally, the height optimization experiment demonstrates that the full model produces similar maximum net peak area results for the optimization of the geometry of the system. There was no discrepancy between model and experimental for the optimized heights of the carbon net peak area and a 5 cm discrepancy for the oxygen and silicon heights. The 5 cm is due to human error in measuring the height in the experimental and therefore resulted in the error for the model. The benchmarks all achieved the desired accuracies except the detector 2 spectrum.

Chapter 8: Soil Perturbations

8.1. Soil Moisture and Density Effects

The effects of soil bulk density and moisture content on neutron and gamma-ray transport in soil has been studied using version β of the model. We varied the soil bulk density from 0.5 to 2 g cm^{-3} and the moisture content from 0 to 100% by weight. Noticeable effects on gamma ray yield were observed for this range of variability in the bulk density. However, within the median average density range (1-1.5 g cm^{-3}) in a given soil type the density effect is much reduced. Changes in the soil moisture content affected mainly the low energy range of the neutron transport with minimal changes in the transport of the fast neutrons. However, increased moisture content increased the soil bulk density thus affecting the signal yield. The measured carbon signal depends on the transport conditions of neutrons and gamma rays in the soil matrix, which are affected by the soil moisture and bulk density. While variations in the bulk density affect both the neutrons and the gamma rays attenuation the moisture affects mainly, but not only, the transport of neutrons due to elastic scatterings with hydrogen nuclei. Changes in the transport properties of the soil influence the sampling depths thus affecting the calibration and response function of the INS system.

In this section we assess the magnitude of the effects on the neutron and gamma ray propagation and the resulting carbon measured signal due to variations in the soil bulk density and moisture.

8.1.1. Experimental

The geometry of the modeled INS system depicted in Figure 2.7 contains a NG point source of 14 MeV neutrons, shielding between the source and the NaI detection system,

and an array of NaI detectors. The system was placed 30 cm above the ground with the simulated soil volume of 250 cm by 200 cm by 50 cm deep. The soil composition consisted of the top thirteen soil elements, Table 5.1, from the median value of world soils with a bulk density of 1.4 g cm^{-3} and 2% by weight carbon [Vinogradov, 1959]. In the present simulations the neutrons were traced from the source into the soil and the induced gamma radiation intercepting the detection volume was scored and binned according to their energies. The detector response function was not included in the calculations since the carbon photopeak in the pulse-height distribution is proportional to the number of gamma rays in the region-of-interest (ROI) intercepting the detector volume.

8.1.1.1. Density Variations

Soil bulk density affects the mass attenuation of the neutron and gamma ray transport in the soil. The dry bulk density of the modeled soil was varied from 0.25 to 2 g cm^{-3} maintaining a constant carbon concentration. The range was chosen to encompass the density range of highly organic soils (0.25 g cm^{-3}) to solidified earths (1.8 g cm^{-3}), with an average bulk density range from 1.2 to 1.6 g cm^{-3} [Frank, 1993]. The density effects on the neutron transport were modeled by monitoring the fast neutron flux (5-14 MeV) at depths of 0, 5, 10, 20, 30, and 50 cm in the soil volume. To observe the density effects on the gamma-ray transport, 4.43 MeV gamma ray sources were modeled at depths of 0, 5, 10, 20, 30, and 50 cm in the soil volume and the 4.43 MeV gamma ray yield at the detectors was counted. Also, to observe the effect of density on the neutron and gamma transport simultaneously, the complete model with the NG 14 MeV point source was used and the 4.43 MeV gamma ray yield at the detectors was counted for same density variations.

8.1.1.2. Moisture Variations

Moisture content in soil directly affects the neutron transport due to increased elastic interactions with hydrogen nuclei. On average, neutrons lose half their energy in elastic collisions with hydrogen nuclei, and can lose all of their energy. However, the neutron generator produces fast neutrons (~14 MeV), that could theoretically undergo almost two collisions with hydrogen and remain above the threshold energy (~4.5 MeV) necessary for INS reactions with carbon. The soil bulk density increases with an increase in the soil moisture content. Assuming that a given soil volume remains constant with the increase of moisture content, *i.e*. pore space allowing, and no swelling occurs, the increase in the bulk density of a given soil volume is dictated by Equation 8.2.

$$\rho_{bw} = \frac{\rho_b}{1 - X} \tag{8.2}$$

Where ρ_b is the old bulk density previous to the addition of moisture, ρ_{bw} is the new bulk density with added moisture, and X is the weight fraction of moisture added.

Equation 8.2 was validated with an experiment. Water was added to a graduated cylinder filled with a volume of dry sand and the weight percent of water, or moisture content, and bulk density was calculated until saturation of the sand was observed. The moisture content in the sand is plotted versus the measured and analytical increase in bulk density (Fig 8.2). The moisture content of the modeled soil was varied from 0 to 100% water by weight while maintaining the carbon concentration constant with exception of the 100% water case. The effects of moisture on the neutron and gamma-ray transport were determined utilizing similar methods as for density variations.

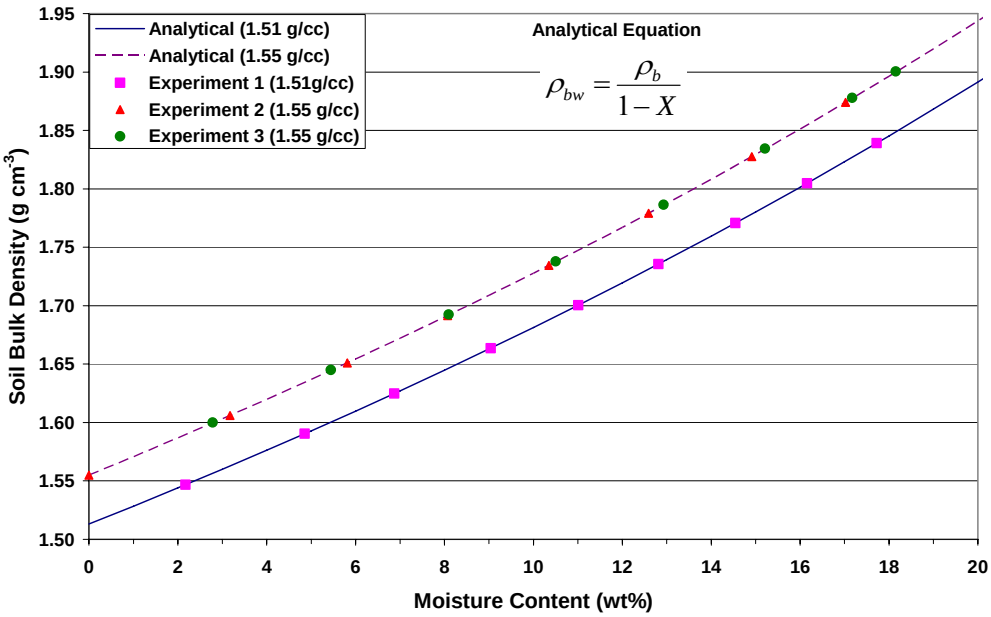

Figure 8.2. Effect of Moisture Content on Soil Bulk Density, experiment (points) and analytical (lines), bulk density versus moisture content (w/o).

8.1.1.3. Soil Layers

An increasing (cumulative) thickness of a soil layer with a carbon content of 2% by weight was modeled, *i.e.* for the 10 cm case; there is a 10 cm thick layer of soil with carbon from 0-10 cm and soil without carbon from 10-60 cm. Also, an increasing depth (differential) of a 5 cm thick layer of soil with a 2% by weight carbon content was modeled, *i.e.* for the 10 cm case; there is a 5 cm thick layer of soil with carbon from 5-10 cm and without carbon from 0-5 cm and from 10-60 cm. The layer calculations were repeated for soil bulk densities of 0.5, 0.75, 1, 1.5, and 2 g cm^{-3}. The carbon ROI yields are compared.

8.1.1.4. Volume and Depth

Version β of the model was utilized to calculate the effects of bulk density variations on the volume and depth that the system may sample. The volumes

contributing to 90% of the total carbon inelastic gamma ray flux intercepting the detectors, and the maximum depth associated with these volumes are calculated. These 90% volumes and depths are utilized for a relative comparison of the bulk density effects. The volumes contributing to 90% of the total carbon inelastic gamma ray flux intercepting the detectors, and the maximum depth associated with these volumes is calculated. The method described in chapter 6 is utilized to calculate these volumes and depths.

8.1.2. RESULTS AND DISCUSSION

The results of the density effects on neutron and gamma-ray transport individually, and combined are given in Figures 8.3, 8.4, and 8.5, respectively. There is a difference of a factor of two between the fast neutron fluxes at 30 cm for 0.25 and 1.5 g cm^{-3}. The difference in fluxes in the average bulk density range is only 25%. The bulk density of the soil has an observable effect on the neutron transport. There is a difference of a factor of five between the fast neutron fluxes at 30 cm for 0.25 and 1.5 g cm^{-3}. The difference in fluxes in the average bulk density range is reduced to a factor of two. The gamma-ray transport appears to be more affected than neutrons by the bulk density. Neutron attenuation is dominated by lighter elements, and gamma-ray transport is the opposite, therefore, when increasing the soil density, which is composed of heavier elements, then the affect on the gamma-ray transport is more evident.

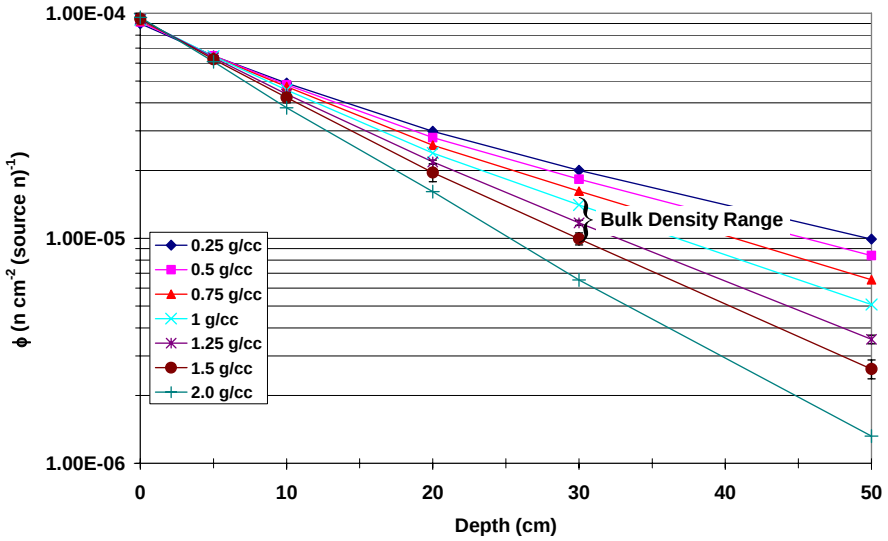

Figure 8.3. An isotropic 14 MeV neutron point source was modeled to emit into a 250 cm by 200 cm by 60 cm soil volume with a carbon content of 2% by weight. The fast neutron flux, 5-14 MeV, in the soil is plotted for different bulk densities.

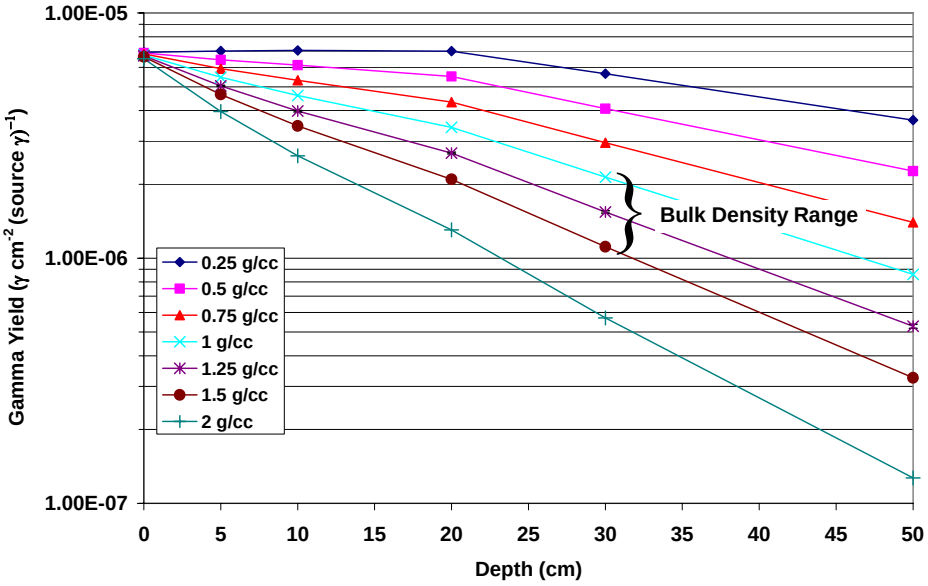

Figure 8.4. An isotropic 4.43 MeV gamma point source was modeled to emit from different depths of a 250 cm by 200 cm by 60 cm soil volume with a carbon content of 2% by weight. The carbon region of interest gamma yield, 4.43 MeV, at the detectors is plotted for different bulk densities.

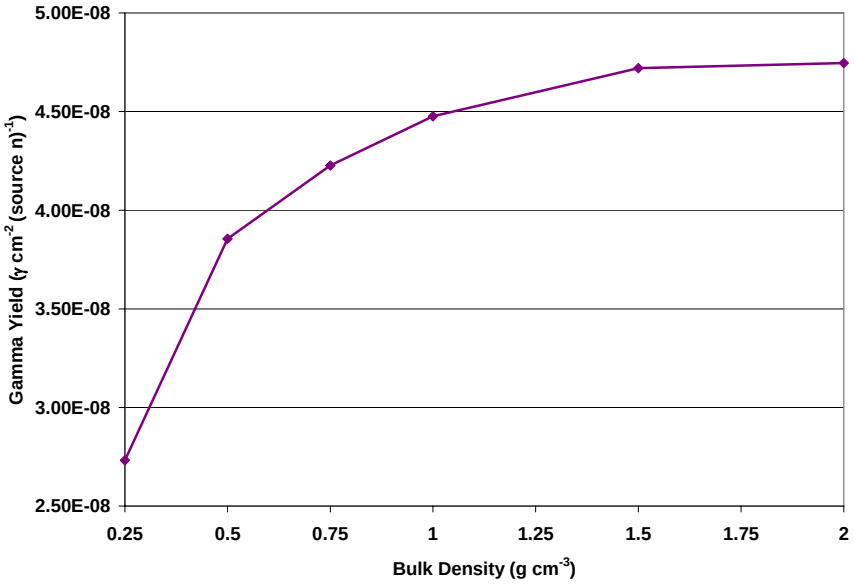

Figure 8.5. Version β of the model was utilized. The carbon region of interest gamma yield, 4.43 MeV, at the detectors is plotted versus bulk densities.

From Figure 8.5, it can be observed that as the bulk density of a homogeneous soil with constant carbon concentration increases the mass of carbon in a given soil volume increases and therefore the carbon gamma ray yield increase proportionally. It is important to note that porosity has not been modeled here, and that the transport may be less affected with porosity included due to the increased void space in the soil volume.

The results of the moisture content effects on the gamma-ray transport are given in Figure 8.6 and the neutron transport results are given in Figures 8.7, 8.8, and 8.8. Also, the effect on the complete model is given in Figure 8.10. The results indicate that the fast neutron and gamma-ray transport are not heavily affected directly by the addition of moisture, but instead, are indirectly affected by the increase in bulk density due to the increase in moisture content. In Figure 8.6, this is observed in the comparison of the 0%

and 50% moisture lines both with the same density of 1.4 g cm^{-3}. The direct affect on the fast neutron transport by the addition of hydrogen can be seen as well by the comparison of the former discussed lines, the addition of 50% moisture, when maintaining constant bulk density, reduces the fast neutron flux at 30 cm by only 20%. Whereas, the fast neutron flux at 30 cm reduces by nearly 70% with the addition of 50% moisture and changing the bulk density according to Eq. 8.2. Comparing Figures 8.8 and 8.9, it is clear that moisture dominantly affects the thermal neutron flux which is inconsequential to the measurement of carbon because the carbon reaction of interest is only occurs with the fast neutron flux. The same trends can be dually observed in Figure 8.6 for the gamma ray transport. The line of 100% water indicates the least amount of gamma-ray attenuation, whereas, 50% moisture and with the bulk density increased, indicates the greatest attenuation. Also, the line of 0% moisture with a density of 1.5 g cm^{-3}, and 10% with a similar density of 1.56 g cm^{-3}, are almost the same. Moisture content in soil appears to affect the fast neutron and gamma-ray transport due to the increase in bulk density.

It can be observed from Figure 8.10 that bulk density increases as soil moisture content increases (Eq. 8.2); however, the mass of carbon in a given soil volume remains constant. As shown above, density affects both neutron and gamma flux and therefore as moisture is increased in a homogeneous soil the carbon gamma ray yield decreases proportionally.

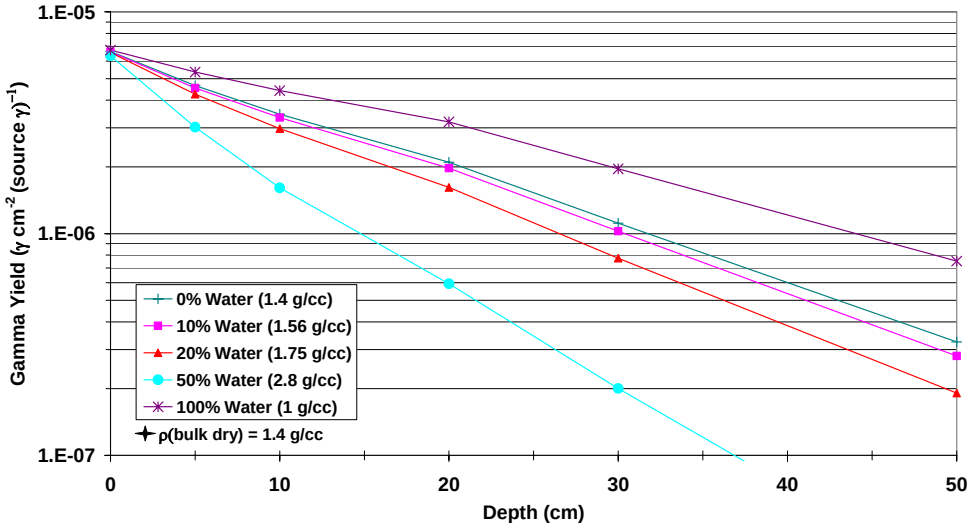

Figure 8.6. An isotropic 4.43 MeV gamma point source was modeled to emit from different depths. The carbon region of interest gamma yield, 4.43 MeV, at the detectors is plotted for moisture content variations.

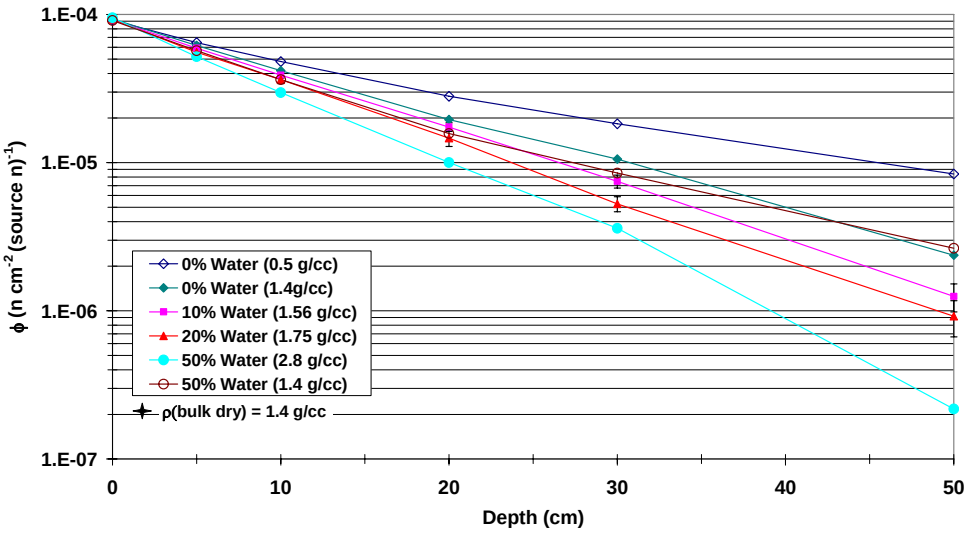

Figure 8.7. An isotropic 14 MeV neutron point source was modeled to emit into the soil volume. The fast neutron flux, 5-14 MeV, in the soil is plotted for moisture content variations.

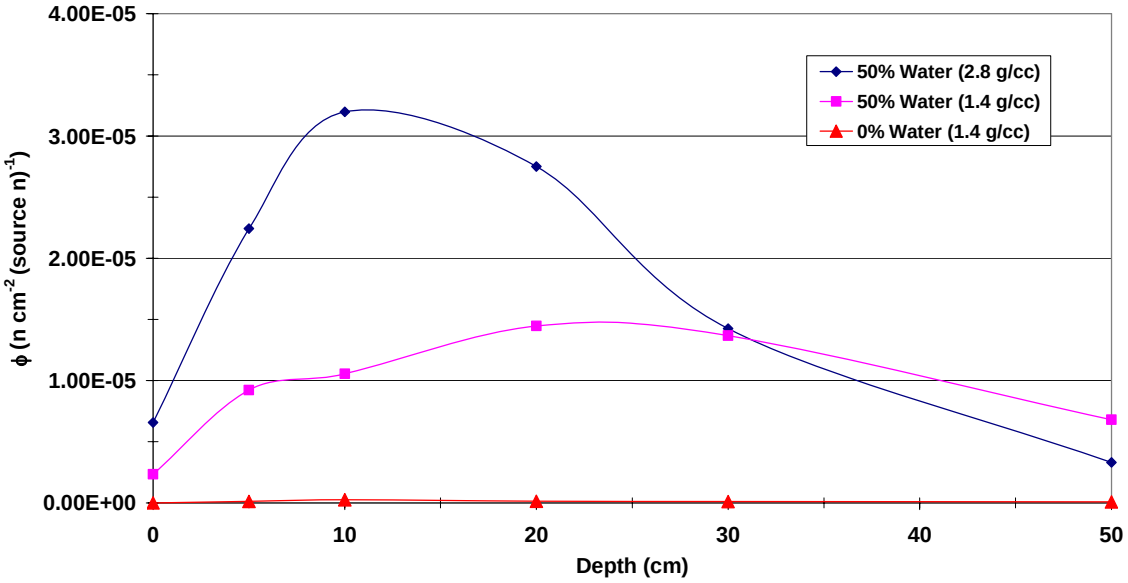

Figure 8.8. Moisture effects on 0-0.5 eV (thermal) neutron flux in soil versus depth.

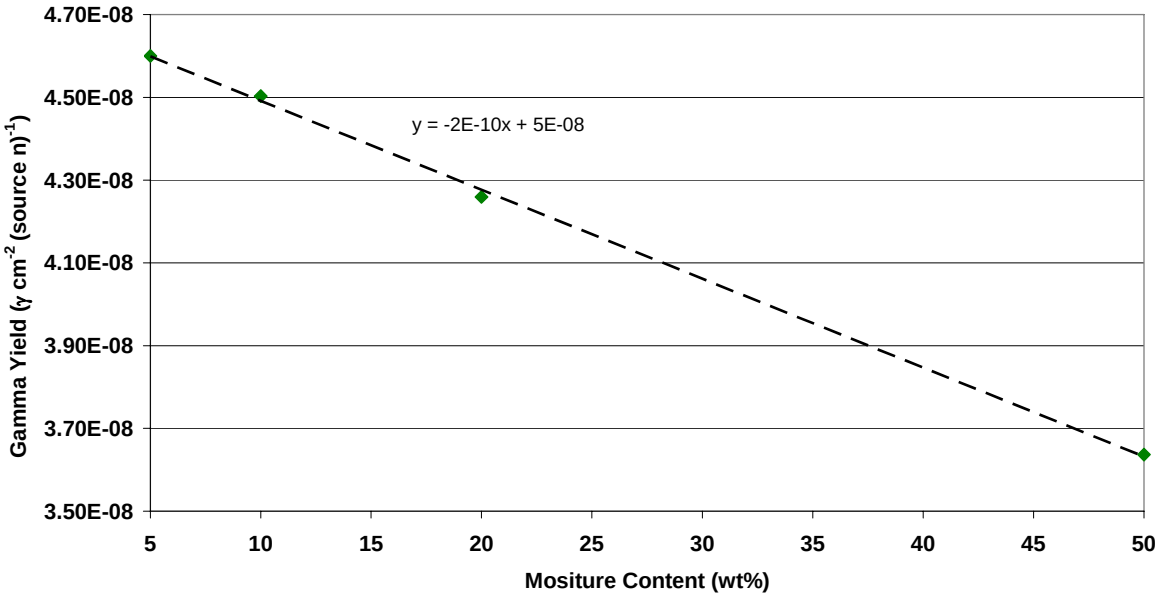

Figure 8.9. Moisture effects on 5-14 MeV (fast) neutron flux in soil versus depth.

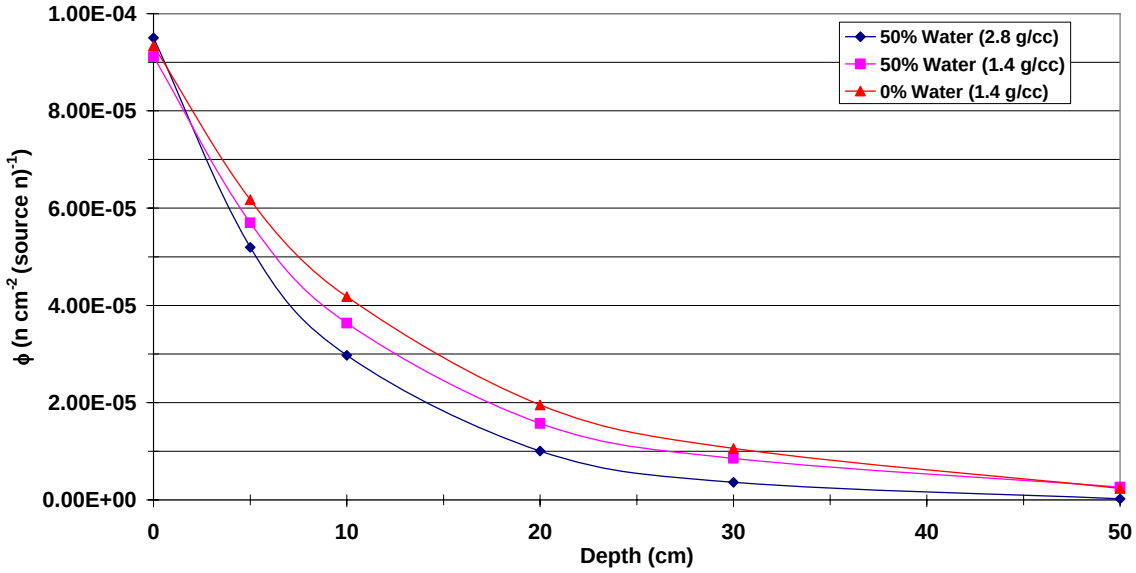

Figure 8.10. Version α of the model was utilized The carbon region of interest gamma yield, 4.43 MeV, at the detectors is plotted versus moisture content.

The results from the increasing thickness soil layer calculations are given in Figure 8.11. The combined results from the increasing thickness and depth soil layers for a bulk density of 1.5 g cm^{-3} are given in Figure 8.12. The yields in Figure 8.11 are normalized to the yield from a 5 cm thick layer with a bulk density of 2 g cm^{-3}. The carbon yield reaches a plateau from shallower depths for increasing ρ_b. The detection depth of the system decreases with increased ρ_b (Fig. 8.11). As the bulk density of the soil increases so does the number density of isotopes. The result is a stronger signal from more shallow depths and therefore less sensitivity to increasing depths. The carbon yield reaches a plateau at the same depth of 25 cm from both the increasing thickness and depth of carbon layers. The signal from the increasing depth of carbon layers decreases to background level at a depth of 25 cm. The detection depth of the system for a given ρ_b and carbon content is independent of where the carbon is present in the soil (Fig. 8.12).

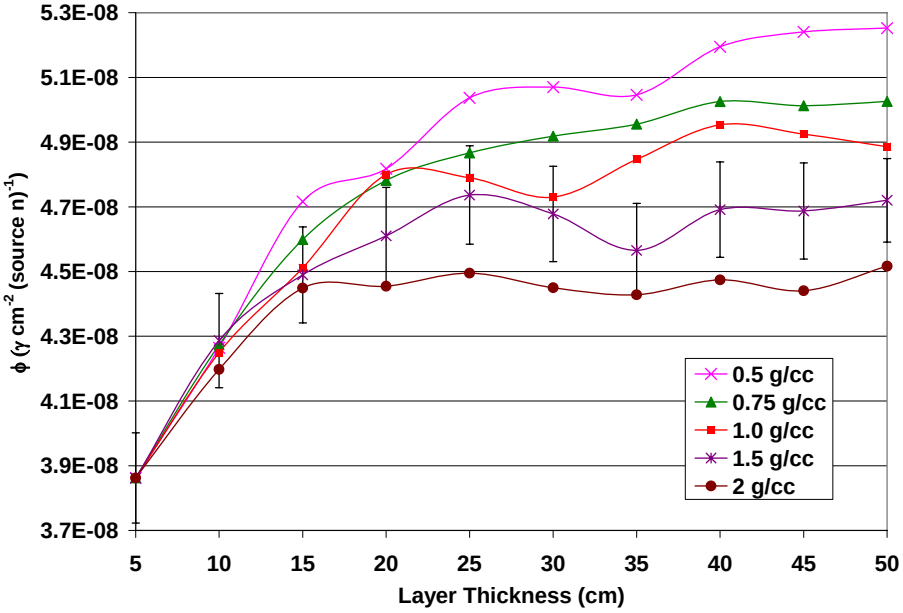

Figure 8.11.Carbon (4.43 MeV) gamma ray yield at the detectors from increased depth of carbon layers of varying density.

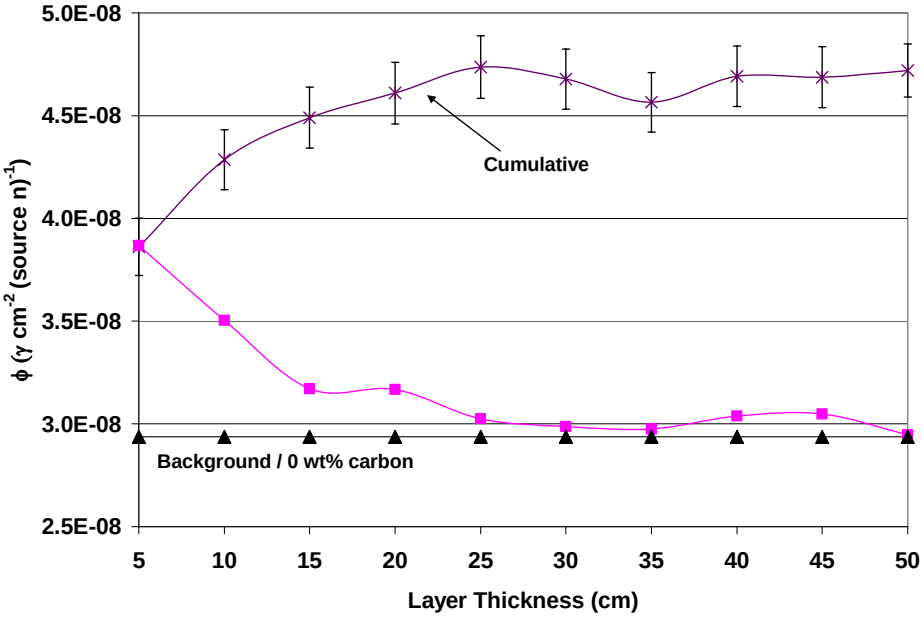

Figure 8.12. Carbon (4.43 MeV) gamma ray yield at the detectors from increased depth and differential of carbon layers with ρ_b of 1.5 g cm^{-3}.

The affects of bulk density on the volumes contributing to 90% of the total carbon inelastic gamma-ray flux intercepting the detectors and their associated depths are given in Figures 8.13 and 8.14, respectively. The 90% volumes are reduced by a factor of four from 0.65 to 0.16 m^3 from a bulk density of 0.25 to 2 g cm^{-3}. The reduction in the 90% volumes can be attributed to increased number density of the elements in the soil, as a larger fraction of the gamma-ray yield will come from a more shallow depth, therefore the 90% volumes be smaller. Though, the volumes are reduced by a factor of four from low to high density, the associated depths are only reduced by just more than a factor of two, from 49 to 21 cm. In the average bulk density range the 90% volume is reduced 45% and the depths are only reduced 26%, from 33 to 26 cm. The average sampling depth for this bulk density range is ~30 cm. These results help us understand the sensitivity of the system to detect carbon from various soil depths. As the soil bulk density increases, the depth sensitivity of the system to detect carbon is reduced. However, it is important to note two things, that the changes are not large in the average bulk density range the 90% volumes and depths, and that even with a bulk density well passed that to solidified earths, the system still measures a 90% signal at 21 cm.

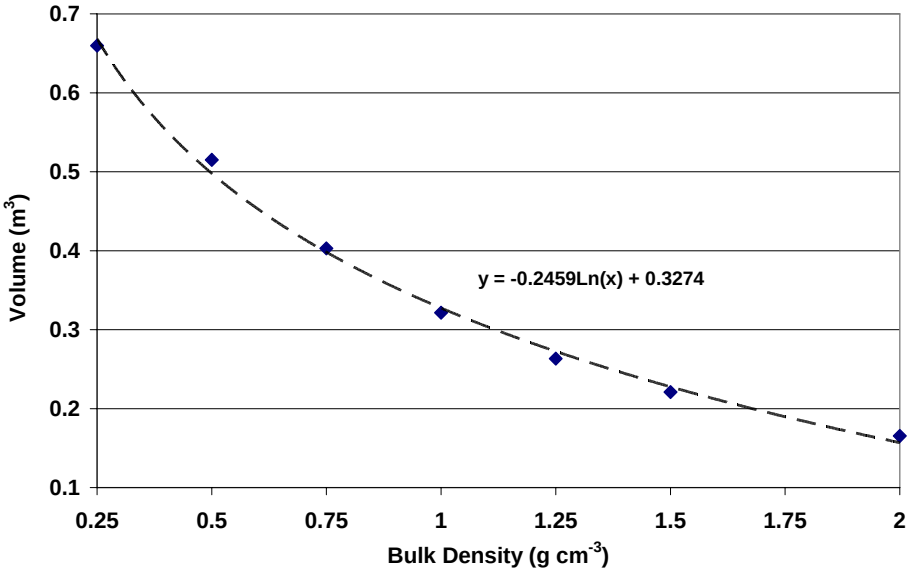

Figure 8.13. The volumes contributing to 90% of the total carbon inelastic gamma ray flux intercepting the detectors are plotted versus bulk density variations.

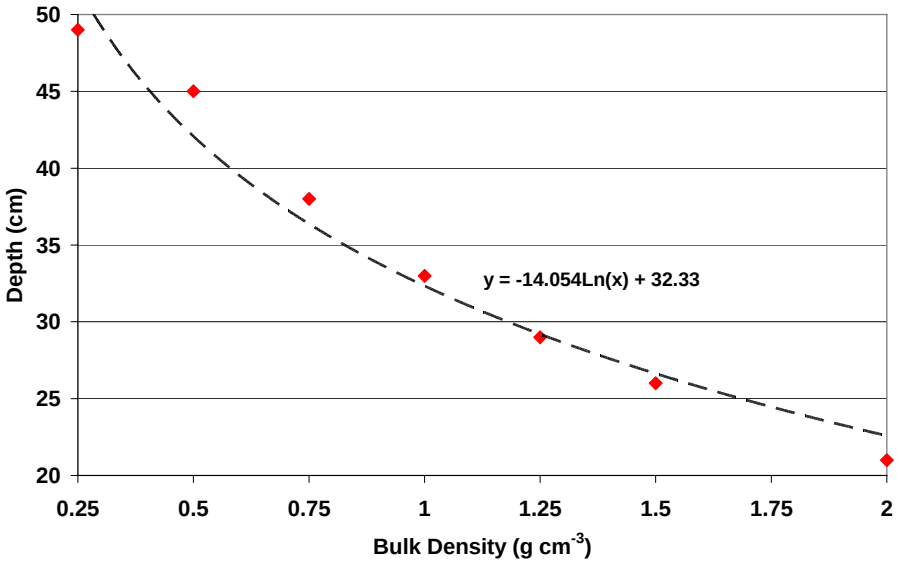

Figure 8.14. The maximum depth associated with the volumes contributing to 90% of the total carbon inelastic gamma ray flux intercepting the detectors are plotted versus bulk density variations.

8.2. CARBON PROFILE

Presented here is a comparison of the carbon gamma flux from soil with a carbon profile and a homogeneous soil with 5% by weight carbon (5 w/o C). Version α of the model was utilized with the soil carbon profile adjusted for the calculations (Fig. 8.17). The profile of carbon in the soil is dictated by Equation 8.3. Equation 8.3 was fitted using nonlinear least-squares to carbon profiles obtained in experiments at BNL (Fig.8.15) nine spots measured in a Duke Forest site (Fig. 8.16). In each case, the thick solid line in the graphs represents a carbon transport model given by Equation 8.3. Integrating Equation 8.3 from a depth A to a depth B, where A is usually zero at the surface and B is 30 cm belowground, yields the surface carbon density in units of g C cm^{-2}, representing the projection of belowground carbon onto surface unit area. The results of the integration from A to B, together with the measured values for BNL and Duke Forest, are summarized in Table 8.1; in both sites there is ~5% difference between the integrated and mean measured values. The equation is dominated by γ in the exponential. The behavior of the equation while varying γ is shown in Figure 8.18. The carbon concentration at Z equals 0 is the sum of β and α, and as Z goes to infinity the concentration converges to α. The carbon concentration divided by the bulk density of the soil equals the weight percent of carbon in that specific soil. The values of β and α for Figure 8.18 represent a soil with 10 w/o C at the surface and 2 w/o C as Z goes to infinity with a soil density of 1.4 g cm^{-3}.

$$C_c = \alpha + \beta e^{-\gamma z} \tag{8.3}$$

C_c = carbon concentration (gC cm^{-3})
α = constant (gC cm^{-3})
β = constant (gC cm^{-3})
γ= constant (cm^{-1})
z = soil depth (cm)

There is one detector volume of the size 12.7cm by 38.1 cm by 15.24 cm in height. The detectors are at a 45 degree angle with the horizontal. The shielding present is compressed boric acid plates on the bottom of the detector, Cerrobend in front of the detector, a volume of borated water in front and on the sides of the generator and plates of aluminum in front of the neutron generator.

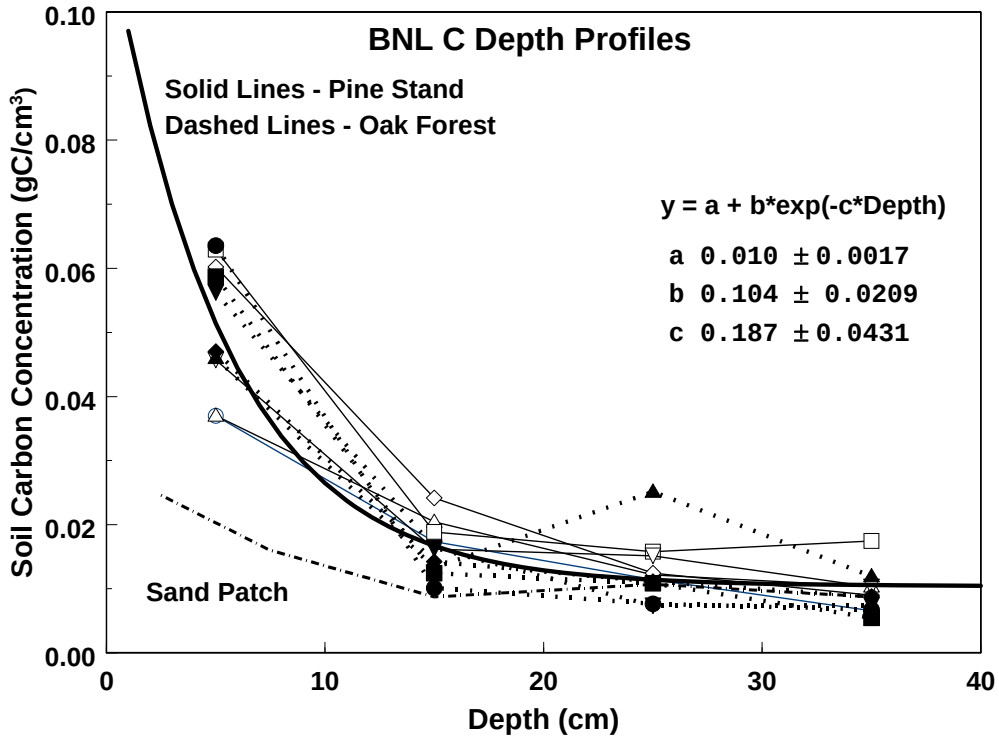

Figure 8.15. Individual BNL carbon depth profiles in the pine stand and oak forest. The former is shown as a single separate line. The thick line is the non-linear fit to all data points. Here α, β, and γ are represented by a, b, and c, respectively.

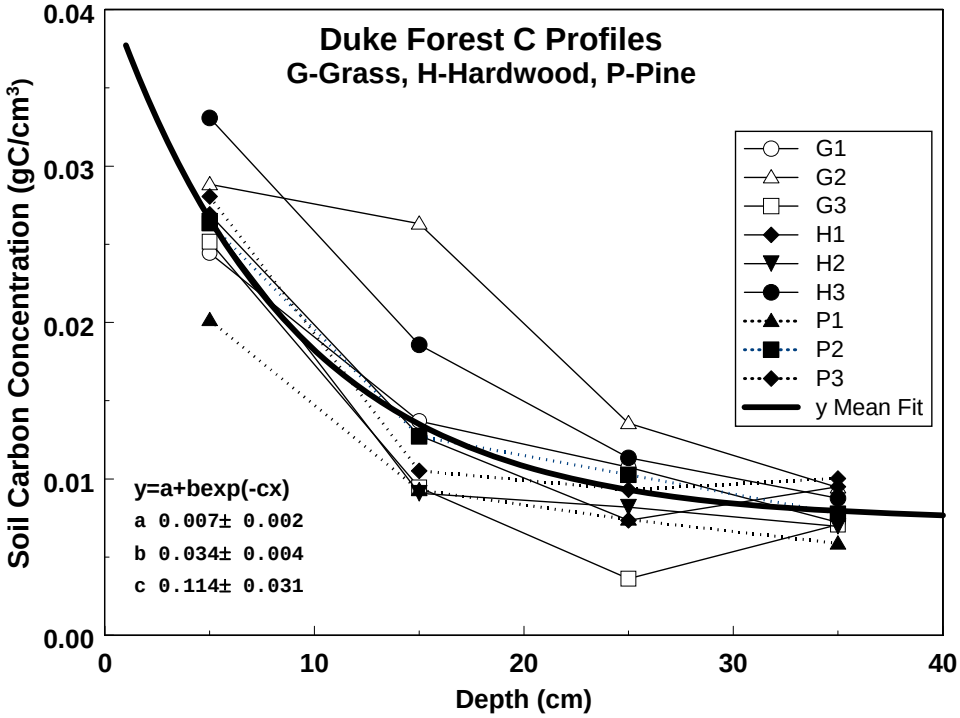

Figure 8.16. Carbon depth profiles derived from Duke Forest excavations. The thick line represents the non-linear fit to all data points. Here α, β, and γ are represented by a, b, and c, respectively.

Table 8.1. Depth profile coefficients.

Site	a (STE) (g C/cm^3)	b (STE) (g C/cm^3)	c (STE) (1/cm^1)	Integral (0-30 cm) (g C/cm^2)	Measured (g C/cm^2)
BNL	**0.010 (0.002)**	**0.104 (0.021)**	**0.187 (0.043)**	**0.854**	**0.807**
Duke	**0.007 (0.002)**	**0.034 (0.004)**	**0.114 (0.031)**	**0.498**	**0.473**

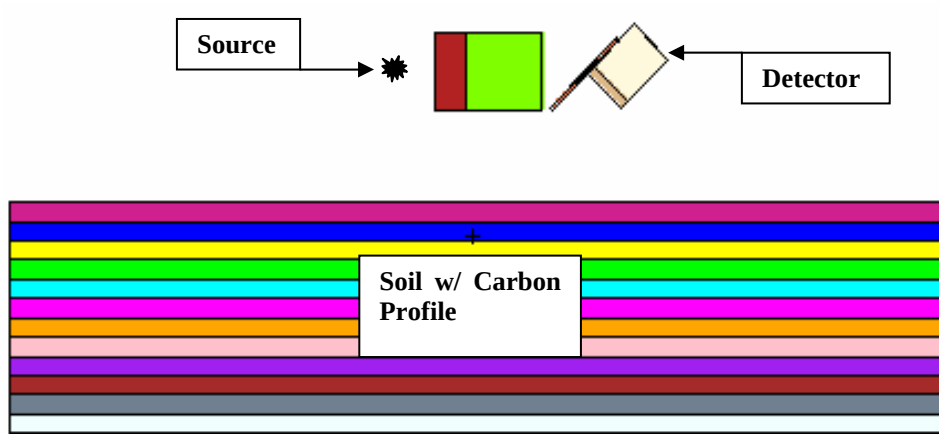

Figure 8.17. Diagram of the soil carbon layers modeled in MCNP5 for the simulation

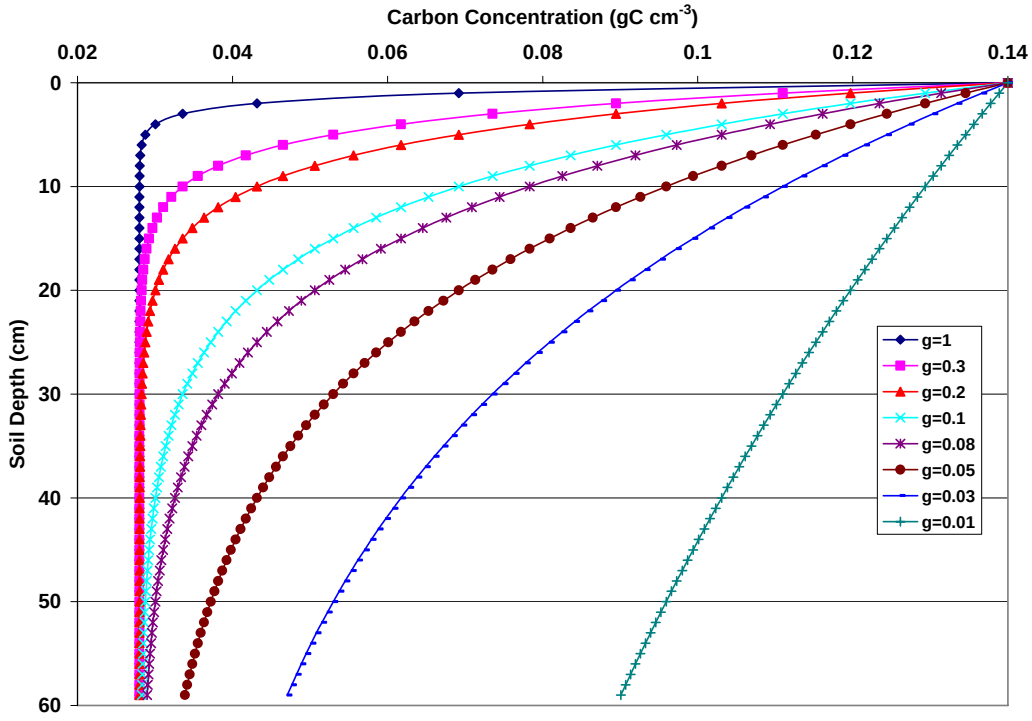

Figure 8.18. Equation 8.3 with β=0.112 g cm^{-3}, α=0.028 g cm^{-3} and γ varied. The values of β and α were chosen to represent a soil with 10 w/o C on the surface reducing to 2 w/o C with increased depth.

8.2.1. Experimental

The mass of carbon in the modeled soil volume is maintained constant to isolate the effect of the carbon profile on the carbon region of interest (ROI), independent of the mass of carbon in soil. The weight percents of the other elements in the soil are adjusted accordingly to maintain their relative abundance to each other. A detailed explanation of the weight percent adjustments of all the elements is given in Appendix G. The mass of carbon is maintained constant by varying β and γ in equation 8.3 with α constant. To solve for the values of β and γ for different carbon profiles the evaluated integral of Eq. 8.3 is set equal to an area concentration of carbon (g C cm^{-2}) in the modeled soil volume. The area concentration used for this example is calculated for the modeled soil with 5 w/o carbon and a bulk density of 1.4 g cm^{-3} (Eq. 8.4). The derivation of the evaluated integral of equation 8.3 is given below. The dependence of β and γ is plotted in Figure 8.19. The plot of equation 8.3 with β and γ varied to maintain a constant area concentration of 4.2 gC cm^{-2} equating to 210 kg C is given in Figure 8.20.

$$\frac{5\%C}{100} * 1.4 g cm^{-3} * 60 cm = 4.2 gC cm^{-2} \tag{8.4}$$

$$\int_0^D \alpha + \beta e^{-\gamma z} = C(g \cdot cm^{-2})$$

$$\alpha * z - \frac{\beta e^{-\gamma z}}{\gamma} = C$$

$$\left[\alpha D - \frac{\beta e^{-\gamma D}}{\gamma}\right] - \left[\alpha * 0 - \frac{\beta e^{-\gamma * 0}}{\gamma}\right] = C$$

$$\left[\alpha D - \frac{\beta e^{-\gamma D}}{\gamma}\right] + \frac{\beta}{\gamma} = C \tag{8.5}$$

$$\alpha D + \frac{\beta}{\gamma}\left(1 - e^{-\gamma D}\right) = C$$

$$\frac{\beta}{\gamma} = \frac{C - \alpha D}{1 - e^{-\gamma D}}$$

$$\beta = \frac{(C - \alpha D) * \gamma}{1 - e^{-\gamma D}} \tag{8.6}$$

$$with \;\; C = 4.2 gC \cdot cm^{-2}, \alpha = 0.028 g \cdot cm^{-3}, D = 60 cm$$

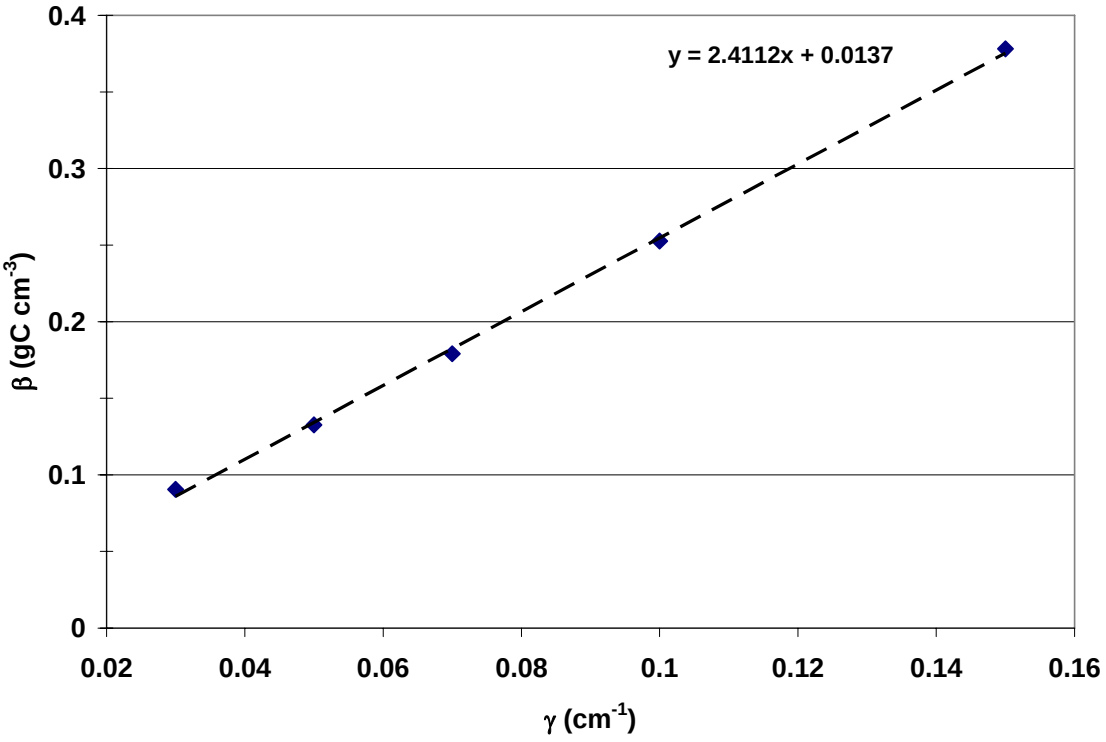

Figure 8.19. The graph of β versus γ from Equation 8.6.

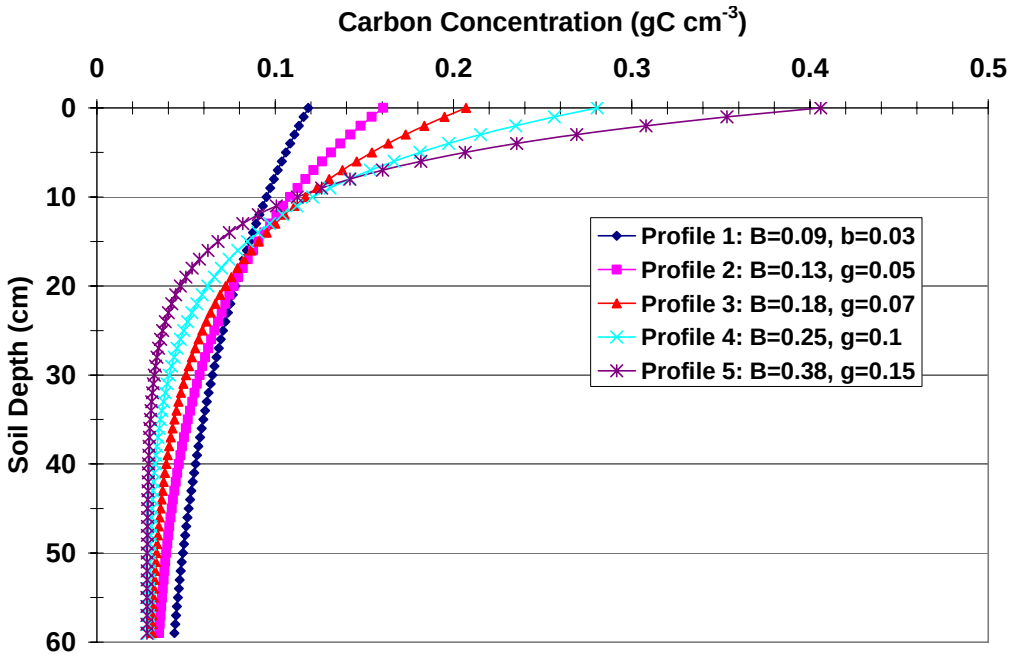

Figure 8.20. Carbon concentration profiles from Equation 8.3 varying β and γ to maintain a constant area concentration of carbon of 4.2 gC cm^{-2} equating to 210 kg C in the soil volume.

Profiles 1 thru 5 are used to model different profiles in MCNP. The profiles are modeled as layers of decreasing C_c. For the purposes of efficiency, layers with a thickness of 5 cm are used for the model. To calculate the C_c in over every 5 cm the integral of Eq. 8.3 is evaluated for every 5 cm layer, *i.e.* from 10-15cm, and is then divided by the thickness of the layer, 5cm. The derivation of the Cc calculation for the 5 cm layers is given below. The total amount of carbon in the soil volume utilizing Eq. 8.7 is maintained at 210 kg C. The tabulated values used for profile 5 for the model are given in Table 8.2. The carbon gamma flux intercepting the detector volume is calculated in MCNP and the results from the carbon profiles and homogeneous cases are given in Table 8.3. The percent of the total carbon present in the first 5 and 10cm is given in Table 8.4. In Figure 8.21, the results from Table 8.3 are plotted versus the

percentages from Table 8.4. The estimated soil volume contributing to 90% of total carbon signal and its associated maximum depth for the homogeneous case and profiles 1, 3 and 5 are presented in Table 8.5 and plotted in Figure 8.22.

$$\int_{Z1}^{Z2} \alpha + \beta e^{-\gamma z} = Cc(g \cdot cm^{-3}) * 5cm \quad \textbf{(8.7)}$$

$$\frac{\int_{Z1}^{Z2} \alpha + \beta e^{-\gamma z}}{5cm} = Cc(g \cdot cm^{-3}) \quad \textbf{(8.8)}$$

$$with\ Cc = average\ \ carbon\ concentration\ over\ layer$$

$$Z2, Z1 = upper / lower\ bound\ of\ \ soil\ layer$$

Table 8.2. Average values of carbon concentration from equation 8.8 for carbon profile 5. Used for input to MCNP.

Depth Range (cm)	Mean (gC cm^{-3})	w/o Carbon
0-5	0.2940	21.00
5-10	0.1536	10.97
10-15	0.0873	6.24
15-20	0.0560	4.00
20-25	0.0412	2.95
25-30	0.0343	2.45
30-35	0.0310	2.21
35-40	0.0294	2.10
40-45	0.0287	2.05
45-50	0.0283	2.02
50-55	0.0281	2.01
55-60	0.0281	2.00

Table 8.3. Gamma ray flux intercepting the detector volume for homogeneous soil and soil with the carbon profiles from Figure 3. The homogeneous case has 5 w/o carbon. The background in the carbon ROI with 0 w/o carbon in the soil is 1.73×10^{-8} n cm^{-2}(source n)$^{-1}$. * Errors less than 1%.

Energy (MeV)	Carbon Profile ϕ (γ cm^{-2} (source n)$^{-1}$) *					
	Homogeneous	1	2	3	4	5
4.43	3.46E-08	5.26E-08	6.10E-08	6.69E-08	7.67E-08	8.79E-08
Total	7.11E-06	7.09E-06	7.08E-06	7.08E-06	7.06E-06	7.01E-06

Table 8.4. Percentage of total carbon present in the first 5 and 10cm layers for the profiles utilized in the calculations.

Layer Thickness (cm)	Homo-geneous	Profile 1 (% of total carbon in layer)	Profile 2 (% of total carbon in layer)	Profile 3 (% of total carbon in layer)	Profile 4 (% of total carbon in layer)	Profile 5 (% of total carbon in layer)
5	8	13	17	22	27	36
10	17	25	32	38	45	54

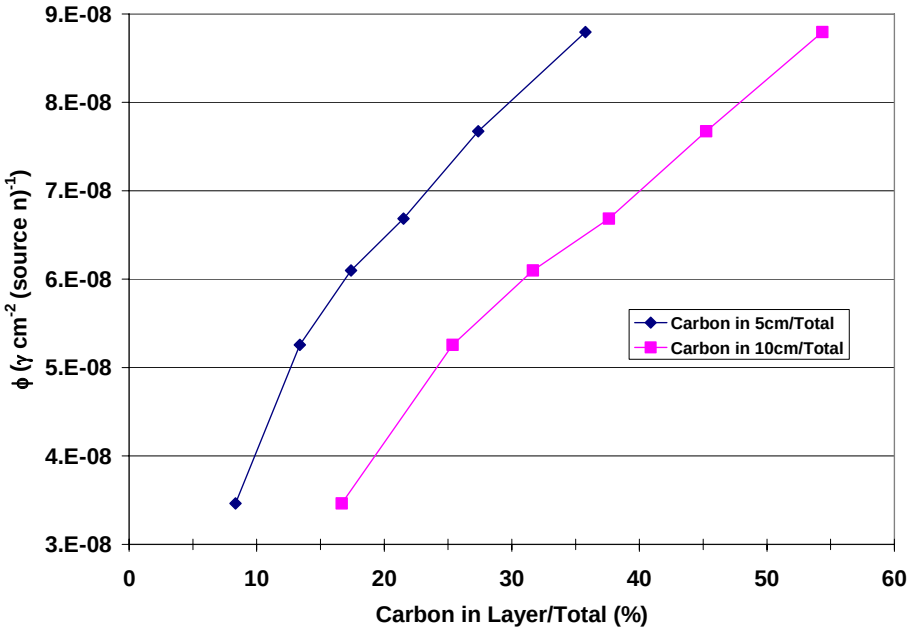

Figure 8.21. Carbon ROI gamma rays intercepting the detector volume plotted versus the percent of the total carbon present in the first 5 and 10cm of the modeled soil volume.

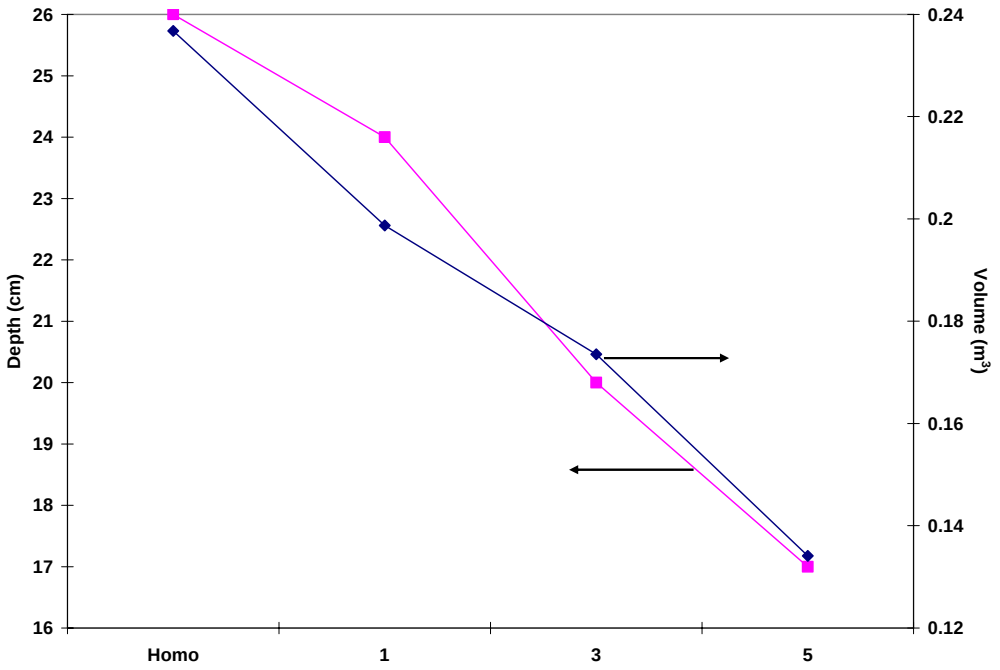

Figure 8.22. The estimated soil volumes contributing to 90% of the total carbon signal and their associated maximum depths from the homogeneous case carbon profiles 1, 3, and 5.

Table 8.5. The estimated soil volumes contributing to 90% of the total carbon signal and their associated maximum depths from the carbon profiles and homogeneous case.

Profile	Depth (cm)	Volume (m^3)
Homo	26	0.236766
1	24	0.198729
3	20	0.173542
5	17	0.134118

8.2.2. Discussion

The data presented above appears to indicate that the INS system is sensitive to carbon profiles. The relationship between β and γ from equation 8.6 (Fig. 8.17) is close

to linear but deviates from linearity with increased values of β and γ and therefore with increased percentage of carbon in the top layers of the soil volume. The results in Table 8.3 show a steady increase in carbon gamma rays intercepting the detector with an increased proportion of carbon in the soil being close to the surface. The total gamma rays from the soil are constant with varying profiles. Also, the homogeneous case with 5 w/o carbon has twice the intensity of the background (1.73×10^{-8} γ cm^{-2} (source particle)$^{-1}$) from the soil with 0 w/o carbon. The results in Table 8.5 and Figure 8.22 indicate that the carbon profiles modeled here have a significant impact on the size of the soil volume from which 90% of the total carbon signal is being measured and the maximum depth of that volume. The volume and depth from homogeneous to profile 5 decrease approximately 50% and 35%, respectively. An important note is that the profiles utilized here for modeling are of extreme cases. On average the carbon profile in soil will not be as dramatic as even profile 1 for instance, most certainly not profile 5. The profiles that will be analyzed will have a more subtle carbon profile, *i.e*. 4 w/o C at the surface and 1 to 2 w/o C at 30 cm in the soil.

8.3. STONES

The presence of large stones in soil may affect the carbon signal the INS system measures because they displace the carbon that the system would measure. In soil analysis with coring or excavating stones are not an issue simply because cannot core or dig where a large stone is present. The INS system, being non-invasive, must recognize the presence of stones by their effect on the carbon signal. Presented here is a comparison of the carbon gamma flux from soil with a homogeneous soil with 2 w/o C (App. A) and with varying sizes of stones present in the soil. Version α of the model was utilized and the stones are hemi-spherical in shape extending down into the soil volume (Fig 8.21). The radii of the stones increase from 0 cm to 50 cm. The centerline location

of the response volumes (Fig. 5.9) is at the approximate midpoint between the detectors and the NG, indicating that the dominate soil response is center around point. Therefore, all of the stones are centered on this midpoint. An hour runtime is simulated by taking the product of the gamma flux from MCNP5 and the number of neutrons produced by the NG in an hour based on the output calculated in the copper foil experiment (Table 7.2).

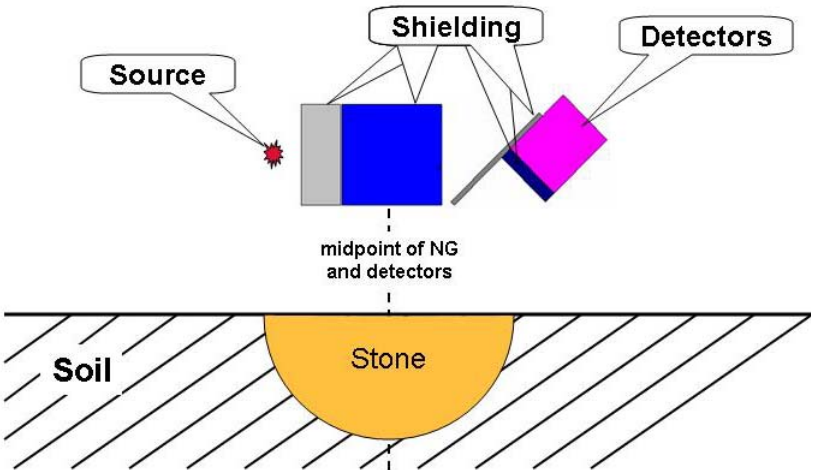

Figure 8.23. Locations of the stones and the response volume's midpoint relative to the model geometry.

The net gamma flux intercepting the detector volume in the carbon ROI is plotted versus the stone radii (Fig. 8.24). The effect of the stones on the carbon signal is non-linear. The non-linearity is due to the nature of the carbon signal and the stones being modeled as hemi-spheres. The carbon displaced closer to the surface has a stronger effect on the carbon signal. The gamma flux is reduced 28% from no stone to a stone with a radius of 30 cm. A 2nd order polynomial is fit to the data with an R^2 of 0.99. The approximate size of a stone present in a sampling location could theoretically be calculated based on the fitted polynomial.

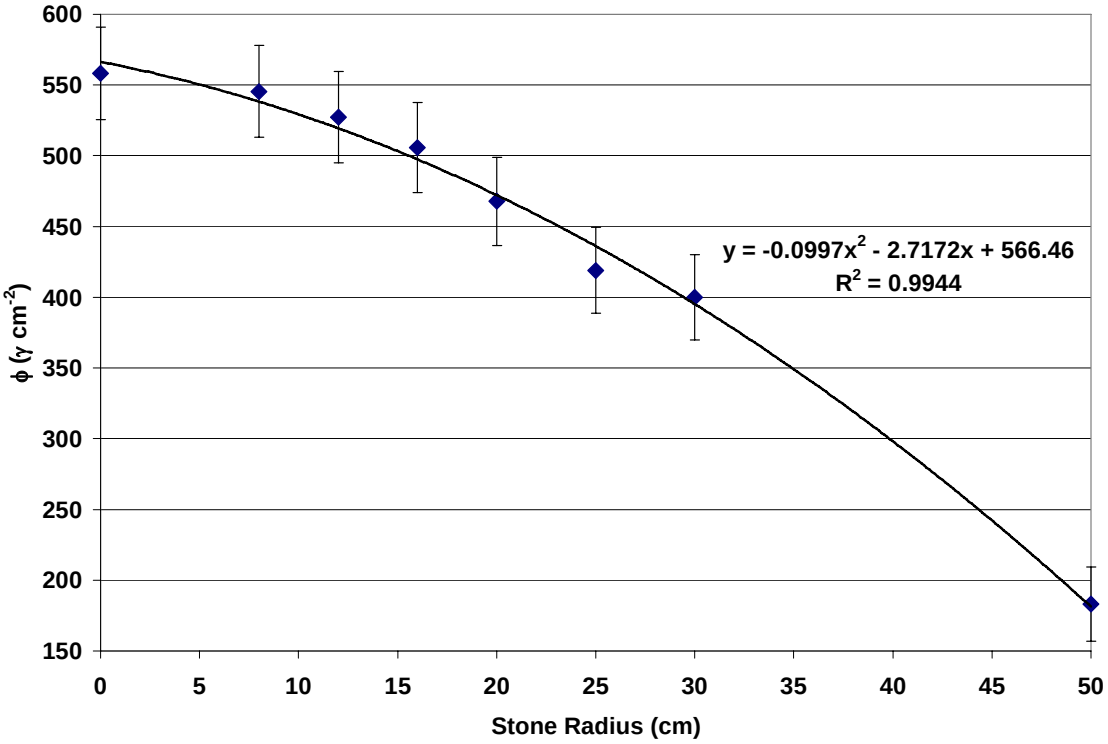

Figure 8.24. The net gamma flux intercepting the detector in the carbon ROI versus the stone radii.

8.4. CONCLUSION

Soil bulk density affects the neutron and gamma transport through soil thus affecting the gamma yield at the detectors. However in the average bulk density range the effect is minimal. INS, being a threshold process, the presence of moisture alone does not have a dramatic effect on carbon measurements. Moisture content affects the neutron and gamma transport through the increase of bulk density, rather than the increased presence of the hydrogen introduced into the soil volume. As bulk density increases, the mass of carbon in a given soil volume increases and therefore the carbon gamma ray yield increases proportionally. However, as moisture content increases, the

mass of carbon in a given soil volume remains constant and therefore the carbon gamma ray yield decreases proportionally.

The carbon yield reaches a plateau from shallower depths for increasing ρ_b. The detection depth of the system decreases with increased ρ_b. The maximum depth associated with the volumes contributing to 90% of the total carbon inelastic gamma ray flux intercepting the detectors for a ρ_b of 1.5 g cm^{-3} is similar to the independent calculation of the detection depth of system from the soil layers. The depths are both around 25 cm.

Carbon profiles have a strong effect on the carbon signal and will have to be accounted for in future measurements. Stones reduce the carbon signal by displacing the soil in the volume measured by the INS system. The effect of stones on the carbon signal is predictable and relatively easy to account for.

Chapter 9: INS Calibration

The largest scientific hurtle still present for the INS system is calibration. Calibration of the system is necessary for relating the carbon gamma ray counts from the detectors to a carbon concentration in the soil volume measured. So far, the method of calibration has been with field experiments on dry, homogeneous soils with known carbon contents as shown in Figure 7.4. This method of calibration works well for a laboratory setting, however, as shown in the perturbation examples in Chapter 8, moisture, density and carbon profile have a relatively strong effect on the system's carbon signal. Therefore, two different net peak areas in the carbon ROI will be measured for the same carbon content with varying soil parameters. Utilizing the benchmarked MCNP5 model of the INS system it is possible to create many calibration curves. The advantages of the model are that the calculations require a relatively short amount of time, and that all the soil variables are defined by the user. Two examples of the calibration curves created with the model are shown below: a moisture-porosity-density dependent calibration curve (Fig. 9.1) and a carbon profile dependent curve (Fig 9.2). Version β of the model was utilized for all the calculations in this chapter.

9.1. MOISTURE-POROSITY-DENSITY

Figure 9.1 is a calibration for the modeled soil volume with the general soil composition from Appendix A, where dry ρ_b is 1.4 g cm^{-3} and the dry volumetric soil porosity is 48% (Eq. 9.1). The moisture content of the soil is varied from 0 w/o to 25 w/o H_2O. The porosity of the dry soil volume is 48% and is reduced to 0% when the soil is fully saturated with water at 25 w/o H_2O. The dry ρ_b of the soil is 1.4 g cm^{-3} and increases to 1.86 g cm^{-3} at saturation, according to Equation 8.2. The carbon concentration is varied from 0 g C cm^{-3} to 0.14 g C cm^{-3} for each moisture level. The

counts from MCNP5 are normalized to a 60 min run of the NG utilizing the NG output calculated in the copper foil experiment (Chapter 7). The integral counts in the carbon ROI (Table 2.1) are plotted for each moisture level versus the increasing carbon concentrations.

$$P = \frac{S - S_R}{S} x100(\%) \tag{9.1}$$

Where P is the volumetric soil porosity (%) [Tölgyessy, 1993]

S is the specific mass of unit volume of solid components of soil (g)

S_R is the reduced (dry) bulk weight of 1 cm^3 of soil (g)

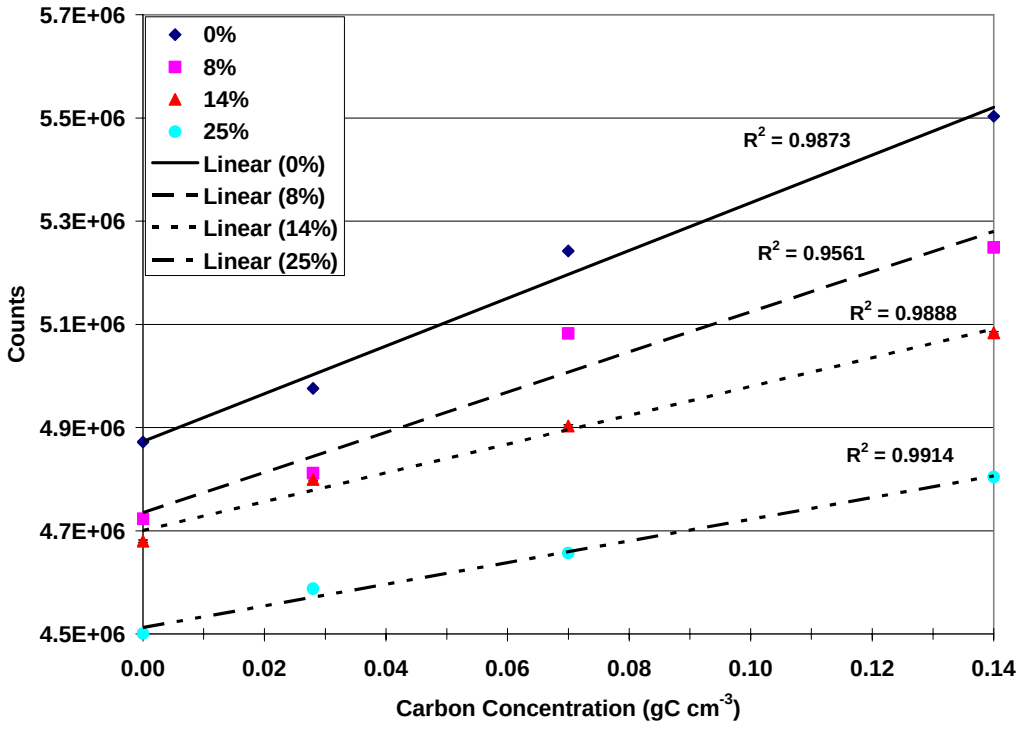

Figure 9.1. Integral counts in the carbon ROI as calculated with MCNP5 for a soil volume with varying levels of moisture.

Linear least squares regression is used for line fitting. It may be observed in Figure 9.1 that for the same carbon concentration there are four different values for the counts for the four different moisture levels. To find the dry carbon concentration it will be necessary to have some knowledge of the moisture level of the soil measured by the INS system. Moisture may be measured quickly and accurately with many readily available moisture gauges. Moisture content may also potentially be determined from the hydrogen signal in the TNC spectrum. A set of calibration curves similar to Figure 9.1 may be calculated utilizing the MCNP5 model. The dry carbon concentration may then be extrapolated with the knowledge of the moisture content of the soil at the time of the INS measurement.

9.2. CARBON PROFILE CALIBRATION

Figure 9.2 is a calibration for carbon profiles utilizing version β of the model. The same method utilized in Section 8.2 for creating carbon profiles in the soil is utilized here as well. The net peak area counts in the carbon ROI from a homogeneous soil volume with 5 w/o carbon and Profiles 1-4 (discussed in Chapter 8) were calculated utilizing the model. Figure 9.3 is similar to Figure 8.21, plotting the net peak areas versus the percent of the total carbon present in the top 5 cm and 10 cm.

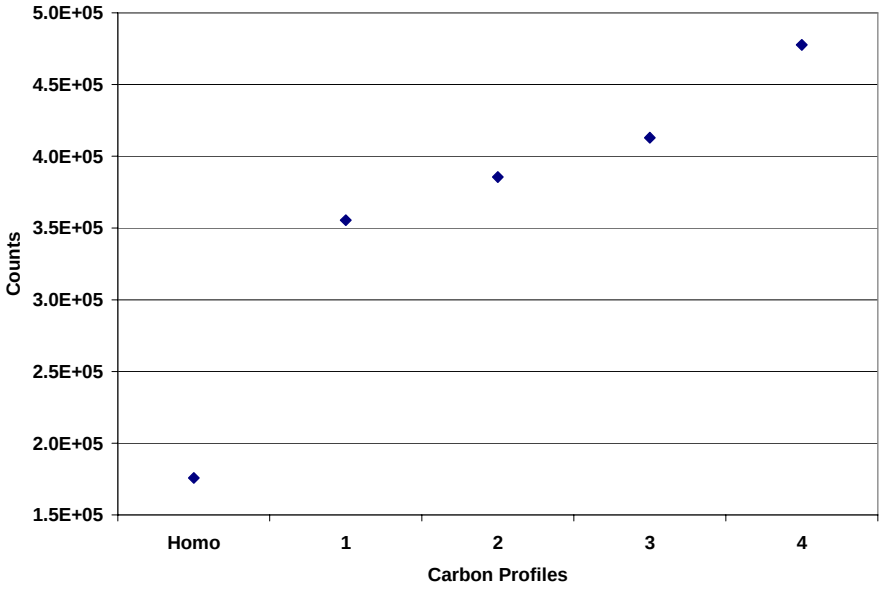

Figure 9.2. Net peak area counts in the carbon ROI for varying carbon profiles.

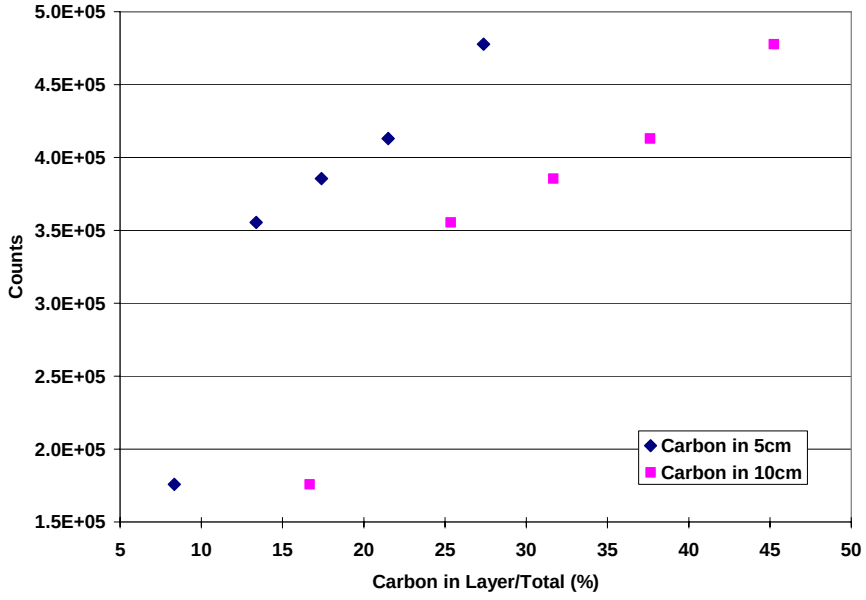

Figure 9.3. Net peak area counts in the carbon ROI for varying carbon profiles versus the percent of the total carbon present in the top 5 cm and 10 cm.

Linear least squares regression is used for line fitting. It can be observed in Figures 9.2 and 9.3 that for the same total carbon in the volume there are 5 different values for the counts for the five different carbon profiles. It will be difficult to account for varying carbon profiles especially if the total carbon in a given volume is constant as it is in this example. A solution to the issue of correcting for different carbon profiles with the same total carbon in a given volume is to utilize a time of flight technique [Biegalski, 2008].

Chapter 10: Conclusions and Recommendations

Soil carbon sequestration is a possible solution for slowing global climate change and is at the forefront of all discussions on the topic. The measurement of carbon in soil for the purpose of tracking the rate of soil sequestration is a critical issue. There remains no efficient way to repetitively sample large volumes of soil. The INS system is one method that could solve this problem. The INS system performs *in-situ*, non-destructive, multi-elemental analysis of soil. The calibration of the INS system is non-trivial. For that purpose, a benchmarked MCNP5 model of the system was generated in this work. The MCNP5 model working in series with Matlab enhances the understanding of the soil volume and related depth that the system measures and the effects of soil perturbations and carbon profiles on this volume and the total carbon response from the volume.

Four experiments were performed in order to benchmark the MCNP5 model. The benchmarks each concentrated on a specific part of the model: the fast neutron transport, creation of calibration curves, the pulse height distributions of the detectors, and the full model. The desired accuracy of the model is 10% within any of the experimental values. The benchmarks all achieved the desired accuracies except the detector 2 spectrum. As discussed above the relatively large error for detector 2 is due to the proximity of the sources to the detector and therefore the model is more sensitive to any human error in the geometric modeling of the source.

Soil bulk density affects the neutron and gamma transport through soil and thus affects the gamma yield at the detectors. However in the average bulk density range the effect is minimal. Moisture content affects the neutron and gamma transport through the increase of bulk density. As bulk density increases the carbon gamma ray production

increases proportionally. However, as moisture content increases the carbon gamma ray yield decreases proportionally.

The carbon gamma ray production reaches a plateau from shallower depths for increasing ρ_b. The detection depth of the system decreases with increased ρ_b. The maximum depth of the system for a ρ_b of 1.5 g cm^{-3} is around 25 cm. The levels of moisture in at measurement will have to be accounted for in order accurately interpret the results from the system. Stones reduce the carbon signal by displacing the soil in the volume measured by the INS system. The effect of stones on the carbon signal is predictable and relatively easy to account for. Carbon profiles have a strong effect on the carbon signal and will have to be accounted for in future measurements.

Two examples of the calibration curves created with the model were presented demonstrating the models ability to assist in the calibration the INS system in the future. The two calibration curve sets were a moisture-porosity-density dependent calibration curve and a carbon profile dependent curve. It was shown that the dry carbon concentration of the measured soil may be extrapolated with the knowledge of the moisture content of the soil at the time of the INS measurement. Therefore it is recommended that the research be done in the area of utilizing the hydrogen signal from the TNC spectra to quantitatively measure the presence of moisture in the soil volume measured. A set of real and numerical experiments utilizing the model should be performed to help understand the relationship of the H signal to the presence of moisture.

It is observed from the carbon profile calibration curves that carbon profiles have a strong effect on the carbon signal. A solution to the issue of correcting for different carbon profiles with the same total carbon in a given volume is to utilize a time of flight technique along with the associated particle technique [Biegalski, 2008].

The lack of comprehensive data set on any single soil measurement site prevented the benchmarking of the entire INS and TNC spectra. The importance of acquiring a complete data set, including a complete elemental analysis, total (inorganic and organic) carbon-, density-, and moisture-profiles, on no less than three soil measurement sites is highly recommended.

Appendices

APPENDIX A: TOP THIRTEEN ELEMENTS FROM THE MEIDAN AVERAGE OF WORLD SOILS WITH 2% BY CARBON AND A DENSITY OF 1.4 G CM^{-3}

Element	(% by weight w/ 2% C)
O	49
Si	33
Al	7.1
Fe	3.8
C	2
Ca	1.37
K	1.36
Na	0.63
Mg	0.63
Ti	0.46
N	0.10
S	0.09
P	0.08

APPENDIX B: EXAMPLE MCNP5 INS SYSTEM DECK FOR LOCATION AB-10 AT SOUTH CAROLINA FIELD

```
Location AB-10 at South Carolina Bonneau Soil w/ 1% Carbon and 5.5% H20
c ONLY DETECTORS 2 AND 3
c w/ Shielding in Place and DETECTOR ANGLED
c
c     CELL CARDS
c
c @@@@@@@@@@ Detectors @@@@@@@@@@@@@@@@@@
c
1   8 -2.7    (36 -56 -34 35 33 -32):(56 -37 33 -32 -34 46)
     :(33 -32 56 -37 -47 35):(56 -37 -46 47 44 -32):(56 -37 -46 47 -45 33)
     imp:n,p 1 $Al Detector Case 1/8" Al
2   9 -8.03  -41 40  47 -46 42 -44 #10 #5  #40 #43 #46 imp:n,p 1 $Det 1 Housing
3   9 -8.03  -41 40  47 -46 43 -42 #11 #6  #41 #44 #47 imp:n,p 1 $Det 2 Housing
4   9 -8.03  -41 40  47 -46 45 -43 #111 #7 #42 #45 #48 imp:n,p 1 $Det 3 Housing
5   7 -3.67  -50 51 -54 55 -52 502  #10  imp:n,p 1 $NaI Detector #1
6   7 -3.67  -50 51 -54 55 -522 533 #11  imp:n,p 1 $NaI Detector #2 (middle)
7   7 -3.67  -50 51 -54 55 -503 53  #111 imp:n,p 1 $NaI Detector #3
10  7 -3.67  -109 113 -116 119 -103 104 imp:n,p 1 $NaI Detector #1 Active Region
11  7 -3.67  -110 114 -117 120 -105 106 imp:n,p 1 $NaI Detector #2 Active Region
111 7 -3.67  -111 115 -118 121 -107 108 imp:n,p 1 $NaI Detector #3 Active Region
40 10 -0.45  -50 51 -95 92 -85 82 #5 #10  #43 imp:n,p 1 $2mm Al203 Det 1
41 10 -0.45  -50 51 -95 92 -81 87 #6 #11  #44 imp:n,p 1 $2mm Al203 Det 2
42 10 -0.45  -50 51 -95 92 -88 91 #7 #111 #45 imp:n,p 1 $2mm Al203 Det 3
43 11 -2.2   -50 51 -94 93 -84 83 #5 #10      imp:n,p 1 $4mm Teflon Det 1
44 11 -2.2   -50 51 -94 93 -80 86 #6 #11      imp:n,p 1 $4mm Teflon Det 2
45 11 -2.2   -50 51 -94 93 -89 90 #7 #111     imp:n,p 1 $4mm Teflon Det 3
46 13 -1.2   -51 96 -95 92 -52 502      imp:n,p 1 $2.5mm Si Rubber Bottom Det 1
47 13 -1.2   -51 96 -95 92 -522 533     imp:n,p 1 $2.5mm Si Rubber Bottom Det 2
48 13 -1.2   -51 96 -95 92 -503 53      imp:n,p 1 $2.5mm Si Rubber Bottom Det 3
50  9 -4     -37 41 -100           imp:n,p 1 $Detector 1 PMT as Scatterer
51  9 -4     -37 41 -101           imp:n,p 1 $Detector 2 PMT as Scatterer
52  9 -4     -37 41 -102           imp:n,p 1 $Detector 3 PMT as Scatterer
c
c @@@@@@@@@@ Shielding @@@@@@@@@@@@@@@@@@
c
8   6 -9.403   59 -58 -32 33  57 -35       imp:n,p 1 $Cerrobend
9   3 -1.465  -40 56 -44 45 -46 47         imp:n,p 1 $Compressed Boric Plates
12  8 -2.7 -62 61 -63 64 -65 66 #122 #1222 imp:n,p 1 $Front Water Aluminum Tank
13  8 -2.7 -61 76 -65 66 -73 75 #133 #1333 imp:n,p 1 $Side1 Water Aluminum Tank
14  8 -2.7 -61 76 -65 66 72 -74 #144 #1444 imp:n,p 1 $Side2 Water Aluminum Tank
```

```
122 4 -1.0192 611 -622 644 -633 666 -655   imp:n,p 1 $Front Borated Water
133 4 -1.0192 755 -733 766 -77 78 -655     imp:n,p 1 $Side1 Borated Water
144 4 -1.0192 722 -744 766 -77 78 -655     imp:n,p 1 $Side2 Borated Water
1222 12 -1.15e-3  611 -622 644 -633 -666 6666  imp:n,p 1 $Front Air in Tank
1333 12 -1.15e-3  755 -733 766 -77 -78 6666    imp:n,p 1 $Side1 Air in Tank
1444 12 -1.15e-3  722 -744 766 -77 -78 6666    imp:n,p 1 $Side2 Air in Tank
15  8 -2.7   -71 70 -72 73 -65 66              imp:n,p 1 $Al in Generator Box
c
c @@@@@@@@@@@@ Cart @@@@@@@@@@@
c
16  8 -2.7  ((65 -7 11 -10 14 -13):(12 -7 10 -8 14 -13)
          :(12 -7 9 -11 14 -13)) #17     imp:n,p 1 $Cart
17 12 -1.15e-3 16 -15 65 -7 20 -19 imp:n,p 1 $Cart opening between dets and gen
18  8 -2.7 (18 -17 20 -19 22 -21):(18 -188 20 -19 21 -65)
          imp:n,p 1 $Angled Cerrabend holder
c
c @@@@@@@@@@@ SOIL VOLUME @@@@@@@@@@@@
c
20  1 -1.56  -1 2 -3 4 -6 5  imp:n,p 1 $ SOIL VOLUME
c
30 0 -200 #1 (-33:32:-35:34:-36:41) (62:-61:63:-64:65:-66)
    (61:-76:73:-75:65:-66) (61:-76:-72:74:65:-66) (1:-2:3:-4:6:-5)
    (-59:58:32:-33:-57:35) (71:-70:72:-73:65:-66)
    #16 #17 #18 #50 #51 #52 imp:n,p 1 $Rest of the World
31  0        200                  imp:n,p 0 $Outside world

c       SURFACE CARDS
c
c %%%%%%%%%%
c Soil Volume
c %%%%%%%%%%
1 px   150
2 px  -100
3 py   100
4 py  -100
5 pz   30
6 pz   90
c %%%%%%%%%%%%%%%%%%%%%%%%%%%%%%%%%%%%%%%%%%%%%%%%%%%%%%%%%%%%%%%%%%%%%%%
c           Cart Planes
c %%%%%%%%%%%%%%%%%%%%%%%%%%%%%%%%%%%%%%%%%%%%%%%%%%%%%%%%%%%%%%%%%%%%%%%
7 pz   6.6675   $bottom cart plane
8 py   30.48    $Side cart plane
9 py  -30.48    $Side cart plane
10 py  29.21    $inside of cart angle
11 py -29.21    $inside of cart angle
12 pz -0.9525   $top of cart angle
```

```
13 px  116.555  $cart begin (detector side)
14 px  7.335    $cart end   (generator side)
c %%%%%%% Opening between Detectors and Generator **********
15 px  65.755   $detector side plane
16 px  32.735   $generator side plane
c %%%%%%%%% Cerrabend Holder Angle 1/4" thick Al 1.5" by 1.5" *********
17  px 44.8     $upright angle detector side
18  px 44.165   $upright angle generator side
188 px 47.975   $bottom angle detector side
19  py 22.86    $Side
20  py -22.86   $Side
21  pz 5.3975   $bottom angle top side
22  pz 2.2225   $top of angle
c
c %%%%%%%%%%%%%%%%%%%%%%%%%%%%%%%%%%%%%%%%%%%%%%%%%%%%%%%%%%%%%%%%%%%%%%%
c       Detectors' Case in x',y',z'
c %%%%%%%%%%%%%%%%%%%%%%%%%%%%%%%%%%%%%%%%%%%%%%%%%%%%%%%%%%%%%%%%%%%%%%%
32 1 py  21.9125  $outer Case plane Det 1 side
33 1 py -21.9125  $outer Case plane Det 3 side
34 1 pz  8.3675   $outer Case back plane
35 1 pz -6.6675   $outer Case front plane
36 1 px -10.795   $bottom Case plane
37 1 px  13.23    $top Case plane
c %%%%%%%%%%%%%%%%%%%%%%%%%%%%%%%%%%%%%%%%%%%%%%%%%%%%%%%%%%%%%%%%%%%%%%%
c       Detector Housing in x',y',z'
c %%%%%%%%%%%%%%%%%%%%%%%%%%%%%%%%%%%%%%%%%%%%%%%%%%%%%%%%%%%%%%%%%%%%%%%
40 1 px -7.77   $bottom housing plane
41 1 px  8.23   $top housing plane
42 1 py  7.2    $Det 2/1 housing plane
43 1 py -7.2    $Det 2/3 housing plane
44 1 py  21.60  $Det 1 outer housing plane
45 1 py -21.60  $Det 3 outer housing plane
46 1 pz  8.05   $Housing back plane
47 1 pz -6.35   $Housing front plane
c %%%%%%%%%%%% Stainless Steel representing PMT as scatterer %%%%
100 1 c/x  14.4 0.85 6.75  $Det 1 PMT cylinder
101 1 c/x  0    0.85 6.75  $Det 2 PMT cylinder
102 1 c/x -14.4 0.85 6.75  $Det 3 PMT cylinder
c %%%%%%%%%%%%%%%%%%%%%%%%%%%%%%%%%%%%%%%%%%%%%%%%%%%%%%%%%%%%%%%%%%%%%%%
c Material between Detector and Housing: 4mm Teflon & 2mm Al2O3 (sides)
c & 2.5mm Silicon rubber plate (bottom) in x', y',z'
c %%%%%%%%%%%%%%%%%%%%%%%%%%%%%%%%%%%%%%%%%%%%%%%%%%%%%%%%%%%%%%%%%%%%%%%
80 1 py 6.75    $Teflon on Det 2 on Det 1 side
81 1 py 6.95    $Al2O3 on Det 2 on Det 1 side
82 1 py 7.45    $Al2O3 on Det 1 inside plane
83 1 py 7.65    $Teflon on Det 1 inside plane
```

```
84 1 py 21.15   $Teflon on Det 1 outer plane
85 1 py 21.35   $Al2O3 on Det 1 outer plane
86 1 py -6.75   $Teflon on Det 2 on Det 3 side
87 1 py -6.95   $Al2O3 on Det 2 on Det 3 side
88 1 py -7.45   $Al2O3 on Det 3 inside plane
89 1 py -7.65   $Teflon on Det 3 inside plane
90 1 py -21.15  $Teflon on Det 3 outer plane
91 1 py -21.35  $Al2O3 on Det 3 outer plane
92 1 pz -6.10   $Al2O3 front plane
93 1 pz -5.90   $Teflon front plane
94 1 pz  7.6    $Teflon back plane
95 1 pz  7.8    $Al2O3 back plane
96 1 px -7.47   $Silicon Rubber bottom
c %%%%%%%%%%%%%%%%%%%%%%%%%%%%%%%%%%%%%%%%%%%%%%%%%%%%%%%%%%%%%%%%%%%%%%%
c       Detector Planes in x',y',z'
c %%%%%%%%%%%%%%%%%%%%%%%%%%%%%%%%%%%%%%%%%%%%%%%%%%%%%%%%%%%%%%%%%%%%%%%
50  1 px  7.98   $top plane
51  1 px -7.22   $bottom plane
52  1 py  20.75  $Det 1 outer plane
502 1 py  8.05   $Det 1 inside plane
522 1 py  6.35   $Det 2 plane on Det 1 side
533 1 py -6.35   $Det 2 plane on Det 3 side
503 1 py -8.05   $Det 3 inside plane
53  1 py -20.75  $Det 3 outer plane
54  1 pz  7.2    $back plane
55  1 pz -5.5    $front plane
c %%%%%%%%%%%%%%%%%%%%%%%%%%%%%%%%%%%%%%%%%%%%%%%%%%%%%%%%%%%%%%%%%%%%%%%
c         Active Detector Region
c %%%%%%%%%%%%%%%%%%%%%%%%%%%%%%%%%%%%%%%%%%%%%%%%%%%%%%%%%%%%%%%%%%%%%%%
103 1 py  20.75  $Det 1 outer plane active region
104 1 py  8.05   $Det 1 inside plane active region
105 1 py  6.25   $Det 2 plane on Det 1 side active region
106 1 py -6.25   $Det 2 plane on Det 3 side active region
107 1 py -8.05   $Det 3 inside plane active region
108 1 py -20.75  $Det 3 outer plane active region
109 1 px  7.98   $Det 1 top plane of active region
110 1 px  7.98   $Det 2 top plane of active region
111 1 px  7.98   $Det 3 top plane of active region
113 1 px -7.22   $Det 1 bottom plane of active region
114 1 px -7.00   $Det 2 bottom plane of active region
115 1 px -7.22   $Det 3 bottom plane of active region
116 1 pz  7.2    $Det 1 back plane of active region
117 1 pz  7.2    $Det 2 back plane of active region
118 1 pz  7.2    $Det 3 back plane of active region
119 1 pz -5.5    $Det 1 front plane of active region
120 1 pz -5.5    $Det 2 front plane of active region
```

```
121 1 pz -5.5    $Det 3 front plane of active region
c *********** Compressed Boric Acid plates in Detector Housing *******
56 1 px -10.4775
c *********** Cerrabend ************************
57 1 pz -7.62    $generator side plan
58 1 px  1.6323  $bottom plane
59 1 px -23.7677   $top plane
c %%%%%%%%%%%%%%%%%%%%%%%%%%%%%%%%%%%%%%%%%%%%
c                Shielding Surfaces
c %%%%%%%%%%%%%%%%%%%%%%%%%%%%%%%%%%%%%%%%%%
61   px  22.86     $Generator side surface of front water TANK
611  px  23.1775   $Generator side surface of front water
62   px  43.18     $Detector side surface of front water TANK
622  px  42.8625   $Detector side surface of front water
63   py  19.05     $Side surface of front water TANK
633  py  18.7325   $Side surface of front water
64   py -19.05     $Side surface of front water TANK
644  py -18.7325   $Side surface of front water
65   pz  6.0325    $bottom surface of shielding boxes
655  pz  5.715     $bottom surface of shielding water
66   pz -14.2875   $top surface of shielding boxes
666  pz -12.065    $top surface FRONT of shielding water (7 inches of water)
6666 pz -13.97     $top surface of AIR in shielding tanks
70   px  14.605    $Generator side surface of generator shielding
71   px  22.5425   $Detector side surface of generator shielding
72   py  7.858125  $side surface of generator shielding and inside of water tank
73   py -7.858125  $side surface of generator shielding and inside of water tank
c ************************
c Side Borated Water Tanks
c ************************
722 py  8.175625   $side surface of inside of water
733 py -8.175625   $side surface of inside of water
74  py  28.178125  $outside surface of side water TANK
744 py  27.860625  $outside surface of side water
75  py -28.178125  $outside surface of side water TANK
755 py -27.860625  $outside surface of side water
76  px -15.24      $Generator side surface of water TANK
766 px -14.9225    $Generator side surface of water
77  px  22.5425    $Detector side surface of water
78  pz -6.985      $top surface of SIDE shielding water (5 inches of water)
200 so  300

c              DATA CARDS
mode n p
c  dump every 24 hrs
prdmp 1j -1440 1j 1
```

```
c 100 keV Neutron Energy Cutoff
Cut:n 1j 0.1
phys:n 1j 14 $analog neutron transport
c <<<<<<<<<<<<<<<<<<<<<<<<<<<<<<<<<<<<<<<<<<<<<<<<<<<<<<<<<<<<<<<<<<<<<<<
c Coordinate Transformation for Detector Surface => 45 degrees from X
c >>>>>>>>>>>>>>>>>>>>>>>>>>>>>>>>>>>>>>>>>>>>>>>>>>>>>>>>>>>>>>>>>>>>
*TR1 68 0 -8  45 90 135  90 0 90  45 90 45
c
sdef
c ********************
c begin material cards
c ********************
c    Location AB-10 at South Carolina
c    Bonneau Soil w/ 1% Carbon and 5.5% H20
c ***********************************
m1   8016      -53.5       $Oxygen
     14000     -41.75      $Silicon
     13027     -0.526      $Aluminum
     26000     -0.526      $Iron
     6000      -1          $Carbon
     20000     -0.526      $Calcium
     19000     -0.526      $Potassium
     11023     -0.526      $Sodium
     12000     -0.526      $Magnesium
     40000.42c -0.526      $Zirconium
     1001      -0.5
c ***********************************
m2   6000       1          $carbon
m3   1001       3          $Boric acid
     5010       0.199
     5011       0.80
     8016       3
m4   1001       -0.1081076584 $Borated water/ 4.8 wt% H3BO3
     8016       -0.8834
     5010       -0.0015447980
     5011       -0.0068508435
m5   26000      1           $Iron
c ************ cerrabend ************
m6   83209      -0.5        $Bismuth
     82000      -0.267      $Lead
     50000      -0.133      $Tin
     48000      -0.1        $Cadmium
m7   11023      0.5         $NaI
     53127      0.5
m8   13027      1           $ Aluminum
c ********* Stainless Steel Type 304 den 8.03 g/cc *********
```

```
m9   26000     -71
     24000     -18
     28000     -8
     25055     -2
     7014      -0.10
     16000     -0.03
     6000      -0.08
     14000     -0.75
     15031     -0.05
c ******** Al2O3 den=0.45g/cc*********
m10  13027      2
     16000      3
c ********* Teflon  den=2.2g/cc ***************
m11  6000       1
     9019       2
c ************ air den=1.15e-3g/cc
m12  8016      -0.23
     7014      -0.77
c ********* Silicon Rubber den=1.2g/cc
m13  14000      1
     8016       1
c end material cards
c
c begin tallies
c
c **********neutron tallies**********************
e74 2.53e-8 5e-7 0.1 1 5 13.9 14
fc74 Track length neutron flux tally in detector volume
f74:n 10 11 111 T
fc14 Track length neutron tally in aluminum shielding
f14:n 15
c
fc84 *********gamma tally 1 ***************************
e84 0 1e-5 2046i 14
f84:p 10
c
fc8 *********Pulse Height Tally 1 ***************************
e8 0 1e-5 2046i 14
f8:p 10
c
fc18 *********Broadened Pulse Height Tally 1***************************
e18 0 1e-5 2046i 14
f18:p 10
FT18 GEB 0.0116 0.0685 0
c
fc94 *********gamma tally 2 ***************************
```

```
e94 0 1e-5 2046i 14
f94:p 11
c
fc28 *********Pulse Height Tally Detector 2**************************
e28 0 1e-5 2046i 14
f28:p 11
c
fc38 *********Broadened Pulse Height Tally Detector 2***********************
e38 0 1e-5 2046i 14
f38:p 11
FT38 GEB -0.0073 0.078 0
c
fc104 *********gamma tally 3**************************
e104 0 1e-5 2046i 14
f104:p 111
c
fc48 *********Pulse Height Tally Detector 3**************************
e48 0 1e-5 2046i 14
f48:p 111
c
fc58 *********Broadened Pulse Height Tally Detector 3***********************
e58 0 1e-5 2046i 14
f58:p 111
FT58 GEB 0.0116 0.0685 0
c
fc114 *********gamma tally**************************
e114 0 1e-5 2046i 14
f114:p (10 11 111)
c
fc68 *********Pulse Height Tally Sum of Detectors 1,2 & 3 *********************
e68 0 1e-5 2046i 14
f68:p (10 11 111)
c
fc78 *********Broadened Pulse Height Tally Sum of Detectors 1,2 & 3 ***********
e78 0 1e-5 2046i 14
f78:p (10 11 111)
FT78 GEB -0.1014 0.1947 0
c
fc88 *********Broadened Pulse Height Tally Sum of Detectors 2 & 3 only ********
e88 0 1e-5 2046i 14
f88:p (11 111)
FT88 GEB -0.1014 0.1947 0
c
c  end tallies
```

nps 5e8

APPENDIX C: ENGINEERING DRAWINGS OF NAI DETECTORS FROM SCIONIX

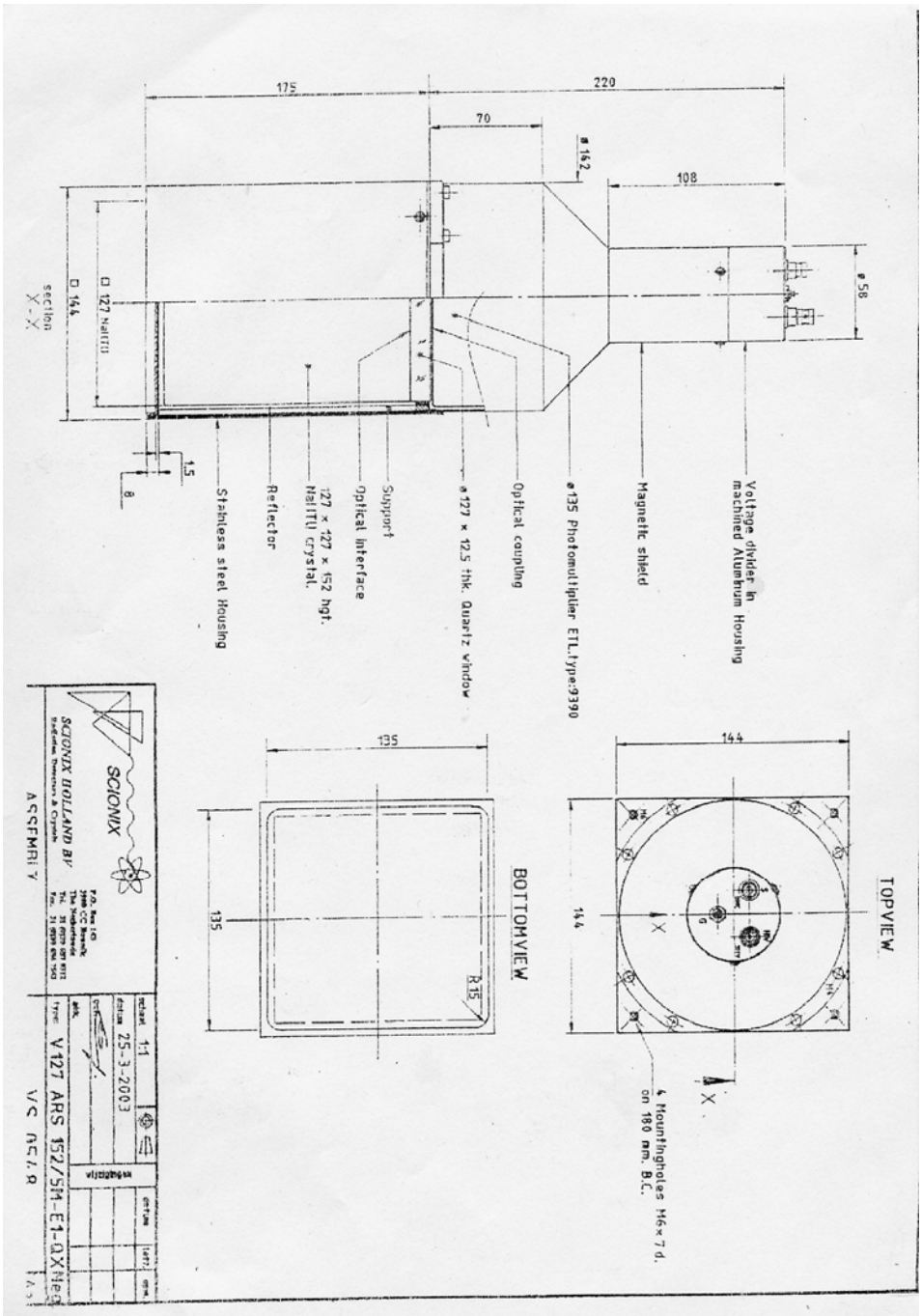

APPENDIX D: EMAIL COMMUNICATION WITH SCIONIX ON DETECTOR MATERIALS

-----Original Message-----
From: Paul Schotanus [mailto:scionix@wxs.nl]
Sent: Monday, May 07, 2007 3:44 AM
To: Doron, Oded
Subject: RE: XIA/CARBON: detector

Hello Oded,

At the sides of the crystals there are 4 mm thick TEFLON plates followed by 2 mm of packed Al2O3 (density 0.45 g / cc).
At the bottom there is a 2.5 mm thick Silicon rubber plate (density 1.2 g / cc) and a 0.2 mm thick Nylon reflector (can be neglected).

I hope this information helps.

Best regards,

PAUL

APPENDIX E: SNIP OF MESH TALLY OUPUT

```
100^3 cm lattice of 1 cm^3 volumes for neutron flux measurements
Number of histories used for normalizing tallies =       1000000.00

 Mesh Tally Number   4
 This is a neutron mesh tally.

 Tally bin boundaries:
    X direction:     -0.50      0.50      1.50      2.50      3.50
4.50      5.50      6.50      7.50      8.50      9.50     10.50
11.50     12.50     13.50     14.50     15.50     16.50     17.50
18.50     19.50     20.50     21.50     22.50     23.50     24.50
25.50     26.50     27.50     28.50     29.50     30.50     31.50
32.50     33.50     34.50     35.50     36.50     37.50     38.50
39.50     40.50     41.50     42.50     43.50     44.50     45.50
46.50     47.50     48.50     49.50     50.50     51.50     52.50
53.50     54.50     55.50     56.50     57.50     58.50     59.50
60.50     61.50     62.50     63.50     64.50     65.50     66.50
67.50     68.50     69.50     70.50     71.50     72.50     73.50
74.50     75.50     76.50     77.50     78.50     79.50     80.50
81.50     82.50     83.50     84.50     85.50     86.50     87.50
88.50     89.50     90.50     91.50     92.50     93.50     94.50
95.50     96.50     97.50     98.50     99.50    100.50
    Y direction:     -0.50      0.50
    Z direction:     29.00     30.00
    Energy bin boundaries: 0.00E+00 1.00E+00 2.00E+00 3.00E+00 4.00E+00
5.00E+00 6.00E+00 7.00E+00 8.00E+00 9.00E+00 1.00E+01 1.10E+01 1.20E+01
1.30E+01 1.40E+01
```

Energy	X	Y	Z	Result	Rel Error
1.000E+00	0.000	0.000	29.500	1.53215E-05	2.09720E-01
1.000E+00	1.000	0.000	29.500	1.79361E-05	1.92468E-01
1.000E+00	2.000	0.000	29.500	2.02392E-05	1.86665E-01
1.000E+00	3.000	0.000	29.500	1.72370E-05	2.04136E-01
1.000E+00	4.000	0.000	29.500	1.37252E-05	2.23310E-01
1.000E+00	5.000	0.000	29.500	1.16699E-05	2.37253E-01
1.000E+00	6.000	0.000	29.500	1.37218E-05	2.12546E-01
1.000E+00	7.000	0.000	29.500	1.90202E-05	1.79616E-01
1.000E+00	8.000	0.000	29.500	1.86872E-05	1.90745E-01
1.000E+00	9.000	0.000	29.500	1.35983E-05	2.09150E-01
1.000E+00	10.000	0.000	29.500	1.47609E-05	2.18513E-01
1.000E+00	11.000	0.000	29.500	1.24636E-05	2.08617E-01
1.000E+00	12.000	0.000	29.500	1.34368E-05	2.23695E-01
1.000E+00	13.000	0.000	29.500	1.40292E-05	1.99310E-01
1.000E+00	14.000	0.000	29.500	1.53142E-05	2.11451E-01
1.000E+00	15.000	0.000	29.500	1.51561E-05	2.00390E-01
1.000E+00	16.000	0.000	29.500	2.17768E-05	1.82733E-01
1.000E+00	17.000	0.000	29.500	1.68578E-05	2.00540E-01
1.000E+00	18.000	0.000	29.500	1.30067E-05	2.23136E-01
1.000E+00	19.000	0.000	29.500	1.13634E-05	2.31971E-01
1.000E+00	20.000	0.000	29.500	1.37309E-05	2.19119E-01

1.000E+00	21.000	0.000	29.500	1.96460E-05	1.88146E-01
1.000E+00	22.000	0.000	29.500	1.54449E-05	1.96966E-01
1.000E+00	23.000	0.000	29.500	1.60897E-05	2.12437E-01
1.000E+00	24.000	0.000	29.500	1.50527E-05	1.97051E-01

APPENDIX F: ENDF NUCLEAR CROSS SECTIONS

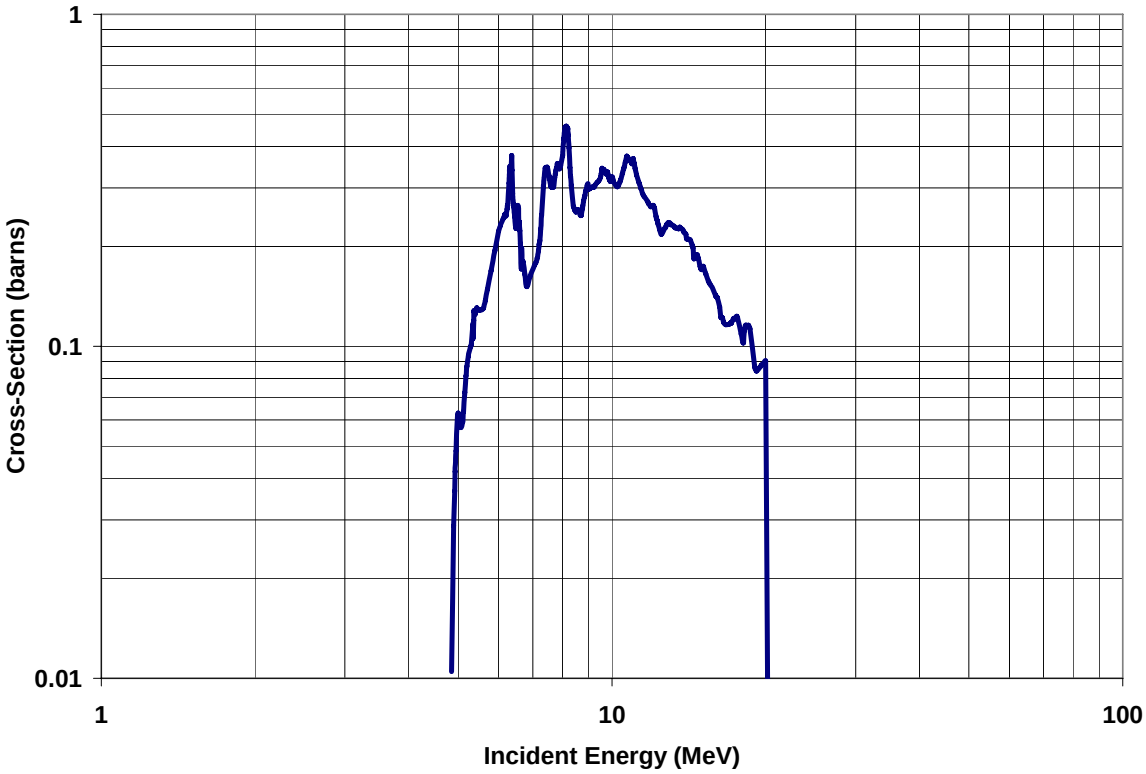

Figure F.1. C (n,n',γ) cross-section as function of incident neutron energy.

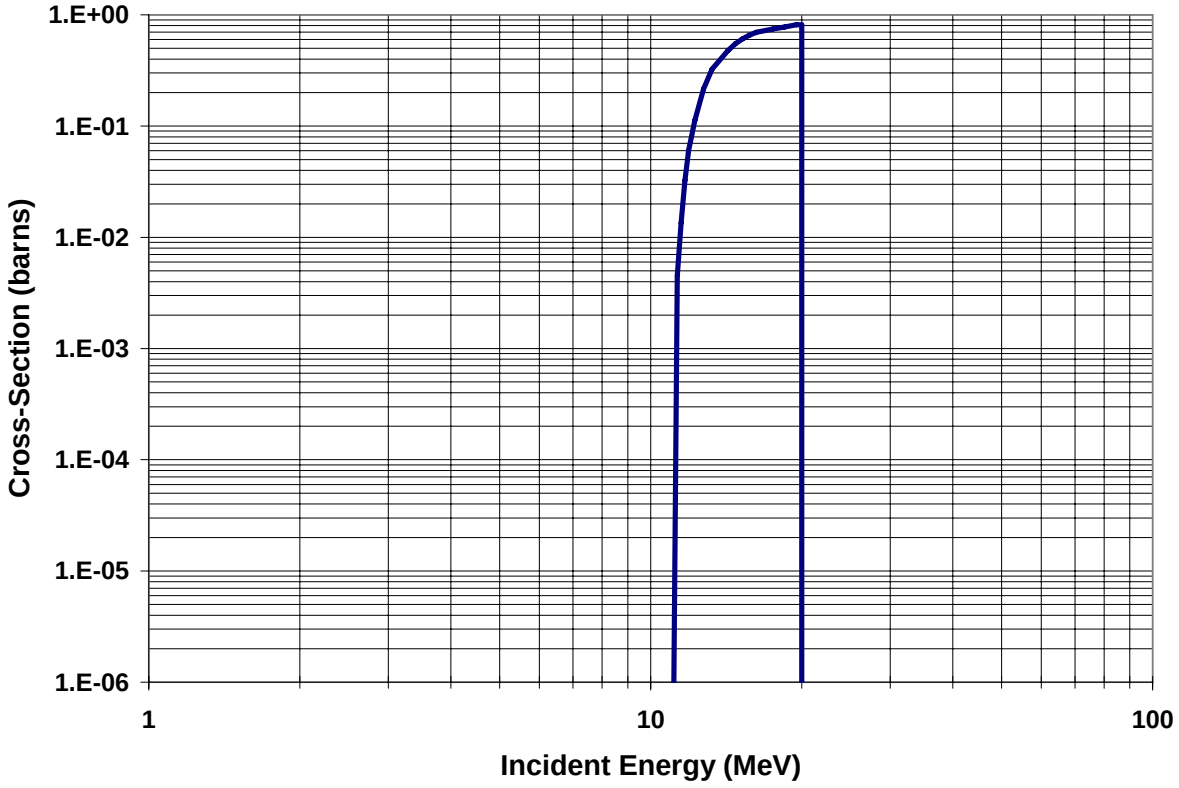

Figure F.2. ^{63}Cu (n,2n)^{62}Cu cross-section as function of incident neutron energy.

APPENDIX G: WEIGHT PERCENT CALCULATIONS AND ADJUSTMENTS

When modeling soil it is important to know what the weight percent, wt%, is of every element in the soil composition. The wt%'s of the soil composition are affected if an element is added or removed, or if an element's wt% is increased or decreased in the soil (Fig. G.1). The wt%'s of the rest of the soil elements must be adjusted accordingly, utilizing equations G.1-G.3, given below.

Element	Wt%
O	wt_i
C	wt_i
Si	wt_i

=>

Element	Wt%
O	wt_n
C	wt_n
Si	wt_n
Al	wt

Figure E.1. An example of adjusting elemental weight percents as a result of the addition of an element (Al here) to a soil composition.

New weight percent, wt_n, with initial percent, wt_i, due to adding element with weight percent *wt*

$$wt_n = (100 - wt) * \left(\frac{wt_i}{100} \right) \tag{G.1}$$

New weight percent, wt_n, with initial percent, wt_i, due to removing element with weight percent *wt*

$$wt_n = \frac{wt_i}{100 - wt} * 100 \tag{G.2}$$

New weight percent, wt_n, with initial percent, wt_i, due to increasing or decreasing element with weight percent *wt* from wt_{old} to wt_{new}

$$wt_n = \left[\left(wt_{old} - wt_{new} \right) * \frac{wt_i}{100} \right] + wt_i \qquad \text{(G.3)}$$

APPENDIX H: GEOMETRIC AND PEAK EFFICIENCY FOR WELL-TYPE NAI

A ^{22}Na source that was assayed on 9/12/2003 was utilized to find the combined geometric and peak efficiency (0.511 keV) of a well-type NaI detector on 12/16/03.

- The activity of the source on the day of the assay was 1.512 x 10^{-9}Ci or 55.9 dps
- The net ^{22}Na counts in the 0.511 keV peak in the well type detector were 5.75counts s^{-1} (1725 counts $300s^{-1}$)
- The combined geometric and peak efficiency of the well-type detector at 0.511 keV is given below in Equation H.1.

$$\varepsilon = \frac{5.75}{55.9 * 0.9046} = 0.11 \qquad \text{(H.1)}$$

where 0.9046 is the total positron emission probability of the source

References

Alfassi, Z. B, Activation Analysis, CRC Press, Boca Raton, Florida, 1990.

Biegalski, S.R., Doron, O., Wielopolski, L., "The Time and depth dependent fluxes due to 14 MeV neutrons impinging soil", J. Rad. Nuc. Chem., In Press, Vol. 282 (2008), 1.

Borsarua, M., Biggsb, M., Nicholsc, W., Bos, F., "The application of prompt-gamma neutron activation analysis to borehole logging for coal", Appl. Radiat. Isot., Vol. 54 (2001), pp. 335 – 343.

Cambardella, C.A. and Elliot, E.T., "Methods of physical separation and characterization of soil organic matter fractions" Geoderma 56(1993.), pp.449-457.

Christy, C. D., Drummond, P., Laird, D. A., "An on-the-go spectral reflectance sensor for soil", ASAE Annual Meeting, Paper No. 031044, 2003

Cremers, D. A., Ebinger, M. H., Breshears, D. D., Unkefer, P. J., Kammerdiener, S. A., Ferris, M. J., Catlett, K. M., Brown, J. R., "Measuring total soil carbon with laser-induced breakdown spectroscopy (LIBS)", J. Environ. Qual., Vol. 20 (2001), pp. 2202-2206.

Dep, L., Belbot, M., Vourvopoulos, G. and Sudar, S., "Pulsed neutron-based on-line coal analysis", J. Radioanal and Nucl. Chem., vol. 234, pp 107-112, 1998.

Doron, O., Wielopolski, L., Biegalski, S.R., "Advantages of mesh tallying in MCNP5 for soil analysis calculations", J. Rad. Nuc. Chem., In Press, Vol. 281 (2008) 1.

Ebinger, M.H., Norfleet, M. L., Breshears, D. D., Cremers, D. A., Ferris, M. J., Unkefer, P. J., Lamb, M. S., Goddard, K. L., Meyer, C. W., "Extending the applicability of laser-induced breakdown spectroscopy for total soil carbon measurement", Soil Sci. Soc. Am. J, Vol. 67 (2003), pp. 1616-1619.

Electronic files for neutron cross-sections data maintained by National Nuclear Data Center (NNDC), Brookhaven National Laboratory (BNL) at http://www.nndc.bnl.gov

Ellert, B.H., and Bettany, J.R., "Calculation of organic matter and nutrients stored in soils under contrasting management regimes", Can. J. Soil Sci. 75(1995.), pp.529-538.

Ellis, K.J., Yasumura, S., Morgan, W.D., (eds.), "In Vivo Body Composition Studies", The Institute of Physical Sciences in Medicine, 1987.

Emanuel, W. R., Shugart, H. H., Stevenson M. P., "Climate changes and the broad-scale distribution of terrestrial ecosystem complexes", Climate Change, Vol. 7 (1985), pp. 29-30.

Ertek, C., Haselberger, N., "Measurement of density and water content of soil using photon multiple scattering", Nuclear Instruments and Methods in Physics Research, Vol. 227 (1984), pp 182-185.

Frank, V., and Tolgyessy, J., The chemistry of soil (Chapter 7) in: "Chemistry and Biology of Water, Air and Soil Environmental Aspects. Edited by J. Tolgyessy, Elsevier, (1993).

Garcia-Olivia, F., and Masera, O. R., "Assessment and measurement issues related to soil carbon sequestration in land-use, land-use change, and forestry (LULUCF) projects under the Kyoto Protocol", Climate Change, Vol. 65 (2004), pp. 347-364.

Gehl, R. J., and Rice, C. W., "Emerging technologies for *in situ* measurement of soil carbon", Climatic Change, Vol. 80 (2007), pp. 43-54.

Girard, S. M., and Shinn, J. B. (Ed.), "MCNP - A General Monte Carlo N-Particle Transport Code, Version 5", Los Alamos National Laboratory Report, LA-CP-03-0245, 2003.

Gozani, T., Elsalim, M., Strellis, D. and Brown, D., "Fusion of time-dependent gamma production spectra from thermal neutron capture and fast neutron inelastic scattering to improve material detection", Nucl. Instrum. Methods, vol. A505, pp. 486-489, 2003.

Choi, H., Roh, G., "Benchmarking MCNP and WIMS/RFSP against measurement data - I: Deuterium critical assembly", Nucl. Sci. Eng. Vol. 146 (2), pp.188-199, 2004

Harling, O.K., Bernard, J.A., Zamenhof, R.G. (eds.), "Neutron beam design, development, and performance for neutron capture therapy", Plenum Press, New York and London, 1990.

Heath, R.L., "The Texas Convention on the measurement of 14-MeV neutron fluxes from accelerators", Proceeding of the 1965 International Conference on Modern Trends in Activation Analysis, College Station, Texas, April 1965.

Howell, S.L., Sigg, R.A., Moore, F.S., Devol, T.A., "Calibration and validation of a monte carlo model for pgnaa of chlorine in soil", J. Rad. Nuc. Chem., 244 (2000) 173.

Hussein, E.M.A., Desrosiers, M., and Waller, E. J., "On the use of radiation scattering for the detection of landmines", Rad. Phys. Chem., Vol. 73 (2005), pp. 7-19.

Hu-Xia, S., Bo-Xian, C., Ti-Zhu, L., Di, Y., "Precise Monte Carlo simulation of gamma-ray response functions for an NaI(Tl) detector", App. Rad. Iso., Vol. 57 (2002), pp. 517-524.

Jenkinson, D. S., Adams, D. E., Wild, A., "Model estimates of CO_2 emissions from soil in response to global warming", Nature, Vol.351 (1991), pp. 34-306.

Keeling, C. D., Piper, S. C., Bacastow, R. B., Wahlen, M., Whorf, T. P., Heimann, M., and Meijer, H. A., "Atmospheric CO_2 and $^{13}CO_2$ exchange with the terrestrial biosphere and oceans from 1978 to 2000: observations and carbon cycle implications, pages 83-113, in 'A History of Atmospheric CO_2 and its effects on Plants, Animals, and Ecosystems', editors, Ehleringer, J.R., T. E. Cerling, M. D. Dearing, Springer Verlag, New York, 2005.

Khatamov, Sh., Zhumamuratov, A., Ibragimov, B., Tillaev, T., "Neutron-activation soil analysis in ecological investigations", Atomic Energy, Vol. 89, No. 2 (2000), pp. 680-684.

Knoll, G.E., Radiation Detection and Measurement, 3rd edition, John Wiley and Sons, Inc., Hoboken, NJ 2000.

Kyoto Protocol to the United Nations Framework Convention on Climate Change, http://unfccc.int/resource/docs/convkp/kpeng.pdf

Lal, R., Kimble, Jm., Follett, Rf., and Cole, Cv., The Potential of U.S. Cropland to Sequester Carbon and Mitigate the Greenhouse Effect, CRC Press LLC, (1999).

Lamarsh, J. R., and Baratta, A. J., Introduction to Nuclear Engineerin, 3rd edition, Prentice Hall, Upper Saddle River, NJ 2001.

Lieser, K. H., Nuclear and Radiochemistry: Fundamentals and Applications, 2nd edition, Wiley-Vch, Weinheim, Germany 2001.

Macdonald, J., Smith, P. H., Assinder, D. J., "The development and use of an *in situ* gamma-ray spectrometry system in North Wales", Journal of Radiological Protection, Vol. 16, No. 2 (1996), pp 115-127.

Masera, O. R., Garza-Caligaris, J. F., Kanninen, M., Karjalainen, T., Nabuurs, G. J., Pussinen, A., de Jong, B. J., Mohren, F., "Modeling carbon sequestration in afforestation and forest management properties: The CO2Fix V.2 Approach", Ecological Modelling, Vol. 164 (2003), pp. 177-199.

Maucec, M., "Implementation of variance-reduction techniques for Monte Carlo nuclear logging calculations with neutron sources", Rad. Prot. Dos., 116 1-4 (2005) 498.

Maucec, M., and Rigollet, C., "Monte Carlo simulations to advance characterisation of landmines by pulsed fast/thermal neutron analysis", Appl. Radiat. Isot., Vol. 61 (2004) pp. 35-42.

Metropolis; N., Ulam, S., "The Monte Carlo method:, J. Amer. Stat. Ass., Vol. 44, (Sep., 1949), 247, pp. 335-341.

MF Physics Corporation, "Texas Convention technique for measuring neutron output", Technical Bulletin #109.

Mitra, S., Wielopolski, L. and Hendrey, G.,"Comparison of a digital and an analog signal processing system for neutron inelastic gamma-ray spectrometry", Appl. Radiat. Isot., vol. 61 (2004), pp. 1463 – 1468.

Mitra, S., Wielopolski, L., Tan, H., Fallu-Labruyere, A., Hennig, W., Warburton, W. K., "Concurrent measurement of individual gamma-ray spectra during and between fast neutron pulses", IEEE Trans.Nucl.Sci., Vol. 54 (1) pp.192-196 Part 2, FEB 2007.

Mosegaard, K., Tarantola, A., "Monte Carlo sampling of solutions to inverse problems", J. Geophys. Res., Vol. 100 (1995), B7, pp.12431-12447.

Naqvi, A. A., Nagadi, M. M., Khateeb-ur-Rehman, Maslehuddin, M., Kidwai, S., Nassar, R., "350 keV accelerator-based neutron transmission setup at KFUPM for hydrogen detection", Nuclear Instruments and Methods in Physics Research A, Vol. 487 (2002), pp. 667-675.

Nelson, D.W., and Sommers, L.E, "Total carbon, organic carbon, and organic matter" Sparks et al. (ed.) Methods of soil analysis. Part 3. SSSA Book Ser. No. 5. SSA and ASA (1996), Madison, WI, pp.961-1010.

Nelson, D.W., and Sommers, L.E, "Total carbon, organic carbon, and organic matter" Methods of soil analysis. Part 2, 2nd ed, Page (ed.) Agronomy 9:539-579.

Nir-El, Y., Haquin, G., "Minimum detectable activity in in situ γ-ray spectrometry", Applied Radiation and Isotopes, Vol. 55 (2001), pp. 197-203.

Novak, J., Personal Communication, USDA-ARS-CPRC, Florence, SC, 2007.

Odom, R.C., Bailey, S.M. and Wilson, R.D.,"Benchmarking computer simulations of neutron-induced, gamma-ray spectroscopy for well logging", Appl. Radiat. Isot., Vol. 48 (1997), pp.1321-1328.

Pansu, M., Gautheyrou, J., Loyer, J. Y., Soil analysis: sampling, instrumentation, and quality control. Lisse, Netherlands, 2001.

Parton, W. J., et. al., "Observations and modeling biomass and soil organic matter dynamics for the grassland biome worldwide", Global Biogeochemical Cycles, Vol.7, No.4 (1993), pp. 785-809.

Pelowitz, D. B. (Ed.), "MCNPX Version 2.5.0 User's Manual", LANL Report, LA-CP-05-0369, (2005).

Qi, F., Wei, L., Yansui, L., Yanwu, Z., Yonghong, S., "Impact of desertification and global warming on soil carbon in northern China", Journal of Geophysical Research, Vol. 109 (2004), DO2104.

Reeves, J. B., McCarty, G. W. III, Reeves, V. B., "Mid-infrared and diffuse reflectance spectroscopy for the quantitative analysis of agricultural soils", J. Agric. Food Chem., Vol. 49 (2001), pp. 766-772.

Roh, G., Choi, H.," Benchmark calculations for standard and DUPIC CANDU fuel lattices compared with the MCNP-4B code", Nucl. Tech., Vol. 132 (1), pp. 128-151, 2000.

Schaeffer, N.M., Reactor Shielding for Nuclear Engineers. U.S. Atomic Energy Commission, 1973.

Schweitzer, J.S., "Nuclear techniques in the oil industry", Nucl. Geophys., vol.5, pp. 65-90, 1991.

Shultis, K. J., and Faw, R. E., Radiation Shielding, American Nuclear Society, La Grange, IL., 2000.

Tölgyessy, J. (Ed.), Chemistry and Biology of Water, Air and Soil: Environmental Aspects, Elsevier, The Netherlands, 1993.

Vinogradov, A.P., The Geochemistry of Rare and Dispersed Chemical Elements in Soil. Chapman and Hall Limited, (1959).

Vourvopoulos, G., and Womble, P.C., "Pulsed fast/thermal neutron analysis: A technique for explosives detection", Talanta, vol.54, pp. 459-468, 2001.

Wielopolski, L., "Emerging modalities for soil carbon analysis: sampling statistics and economics workshop", BNL, January 19-20, 2006.

Wielopolski, L., "Monte Carlo calculation of the average solid angle subtended by a parallelepiped detector from a distributed source", Nuclear Instruments and Methods in Physics Research, 226 (1984) 436-448.

Wielopolski, L., "The Monte Carlo calculation of the average solid subtended by a right circular cylinder from distributed sources", Nuclear Instruments and Methods, 143 (1977) 577-591.

Wielopolski, L., Mitra, S., Doron, O., "Non-carbon based compact shadow shielding for 14 MeV neutrons", J. Rad. Nuc. Chem., In Press, Vol. 281 (2008), 1.

Wielopolski, L., Mitra, S., Hendrey, G., Orion, I., Prior, S., Rogers, H., Runion, B., Torbert, A., "Non-destructive soil carbon analyzer". BNL Report 72200-2004.

Wielopolski, L., Orion, I., Hendrey, G. and Roger, H., “Soil carbon measurements using inelastic neutron scattering”, IEEE Trans.Nucl.Sci., vol. 47, pp. 914-917, June 2000.

Wielopolski, L., Song, Z., Orion, I., Hanson, A.L., Hendry, G., “Basic considerations for Monte Carlo calculations in soil”, App. Rad. Iso., 62 (2005) 97.

www.usgs.gov

Vita

Oded Doron was born at Rotchild (Benai-Zion) Hospital in Haifa, Israel on the 19th day of February in the year 1979 to his loving parents Rachel and Daniel Doron. When Oded was 6 years old, his family immigrated to Houston, Texas where he attended Westbury Senior High School. Oded completed his undergraduate degree at The University of Texas at Austin. He received a B.S.E with a Nuclear and Radiation Engineering Technical Option in May 2002. He continued his study of Nuclear and Radiation Engineering at UT and he received an M.S.E in the Nuclear and Radiation Engineering program under the supervision of Dr. Steven Biegalski. He is currently completing a Ph.D. in the Nuclear and Radiation Engineering program at UT under the supervision of Dr. Steven Biegalski and Dr. Lucian Wielopolski of Brookhaven National Laboratory. Oded has co-authored five journal articles, co-authored a book, and has presented at three conferences.

Permanent address: 7635 Burning Hills Dr.
Houston, Tx. 77071

This dissertation was typed by Oded Doron.